Doctoral dissertation

Bifurcation Analysis of Quasi-Periodic Phenomena in Piecewise-Constant Oscillators

Author
Tri Quoc Truong

March 2018

Nagaoka University of Technology
Department of Integrated Bioscience and Technology

Acknowledgements

This present Ph-D thesis is a collection of studies carried out under the direction and guidance of Associate Professor Tadashi Tsubone of Nagaoka University of Technology during 2015-2017.

I would first like to express the deepest appreciation to my supervisor Associate Professor Tadashi Tsubone for his continuous support and hearty advice throughout this period.

I would like to thank my thesis committee members of Nagaoka University of Technology: Professor Yasuhiro Wada, Professor Masahiro Nakagawa, Professor Masahiro Iwahashi, and Associate Professor Isao Nambu for their insightful comments, and valuable questions.

I would like to thank Dr. Naohiko Inaba of Meiji University for his excellent cooperation, insightful comments, and patiently corrected my writing.

I sincerely thank Professor Tetsuro Endo of Meiji University, Associate Professor Munehisa Sekikawa of Utsunomiya University, and Associate Professor Kuniyasu Shimizu of Chiba Institute of Technology for their helpful advice and suggestions.

I am grateful to Dr. Yoshikazu Yamanaka of Utsunomiya University and my colleagues from Tsubone laboratory at Department of Electrical, Electronics and Information Engineering, Nagaoka University of Technology for friendly helps during the period of this research.

Finally, I would like to express my deep gratitude to my parents, my brother, my wife and my son for their persistent supports and encouragements.

Preface

This study investigates complex quasi-periodic bifurcations such as Arnol'd tongues and Arnol'd resonance webs generated in piecewise-constant oscillators. The piecewise-constant system is referred to as dynamics for which the dynamical equations are represented by one of the simplest nonlinear ordinary differential equations (ODEs) in which the right-hand side of equations is piecewise-constant. By using these simple circuits, we analyze quasi-periodic phenomena with a significantly high resolution.

Nonlinear dynamics represent complex oscillatory behaviors. Nonlinear oscillations include weather occurring on the surface of the earth or information processing conducted in human brains, which can not be explained by linear dynamical systems. Even though these phenomena appear to be statistical at first glance, there exist laws that govern these phenomena.

When we solve nonlinear dynamics, we encounter a bifurcation. The bifurcation is a technical term that refers to a qualitative change of the solution. The solution indicates a scale such as a physical location of the object in mechanical systems and a voltage or a current in electric circuits. We say a bifurcation

occurs when a qualitative change occurs as a parameter crosses a certain threshold value. In this thesis, we investigate bifurcation analysis of quasi-periodic phenomena generated in coupled oscillators. Specifically, we concentrate on the following oscillatory behaviors:

(A) Arnol'd tongues generated in two-coupled oscillators.

(B) Arnol'd resonance webs generated in two-coupled oscillators including a periodic forcing and three-coupled oscillators.

First, we propose an autonomous two-coupled piecewise-constant oscillators (ab. PWCOs) that can generate two-dimensional tori. The governing equation of the coupled oscillators is represented by piecewise-constant dynamics. The advantage of the piecewise-constant system is that the solutions are obtained explicitly and, moreover, the solutions are connected explicitly in each piecewise-constant branch. Using these expressions, we can create a rigorous two-parameter Lyapunov diagram. Our numerical results show that Arnol'd tongues are generated in a wide range of parameter space. Moreover, the analysis of the dynamics arrives at that of a 1-D return map. By using the 1-D return map, we clarify that Arnol'd tongues are surrounded by a non-smooth tangent bifurcation. Several bifurcation boundaries are explicitly derived.

Second, we investigate chaos and quasi-periodic phenomena generated in a non-autonomous two-coupled PWCOs driven by a rectangular periodic forcing. We formulate a numerical procedure for conducting Lyapunov analysis in

PWCOs. In these coupled PWCOs, Arnol'd resonance webs (ab. ARWs) is clearly observed. Chaos occurs around the regions-generating the Chenciner bubbles. Inevitably, we can observe the hysteresis phenomenon, which distorts the Chenciner bubbles in the cases of weak coupling. Furthermore, the generation pattern of two-dimensional tori is clarified by both the numerical experiment and the laboratory measurement.

Third, we present an autonomous three-coupled PWCOs. The Lyapunov exponents are obtained by using a generalized calculation algorithm, which is introduced in previous work. We study on bifurcation structures of ARWs in detail and compare ARWs that is generated in autonomous three-coupled PWCOs and that is generated in non-autonomous two-coupled ones. ARWs and the hysteresis phenomenon are also observed. However, the hysteresis phenomenon does not penetrate the Chenciner bubbles as seen in the non-autonomous system. In order to clarify the mechanism causing the hysteresis phenomenon, a two-coupled delayed logistic map is considered. The hysteresis phenomenon partially occurs as a result of a subcritical Neimark-Sacker bifurcation.

Final, we provide the overall conclusions and discuss some unsolved problems.

Contents

List of Figures

Chapter 1

General Introduction

1.1 Backgrounds

1.1.1 Quasi-periodic phenomena

It has been clarified that nonlinear dynamics represent noteworthy bifurcations. The word "bifurcation" refers to a technical term, which indicates a qualitative change of a solution that occurs when a parameter varies. When a parameter value crosses a certain threshold, called a boundary condition, the number and type of solutions will change. Such a qualitative change is called bifurcation phenomenon.

To explain a typical bifurcation phenomenon, a first order equation of ordinary differential equations (ab. ODEs) is introduced as follows:

$$F(x, \mu) = \dot{x} = \mu + x^2, \tag{1.1}$$

where μ is a parameter, $\mu \in \mathbb{R}$.

- If $\mu < 0$, there exists two equilibrium points, which are solutions in Eq. (1.1).
- If $\mu = 0$, there exists a unique equilibrium point at $x = 0$.

- If $\mu > 0$, there is no equilibrium point.

On the plane $(x, \dot{x})$, the equation shows a parabolic curve. $x_1 = \sqrt{-\mu}$ is an unstable equilibrium point, while $x_2 = -\sqrt{-\mu}$ is a stable equilibrium point, which are shown in Fig. 1.1.1(a). Clearly, at $\mu = 0$, there exists only one equilibrium point owing to collision of two equilibrium points (see Fig. 1.1.1(b)). At this parameter value, the property of the solution is changed. Thus, $\mu = 0$ is called a bifurcation point. Note that for $\mu > 0$, there is no equilibrium point, and the system loses its stability as seen in Fig. 1.1.1(c).

When we solve the bifurcation equations, we obtain bifurcation diagrams, in which we encounter various complex phenomena such as coexistence of periodic oscillations and quasi-periodic oscillations, and chaotic vibration. Chaos is defined as a statistical behavior generated by deterministic systems such as difference equations, ODEs, and partial differential equations. The existence of some kind of periodic oscillations and quasi-periodic oscillations are found in the dynamical systems that have multiple oscillation frequencies. A periodic oscillation is observed if the rotation number that corresponds a ratio between different independent frequencies is rational. By contrast, a quasi-periodic oscillation is observed if the ratio becomes irrational.

Quasi-periodic oscillations are generated in various systems such as biological and engineering systems, and so on [1–6, 12–15]. In the field of electric circuits, to derive the generation conditions of the quasi-periodic oscillations is of great

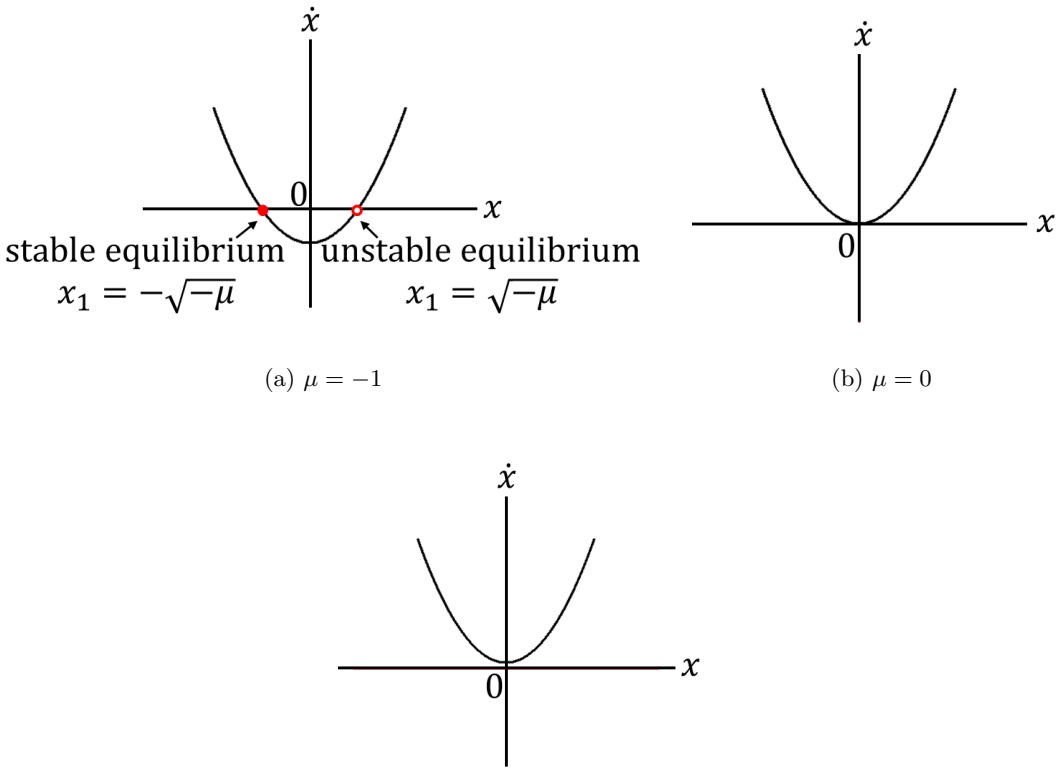

(a) $\mu = -1$

(b) $\mu = 0$

(c) $\mu = 0.2$

Figure 1.1.1 Plane $(x, \dot{x})$ showing bifurcation phenomenon.

importance for applications in designing various practical circuits [7–9]. It is well known that the phase-locking regions that represent periodic oscillations exist in the regions-generating quasi-periodic oscillation are often observed in forced oscillators. The applications of phase-locking have been widely employed, such as phase-locked-loops (ab. PLLs) system that generates an output signal whose phase is synchronized to the received signal in electronic communication systems [6, 13].

1.1.2 Arnol'd Tongues

At an early stage, quasi-periodic oscillations that have two fundamental oscillation frequencies have been investigated. Such quasi-periodic oscillations are called two-dimensional tori, which can occur in two-coupled oscillators or driven self-excited oscillators [16,21,22,24]. It is well-known that infinitely many regions-generating periodic oscillations are in a parameter space, where the ratio between two independent frequencies become a rational number. Such bifurcation structures are universal, which is called Arnol'd tongues. Arnol'd tongues were observed in circadian rhythms, cardiac pacemakers, or radio-controlled clocks, and so on [1, 2].

A typical example of the discrete-time dynamics-generating Arnol'd tongues is sine circle map [2, 6, 11, 12]. A sine circle map is introduced as follows:

$$\theta_{n+1} = \theta_n + \Omega + \frac{K}{2\pi}\sin(2\pi\theta_n) \pmod 1, \tag{1.2}$$

where Ω and K are parameters.

$\Omega = p/q$ is proportional to the ratio of the oscillator frequency and the sine wave frequency. K is the amplitude of the sine wave. Figure 1.1.2 shows a schematic illustration of dynamics on the plane of parameters (Ω, K). In the regions marked by black diagonal lines, $\Omega = p/q$ becomes a rational number, and it shows synchronization regions or Arnol'd tongues. By contrast, the regions marked by white show quasi-periodic oscillations. Moreover, the blue curves show the boundaries between quasi-periodic and periodic oscillations. Noting

that, between two Arnol'd tongues corresponding to p/q and $p^{'}/q^{'}$, there exists another Arnol'd tongue corresponding to $(p+p^{'})/(q+q^{'})$. For example, between $1/3$ and $2/3$, there exists $1/2$, i.e., $1/2 = (1+2)/(3+3)$.

Usually, Arnol'd tongues can be generated through saddle-node bifurcations. Numerical algorithms for solving bifurcation equations of smooth ODEs including saddle-node bifurcation were given by Kawakami [16]. In general, ODEs that includes smooth nonlinear terms must be solved by numerical techniques such as the averaged methods. Inaba et al. applied a shooting algorithm for solving bifurcation equations using an algorithm presented by Kawakami to a piecewise linear dynamics. In this case, the bifurcation equations are represented by a transcendental equation. The transcendental equation includes no approximation. Therefore, the bifurcation equations of piecewise linear ODEs can be solved to any degree of precision by a computer. In Inaba's case, the bifurcation equations were solved with a precision of 10^{-13} [22].

1.1.3 Arnol'd Resonance Web and Chenciner Bubbles

Quasi-periodic oscillations that includes three- or higher frequencies have attracted considerable attention in recent years [28–36, 36–45, 45–61]. Classification of quasi-periodic oscillations is usually performed by Lyapunov analysis. Computational algorithms for deriving the Lyapunov exponents were given by Shimada and Nagashima [63]. In general, n-dimensional autonomous ODEs have n Lyapunov exponents. Let the first, second and n-th Lyapunov expo-

nents be denoted by $\lambda_1, \lambda_2, \cdots, \lambda_n$, respectively ($\lambda_1 \geq \lambda_2 \geq \cdots \geq \lambda_n$).

- An oscillation is said to be periodic if $\lambda_1 < 0$.
- An oscillation is said to be two-dimensinal tori if $\lambda_1 = 0$ and $\lambda_2 < 0$.
- An oscillation is said to be three-dimensinal tori if $\lambda_1 = \lambda_2 = 0$ and $\lambda_3 < 0$.
- An oscillation is said to be n-dimensinal tori if $\lambda_1 = \lambda_2 = \lambda_3 = \cdots = \lambda_{n-1} = 0$ and $\lambda_n < 0$.
- An oscillation is said to be chaotic if $\lambda_1 > 0$.

The studies on Lyapunov analysis have been progressing in discrete-time dynamics [33, 34, 37]. Quasi-periodic bifurcation of three- or higher dimensional tori shows a complex bifurcation structure. In such dynamics, partial entrainment occurs, i.e., two-dimensional tori-entrainment regions exist in a three-dimensional tori-generating region in a parameter space, and they extend in a numerous of directions like a "cobweb". Such web-like bifurcation structures were termed Arnol'd resonance webs (ab. ARWs) by Broer et al. [30]. In addition, periodic generating regions, which emerged at the intersection of different two-dimensional tori-generating regions, are called Chenciner bubbles.

Extensive analysis of quasi-periodic bifurcations generated in discrete-time dynamic has been conducted by Hidaka et al. They investigated a three-coupled delayed logistic map that exhibits an invariant three-dimensional tori [59]. They derived an invariant two-dimensional saddle tori and showed that an invariant

three-dimensional tori occur when the invariant two-dimensional tori attractor and the invariant two-dimensional saddle tori merge and disappear by a saddle-node bifurcation. The results suggest that a qualitative transition from a stable n-dimensional tori to a stable $(n+1)$-dimensional tori is generated by the saddle-node bifurcation of a stable n-dimensional tori and a saddle n-dimensional tori.

Moreover, by the recent rapid increase of computational power, the studies on ARWs in continuous-time dynamics have been done in recent years [35, 39, 53, 60]. Sekikawa et al. proposed a piecewise-linear oscillator that consists of three LC-resonant circuit, and analyze quasi-periodic bifurcations by using a piecewise linear technique [35]. A detailed bifurcation diagram was obtained using explicit solutions of piecewise linear dynamics in a wide range of parameters. Although ARWs was not be observed in their study, their numerical results showed a complex bifurcation structure termed as "two-tori Arnol'd tongues", in which two-dimensional tori generating regions emerge in three-dimensional tori generating regions. In their diagram, two-dimensional tori-generating regions exist in a three-dimensional tori generating region like Arnol'd tongues.

Emelianova et al. analyzed a three-coupled van der Pol oscillator to explain the bifurcation structures outside the "Landa's parallelogram", which a full synchronization regions correspond to the ratio of three independent frequencies is 1:1:1 [38]. ARWs occurs in the parameter space near the parallelogram. The structures of two-dimensional tori generated in the neighborhoods of vertices

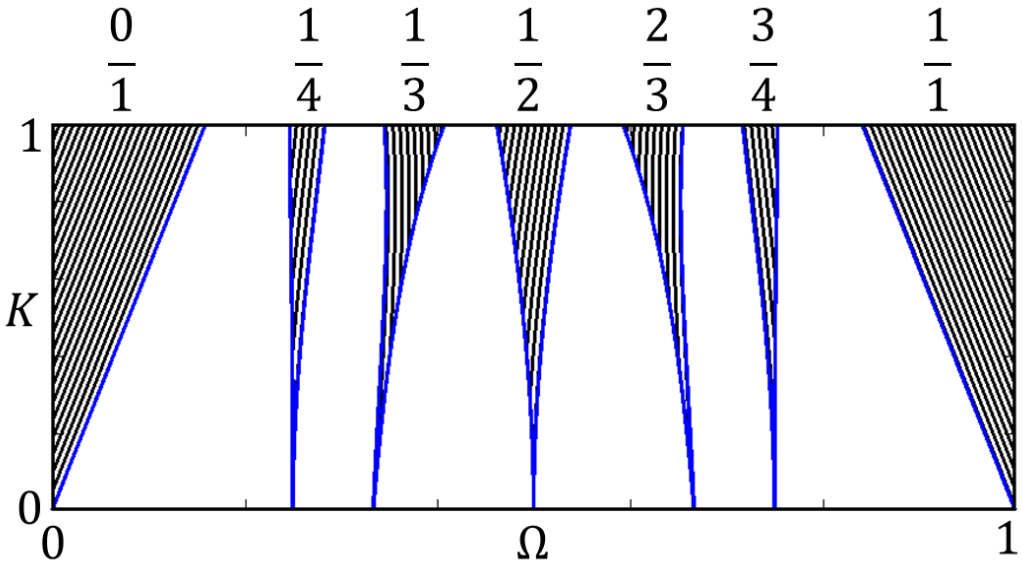

Figure 1.1.2 Arnol'd tongues in the parameter space of a sine circle map.

of this parallelogram are quite complicated. A "fan-shape" structure of two-dimensional tori is discovered in a region generating three-dimensional tori. In particular, the rotation numbers of these two-dimensional tori illustrate many resonance regimes of the different order.

1.1.4 Problems

Quasi-periodic oscillations have attracted a great attention in various types of dynamical systems [16, 21, 22, 24]. In general, we cannot obtain the explicit solution of the governing equation such as ODEs that includes nonlinear terms. From this reason, numerical techniques such as averaged method are used to solve the bifurcation equations. However, bifurcation analysis using numerical techniques contain many problems. Because the convergence-time into a steady

state of quasi-periodic oscillation is intrinsically long, and thereby huge calculation costs are necessary to obtain required accuracy for the analysis. Thus, most of the detailed studies for quasi-periodic phenomena have been targeted toward discrete-time dynamics. Therefore, simpler dynamics are needed to solve the bifurcation analysis in continuous-time dynamics.

Many researchers adopted piecewise-linear dynamics to overcome this difficulty. In piecewise-linear, explicit solutions can be obtained in each piecewise-linear branch. One of the difficulties arises when solving the time when the solution crosses the boundary of piecewise-linear branches. However, the time when the solution strikes the boundaries is generally expressed by an implicit equation. Hence, the implicit equations must be numerically solved. Therefore, not a few numerical calculations are required, and moreover, the application of piecewise-linear techniques to higher dimensional systems appears to be difficult.

In this study, we focus on piecewise-constant oscillators (ab. PWCOs). The governing equations of PWCOs are represented by piecewise-constant dynamics, and the explicit solution can be obtained in piecewise-linear regions without solving any implicit equation. Moreover, the solutions on the boundaries of piecewise-constant branches can be explicitly connected. Usually, the analysis of these oscillators arrives at that of the piecewise-linear return map. Therefore, PWCOs are well suited for theoretical analysis. In addition, PWCOs are quite

simple electric circuit. PWCOs consist of linear capacitors, linear resistors, and voltage controlled current sources (ab. VCCSs). VCCSs can be realized using operational transconductance amplifier. The PWCOs can be easily implemented in the laboratory experiment. In this work, we consider the following oscillatory in these oscillators.

(A) Arnol'd tongues generated in two-coupled oscillators.

Tsubone et al. proposed a simple PWCO driven by a rectangular wave forcing [24]. Tsubone et al. not only succeeded in clarifying the generation mechanism of Arnol'd tongues but also in the rigorous derivation of bifurcation sets of synchronization regions. As far as we know, their work was the first analytical study on the rigorous derivation of Arnol'd tongue boundaries in the continuous-time dynamical system. However, Tsubone's work only considered Arnol'd tongues generated in forced PWCO. In ref. [25], Suzuki et al. introduced PWCOs coupled by signum like element and coupled by hysteresis element. According to their results, the coupled system exhibits both in-phase and anti-phase synchronization phenomenon. However, Arnol'd tongues cannot be observed in these coupled PWCOs.

(B) Arnol'd resonance webs generated in two-coupled oscillators including a periodic forcing and three-coupled oscillators.

In ref [53], Inaba et al. considered a two-coupled PWCOs driven by a rectangular wave forcing to analyze quasi-periodic oscillations. The oscillations gener-

ate three-dimensional tori. Then, using the same computational cost similar to that of discrete-time dynamics, Inaba et al. succeeded in obtaining ARWs with high resolution. However, they use a stroboscopic section as a Poincaré section, it could be difficult to apply this procedure to higher-dimensional PWCOs.

On the other hand, Inaba et al. only considered ARWs generated in the non-autonomous two-coupled PWCOs. It is necessary to discuss ARWs generated in higher-dimensional autonomous systems such as three-coupled PWCOs.

1.2 Outline of the thesis

In this study, we focus on PWCOs, which are considered as simple continuous-time dynamical systems. We propose a calculation algorithm by which we can analyze the quasi-periodic oscillations with a precision similar to that of discrete-time dynamical systems. The thesis is organized as follows:

In Chapter 2, we introduce a preliminary study on PWCOs. We concentrate on the simplest type of PWCOs, which consist of one capacitor and one voltage controlled current sources (ab. VCCSs) with a hysteresis characteristic. The oscillation generates a triangular wave, and it is confirmed numerically and experimentally. We also demonstrate two-coupled fundamental PWCOs, we point out that each PWCO must be connected by capacitors in order for the circuit to become piecewise-constant.

In Chapter 3, we propose an autonomous two-coupled PWCOs that can generate two-dimensional tori. The governing equation of the coupled oscillators

is represented by piecewise-constant dynamics. The advantage of the piecewise-constant system is that the solutions are obtained explicitly and, moreover, the solutions are connected explicitly in each piecewise-constant branch. Using these expressions, we can create a rigorous two-parameter Lyapunov diagram. Our numerical results showed that Arnol'd tongues are generated in a wide range of parameter space. Moreover, the analysis of the dynamics arrives at that of a 1-D return map. By analyzing this 1-D return map, we clarified that Arnol'd tongues are surrounded by a non-smooth tangent bifurcation. Several bifurcation boundaries were explicitly derived.

In Chapter 4, we investigate chaos and quasi-periodic oscillations generated in a non-autonomous two-coupled PWCOs. We formulated the numerical procedure for conducting the Lyapunov analysis in PWCOs. This procedure is applicable in both autonomous and non-autonomous PWCOs driven by a rectangular wave forcing. The extremely simple procedure will contribute to the study on bifurcation analysis of the family of PWCOs. Two-parameter Lyapunov diagrams were obtained, which show the complex bifurcation structures. According to the numerical results, chaos occurred around the regions-generating the Chenciner bubbles. Inevitably, we observed the hysteresis phenomenon, which distorts the Chenciner bubbles in the cases of weak coupling. Furthermore, the generation pattern of two-dimensional tori was demonstrated numerically and experimentally.

In Chapter 5, we present an autonomous three-coupled PWCOs. Two-parameter Lyapunov diagrams were derived with high resolutions using these oscillators. According to the numeric, the hysteresis phenomenon was observed. It did not distort the Chenciner bubbles as observed in two-coupled PWCOs driven by a rectangular wave forcing. To clarify this phenomenon, a two-coupled delayed logistic map was investigated. Based on Lyapunov analysis using these dynamics, it was suggested that the hysteresis might occur owing to a subcritical Neimark-Sacker bifurcation.

Finally, in Chapter 6, we provide the overall conclusions and discuss some unsolved problems.

Chapter 2

Fundamental of Piecewise-Constant Oscillator

2.1 Introduction

Analysis of chaos and related bifurcation phenomena in nonlinear continuous-time dynamical systems have attracted intensive research interest in the last five decades [16–20]. One of the main problems in this field is demonstrating chaotic behavior in rigorous sense. Many researchers have attempted to solve this problem by adopting simpler dynamics. Some researchers adopted piecewise-linear dynamics to overcome this difficulty [17, 19]. In piecewise-linear, explicit solutions can be obtained in each piecewise-linear branch. However, it is not easy to prove the generation of chaotic behaviors in a rigorous sense. One of the difficulties is that it is necessary to solve the time when the solution crosses the boundary of piecewise-linear branch. However, the time when the solution strikes the boundaries is generally expressed by an implicit equation. Hence, the implicit equations must be numerically solved.

To solve these problems, Tsubone et al. proposed more simplified electrical circuit called a piecewise-constant oscillator (ab. PWCO) [23]. PWCOs consist of linear capacitors, linear resistors and voltage controlled current sources (ab. VCCSs). There are two kinds of VCCSs: VCCS with hysteresis characteristic and VCCS with signum characteristic. VCCSs can be realized using operational transconductance amplifier (ab. OTA). The piecewise-constant oscillators can be easily implemented in the laboratory experiment.

The PWCOs are quite simple. However, they generate various complex bifurcations [23–25, 27]. The state equations are represented by piecewise-constant equations, and thus, rigorous analysis can become possible using these oscillators. Moreover, the analysis of PWCOs arrives at those of the piecewise-linear return maps. By using these return maps, complex bifurcation phenomena can be clarified completely.

This chapter introduces a fundamental circuit of PWCO, which consists of a capacitor and a VCCS with a hysteresis characteristic. This oscillator is considered to be the simplest example of PWCOs. The oscillations generates a triangular wave, which is confirmed both numerically and experimentally. By demonstrating two-coupled fundamental PWCOs, we point out that each PWCO must be connected by capacitors in order for the circuit to become piecewise-constant.

2.2 Circuit model

Figure 2.2.1(a) shows a circuit diagram of the simplest PWCO. The voltage that acrosses the capacitor C is v. The VCCS with a hysteresis characteristic $H(v)$ is shown in Fig. 2.2.1(b). When $H(v) = I_h$, v is increasing. v increases to V_{th}, $H(v)$ switches from I_h to $-I_h$. Then v is decreasing. When v decreases to $-V_{th}$, $H(v)$ switches from $-I_h$ to I_h. The circuit dynamic is represented by

$$C\frac{\mathrm{d}v}{\mathrm{d}t} = H(v). \tag{2.1}$$

Noting that, $C\dfrac{\mathrm{d}v}{\mathrm{d}t}$ depends on two values of $H(v)$: I_h or $-I_h$. Hence, this oscillator is called a piecewise-constant system. By using the following dimensionless variables and parameters,

$$\begin{aligned} v = V_{th}x,\ t = \frac{CV_{th}}{I_h}\tau, \\ h(x)I_h = H(V_{th}x). \end{aligned} \tag{2.2}$$

the circuit dynamic is described by

$$\dot{x} = h(x) \quad \left(\cdot = \frac{\mathrm{d}}{\mathrm{d}\tau}\right), \tag{2.3}$$

where $h(x)$ is a normalized hysteresis characteristic as shown in Fig. 2.2.2. When x on the upper branch, x increases proportionally to time. h switches from 1 to -1 if x reaches to the threshold $x = 1$, and x jumps to the lower branch. Then x decreases proportionally to time. h switches from -1 to 1 if x reaches to the threshold $x = -1$. The system repeats again this behavior. Here, we focus on the case $-1 \leq x \leq 1$. Therefore, the circuit generates a triangular

wave as shown in Fig. 2.2.3(a). The time-series waveform is also confirmed in laboratory measurement in Fig. 2.2.3(b).

An implementation circuit for Fig. 2.2.1(a) is shown in Fig. 2.2.4(a). Hysteresis characteristic can be realized by using two VCCSs, which can be realized by OTAs. The $v - i$ characteristic of an OTA is shown in Fig. 2.2.4(b). The amplitude of the saturation output current is controlled via the amplifier bias current I_{ABC}. The transconductance g_m in the linear region can be assumed to be sufficiently large. The output current of OTA is expressed as follows.

$$i = I_h \cdot \mathrm{sgn}(V_{th} - v), \tag{2.4}$$

where I_h is the amplitude of the saturation output current ($I_h > 0$).

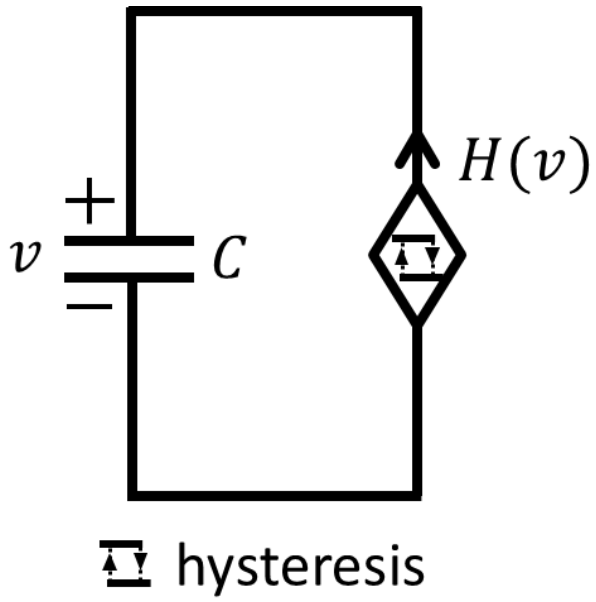

(a) Circuit model

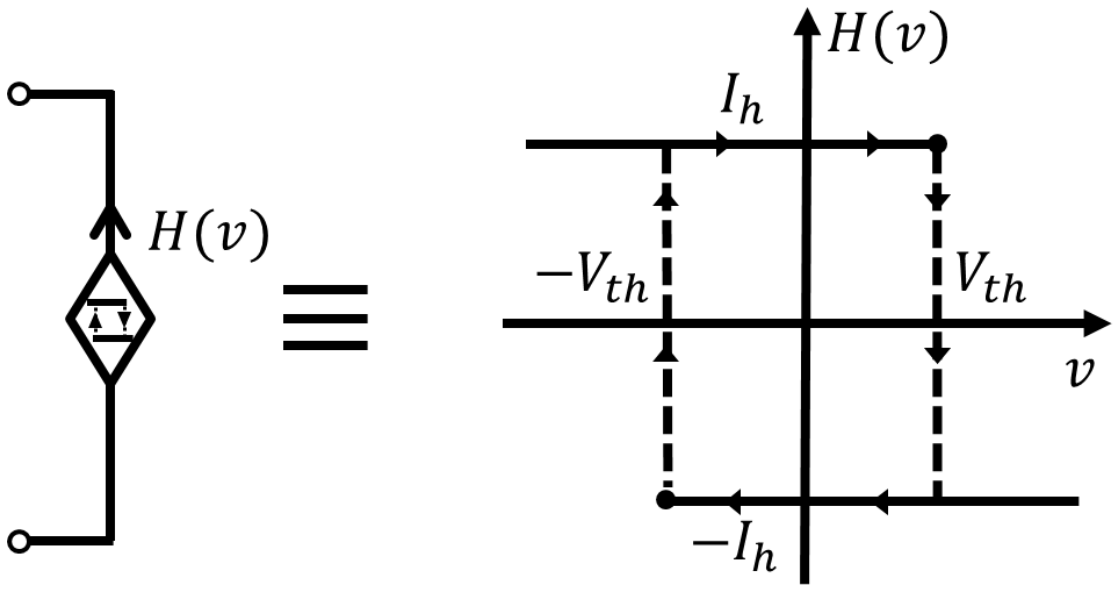

(b) Voltage controlled current source with hysteresis characteristic.

Figure 2.2.1 Fundamental of piecewise-constant oscillator.

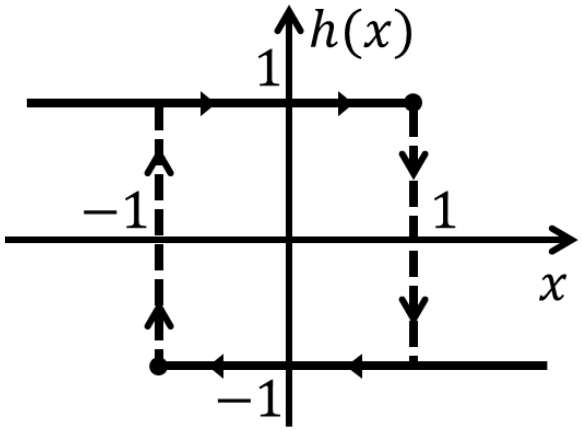

Figure 2.2.2 Normalized hysteresis element.

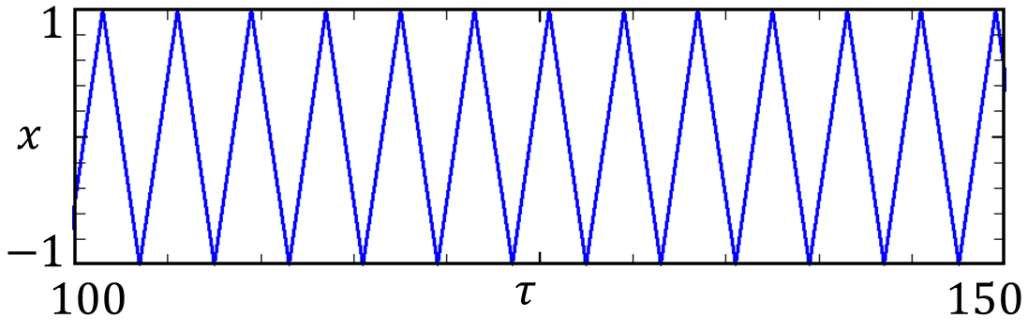

(a) Numerical experiment.

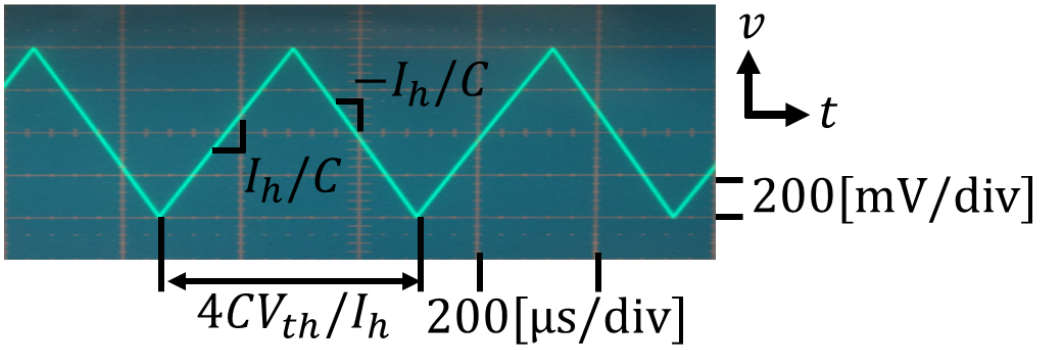

(b) Laboratory measurement.

Figure 2.2.3 Time-series waveform.

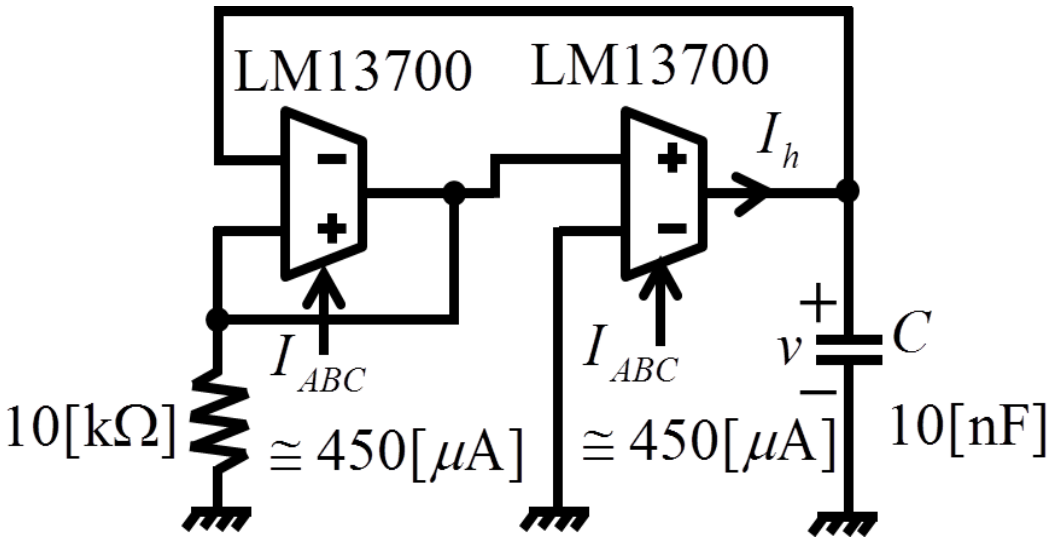

(a) Circuit implementation using OTAs.

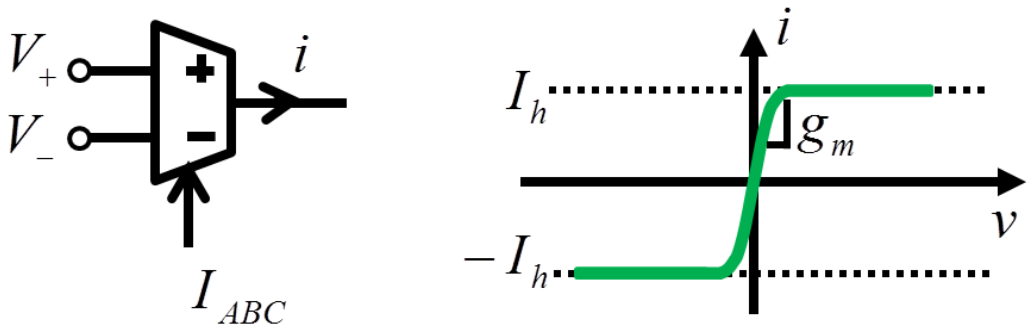

(b) Characteristic of OTA.

Figure 2.2.4 Circuit implementation.

2.3 Two-coupled circuit of piecewise-constant oscillators

Our study concentrates on bifurcation analysis of higher-dimensional circuits. In this section, we consider two-coupled PWCOs. The circuit coupled by a resistor and a capacitor is shown in Fig. 2.3.1(a) and Fig. 2.3.1(b), respectively. The circuit dynamics in Fig. 2.3.1(a) is described by following equations.

$$\begin{aligned} C_1 \frac{\mathrm{d}v_1}{\mathrm{d}t} &= (v_2 - v_1)/R + I_1, \\ C_2 \frac{\mathrm{d}v_2}{\mathrm{d}t} &= (v_1 - v_2)/R + I_2, \end{aligned} \tag{2.5}$$

where I_1, I_2 are VCCSs, such as hysteresis or signum-like characteristic.
The dynamical oscillator represents a two-dimensional circuit. Noting that the right-hand side of Eq. 2.5 depends on v_1 and v_2, and this equation is not piecewise-constant.

By contrast, the circuit dynamics in Fig. 2.3.1(b) is expressed by

$$\begin{aligned} \frac{C_1C_2 + C_1C_3 + C_2C_3}{C_3} \frac{\mathrm{d}v_1}{\mathrm{d}t} &= \frac{C_2 + C_3}{C_3} I_1 + I_2, \\ \frac{C_1C_2 + C_1C_3 + C_2C_3}{C_3} \frac{\mathrm{d}v_2}{\mathrm{d}t} &= \frac{C_1 + C_3}{C_3} I_2 + I_1. \end{aligned} \tag{2.6}$$

Since the circuit has a loop including C_3 that consists of capacitors only, the dimension is the same as that of the circuit dynamics connected by a resistor. Noting that the state equation is piecewise-constant equation. Therefore, the fundamental PWCOs coupled by capacitors are well suited for theoretical analysis.

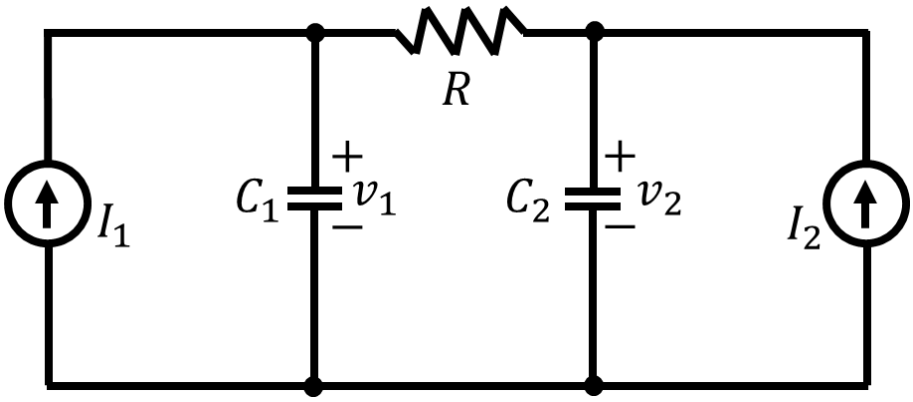

(a) Two-coupled circuit connected by a resistor.

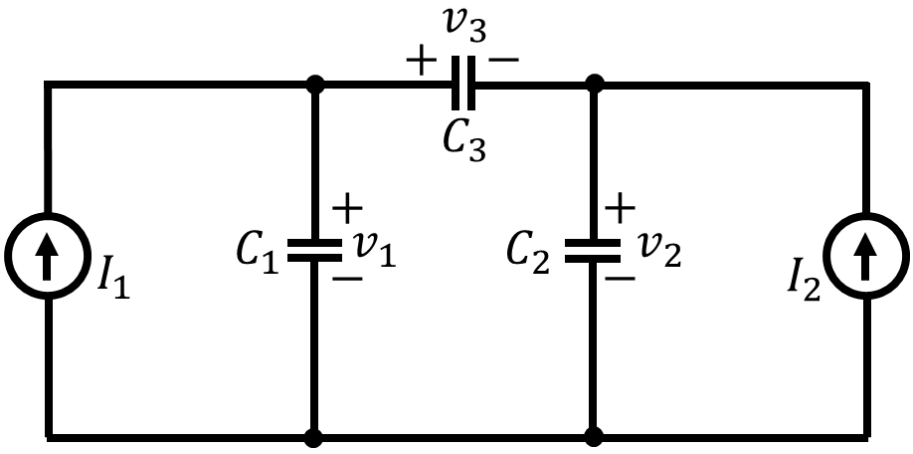

(b) Two-coupled circuit of piecewise-constant oscillator.

Figure 2.3.1 Two-coupled circuits.

2.4 Conclusions

We introduced a fundamental concept of PWCO, which is considered to be the simplest PWCO. The oscillation generates a triangular wave, which is confirmed both numerically and experimentally. By demonstrating two-coupled systems of the fundamental PWCO, we point out that the PWCOs must be coupled by capacitors. In the following chapter, we discuss complex bifurcations generated in these simple circuits in detail.

Chapter 3

Arnol'd Tongues Generated in Two-coupled Piecewise-Constant Oscillators

3.1 Introduction

In nonlinear electric circuits that have two fundamental oscillation frequencies, quasi-periodic oscillations can emerge, which are called two-dimensional tori. Quasi-periodic oscillation represents a non-periodic motion, where the rotation number that corresponds a ratio between two independent frequencies is irrational. In two-dimensional tori-generating systems represented by coupled oscillators or forced oscillators, we can observe infinitely many regions generating periodic oscillations, where two independent frequencies become rational, in parameter space. Such bifurcation structures are well-known as Arnol'd tongues [16, 21, 22, 24].

Arnol'd tongues were observed in circadian rhythms, cardiac pacemakers, or radio-controlled clocks, and so on [1, 2]. Applications of Arnol'd tongues have

been proposed and analyzed such as phase locked loops (ab. PLLs) control system that generates an output signal whose phase is synchronized to the received signal in electronic communication systems [6, 13].

Arnol'd tongues have been studied in various types of dynamical systems in recent years [16, 21, 22, 24]. Kawakami et al. proposed the computational algorithms for obtaining bifurcation sets for forced oscillators including smooth nonlinear terms that are expressed as a nonautonomous smooth ordinary differential equations (ODEs) [16]. Usually, ODEs that includes smooth nonlinear terms must be solved by numerical techniques such as the Euler and Runge-Kutta methods. Hence, the numerical errors are inevitable.

Inaba et al. applied the shooting algorithm proposed by Kawakami to a piecewise linear forced oscillators [21, 22]. In piecewise-linear oscillators, upon obtaining an explicit solution in each piecewise-linear branch, we can calculate the bifurcation sets precisely. To discuss the piecewise-linear equation, it is necessary to solve the boundary condition, i.e., we must solve the time when the solution crosses the boundary of the piecewise-linear branches. However, the boundary condition is generally represented by implicit equations. Hence, the numerical errors cannot be avoided and to discuss the dynamics of higher dimensional dynamics becomes difficult.

To overcome these problems, Tsubone et al. proposed the piecewise-constant oscillator (ab. PWCO) [23]. The governing equation of PWCO is represented

by piecewise-constant equation, and the explicit solution can be obtained in piecewise-linear regions without solving any implicit function. Moreover, the solutions on the boundaries of piecewise-constant branches can be explicitly connected. The analysis of these oscillators arrives at that of the piecewise-linear return map. Therefore, PWCO is well suited for theoretical analysis. In order to analyze Arnol'd tongues, Tsubone et al. proposed a simple PWCO driven by a rectangular wave forcing [24]. Tsubone not only succeed in clarifying the generation mechanism of Arnol'd tongues but also in the explicit derivation of bifurcation sets of synchronization regions. As far as we know, their work was the first analytical study on the explicit derivation of Arnol'd tongue boundaries in the continuous-time dynamical system. However, Tsubone's work only considered Arnol'd tongues generated in forced PWCO. In ref. [25], Suzuki et al. introduced PWCOs coupled by signum like element and coupled by hysteresis element. According to their results, the coupled system exhibits both in-phase and anti-phase synchronization phenomenon. However, Arnol'd tongues cannot be observed in these coupled PWCOs.

This chapter proposes an autonomous two-coupled PWCOs. Because the right-hand side of the state equations take only constant values, the system dynamics can be rigorously analyzed. The Lyapunov analysis is conducted using a calculation algorithm for the rigorous solutions in autonomous PWCOs. Our numerical results show that Arnol'd tongues are observed in a wide range of

the parameter space. Moreover, the system dynamics is reduced to that of a 1-dimensional (ab. 1-D) return map. By using the 1-D return map, we clarify that Arnol'd tongues are surrounded by non-smooth tangent bifurcations. Several bifurcation boundaries are explicitly derived.

3.2 Two-coupled Piecewise-Constant Oscillators

Figure 3.2.1 shows an autonomous two-coupled circuit, which consists of two PWCOs as introduced in Chapter 2. Each oscillator is connected by a capacitor. The voltage across three capacitors, which are denoted by C_1, C_2, and C_3, are v_1, v_2, and v_3, respectively. $H_1(v_1)$ and $H_2(v_2)$ are the two hysteresis elements with their characteristics are explained in a similar manner as Fig. 2.2.1(b). The governing equation of two-coupled autonomous circuits is represented as the following equations from Kirchhoff's law:

$$\begin{aligned} \frac{C_1C_2+C_1C_3+C_2C_3}{C_3}\frac{\mathrm{d}v_1}{\mathrm{dt}} &= \frac{C_2+C_3}{C_3}H_1(v_1)+H_2(v_2), \\ \frac{C_1C_2+C_1C_3+C_2C_3}{C_3}\frac{\mathrm{d}v_2}{\mathrm{dt}} &= \frac{C_1+C_3}{C_3}H_2(v_2)+H_1(v_1). \end{aligned} \tag{3.1}$$

Via rescaling,

$$\begin{aligned} v_1 = V_{th1}x,\ v_2 = V_{th2}y,\ t=\gamma\tau, \\ h_1(x)I_{h1} = H_1(V_{th1}x),\ h_2(y)I_{h2} = H_2(V_{th2}y), \\ \gamma = \frac{V_{th1}(C_1C_2+C_1C_3+C_2C_3)}{I_{h1}C_3}, \\ \frac{I_{h2}}{I_{h1}} = D_1,\ \frac{V_{th1}}{V_{th2}} = D_2,\ \frac{C_2+C_3}{C_3} = D_3,\ \frac{C_1+C_3}{C_3} = D_4, \end{aligned} \tag{3.2}$$

the circuit dynamics is written by

$$\begin{aligned} \dot{x} &= D_3 h_1(x) + D_1 h_2(y), \\ \dot{y} &= D_2 h_1(x) + D_1 D_2 D_4 h_2(y) \quad \left(\cdot = \frac{\mathrm{d}}{\mathrm{d}\tau} \right), \end{aligned} \tag{3.3}$$

where $h_1(x)$, $h_2(y)$ are normalized hysteresis loops, which are denoted in Fig. 2.2.2. The circuit dynamics contain four parameters: D_1, D_2, D_3 and D_4.

To facilitate the analysis of this system, we decrease the number of parameters by defining new state variables and parameters as follows.

$$\begin{aligned} X = \frac{x}{D_2}, Y = \frac{y}{D_2}, \\ \gamma_1 = \frac{D_3}{D_2},\ \gamma_2 = \frac{D_1}{D_2},\ \beta = D_1 D_4. \end{aligned} \tag{3.4}$$

$H_1(v_1)$ and $H_2(v_2)$ are restructured as shown in Fig. 3.2.2(a) and Fig. 3.2.2(b), respectively. The two hysteresis elements function as follows. $H_1(v_1)$ switches from I_{h1} to $-I_{h1}$ if v reaches $\dfrac{V_{th1}^2}{V_{th2}}$ and switches from $-I_{h1}$ to I_{h1} if v reaches $-\dfrac{V_{th1}^2}{V_{th2}}$. $H_2(v_2)$ switches from I_{h2} to $-I_{h2}$ if v reaches V_{th1} and switches from $-I_{h2}$ to I_{h2} if v reaches $-V_{th1}$.

The circuit dynamics can be rewritten by

$$\begin{aligned} \dot{X} &= \gamma_1 h_1(X) + \gamma_2 h_2(Y), \\ \dot{Y} &= h_1(X) + \beta h_2(Y). \end{aligned} \tag{3.5}$$

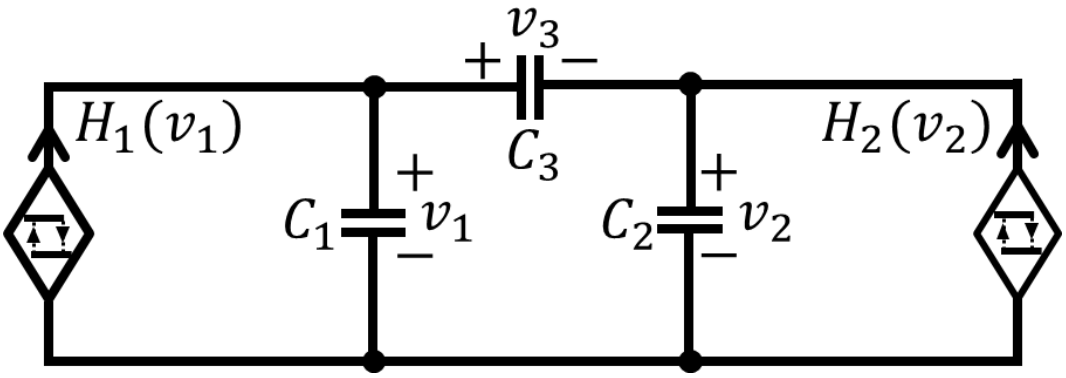

Figure 3.2.1 Circuit model of a two-coupled PWCOs.

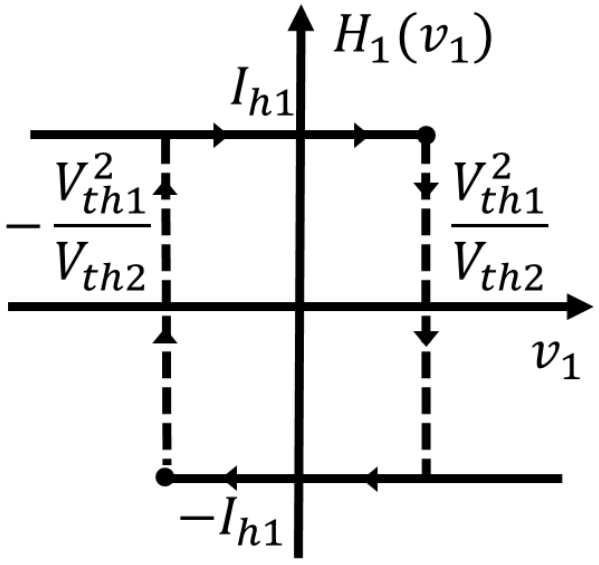

(a) $H_1(v_1)$.

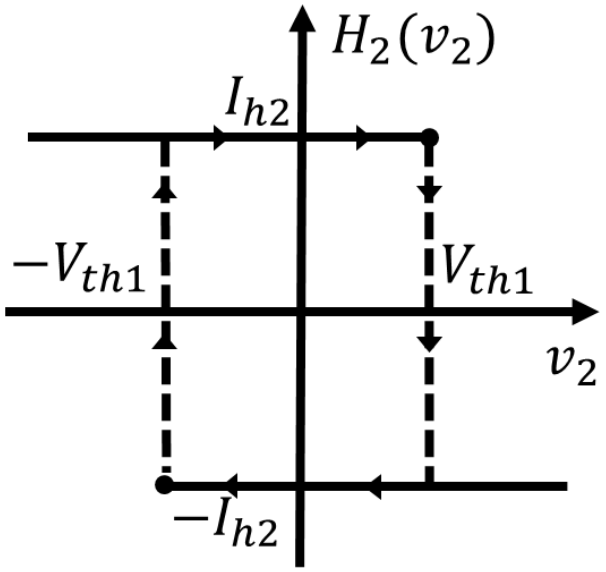

(b) $H_2(v_2)$.

Figure 3.2.2 $v - i$ characteristics of the hysteresis element.

3.3 Oscillation behaviors

In order to explain the behaviors of the circuit dynamics, we rewrite Eq. 3.5 as follows:

$$\begin{aligned} \dot{x} &= k_{xi} = \gamma_1 h_1(x) + \gamma_2 h_2(y), \\ \dot{y} &= k_{yi} = h_1(x) + \beta h_2(y). \end{aligned} \tag{3.6}$$

Noting this state variables x and y in Eq. 3.6 is different from state variables in Eq. 3.3. Since $h_1(x)$ or $h_2(y)$ takes two values: -1 and 1, $\boldsymbol{k}(i) = (k_{xi}, k_{yi})^\top$ takes constant values. The notation $^\top$ represents the transpose of the vector. Using these notations, the circuit dynamics are expressed as follows:

$$\dot{\boldsymbol{x}} = \boldsymbol{k}(i) \in D(i), \quad i \in \{0, 1, 2, 3\}, \tag{3.7}$$

where $\boldsymbol{x} = (x, y)^\top$ and i is an index for indicating the region $D(i)$. $\boldsymbol{k}(i)$ and region $D(i)$ are summarized in Table 3.1. For example, in the case of $i = 0$, since $h_1(x) = 1$ and $h_2(y) = 1$, $\boldsymbol{k}(0) = (k_{x0}, k_{y0})^\top = (\gamma_1 + \gamma_2, 1 + \beta)^\top$.

Figure 3.3.1 introduces the circuit behavior on phase space with horizontal axis x and vertical axis y. The trajectory leaving $\boldsymbol{x}_0 = (x_0, y_0)^\top$, which is marked by red point on the boundary $x = -1$ of region $D(0)$, will reach the boundary $y = 1$. Since the state variable y reaches the threshold $y = 1$, $h_2(y)$ switches from 1 to -1. The trajectory transitions from region $D(0)$ containing $\boldsymbol{k}(0) = (\gamma_1 + \gamma_2, 1 + \beta)^\top$ to region $D(1)$ containing $\boldsymbol{k}(1) = (\gamma_1 - \gamma_2, 1 - \beta)^\top$. In such a case, x increases and y decreases. Thus, the trajectory reaches the boundary $x = 1$. At this time, $h_1(x)$ switches from 1 to -1. The trajectory

transitions from region $D(1)$ containing $\boldsymbol{k}(1) = (\gamma_1 - \gamma_2, 1 - \beta)^\top$ to region $D(3)$ containing $\boldsymbol{k}(3) = (-\gamma_1 - \gamma_2, -1 - \beta)^\top$. Similarly, the trajectory will reach the boundary $y = -1$ of region $D(2)$ and $x = -1$ of region $D(0)$, respectively. The trajectory will be repeated again these behaviors.

Table 3.1 Values of $\boldsymbol{k}(i)$

i	$\boldsymbol{k}(i) = (k_{xi}, k_{yi})^\top$	Regions $D(i)$
0	$(\gamma_1 + \gamma_2, 1 + \beta)^\top$	$\{(x, y, h_1(x), h_2(y)) \mid -1 \le x, y \le 1, h_1(x) = 1, h_2(y) = 1\}$
1	$(\gamma_1 - \gamma_2, 1 - \beta)^\top$	$\{(x, y, h_1(x), h_2(y)) \mid -1 \le x, y \le 1, h_1(x) = 1, h_2(y) = -1\}$
2	$(-\gamma_1 + \gamma_2, -1 + \beta)^\top$	$\{(x, y, h_1(x), h_2(y)) \mid -1 \le x, y \le 1, h_1(x) = -1, h_2(y) = 1\}$
3	$(-\gamma_1 - \gamma_2, -1 - \beta)^\top$	$\{(x, y, h_1(x), h_2(y)) \mid -1 \le x, y \le 1, h_1(x) = -1, h_2(y) = -1\}$

Next, by changing γ_1 and β, we introduce some patterns of trajectory from Fig. 3.3.2 to Fig. 3.3.5. When $\tau = 0$, we set initial values at $x_0 = -0.5$, $y_0 = 0.9, h_1(x) = 1, h_1(y) = 1$. We draw the trajectory from $\tau = 200$ to $\tau = 205$. Our numerical results show that $\tau = 200$ is enough as a transient. In these simulation results, Fig. (a) shows attractor; Fig. (b), (c) shows time waveforms of the state variables x and y, respectively. We fix the parameter values $\gamma_1 = 2.5$, $\gamma_2 = 2.0$ in Fig. 3.3.2–3.3.4. The trajectory shows various periodic oscillation at $\beta = 2.5$, $\beta = 6, 5$ and $\beta = 12.0$ as shown in Fig. 3.3.2, Fig. 3.3.3 and 3.3.4, respectively. By contrast, a quasi-periodic oscillation is observed at $\gamma_1 = 2.5$, $\gamma_2 = 0.7$, and $\beta = 2.9$ as shown in Fig. 3.3.5.

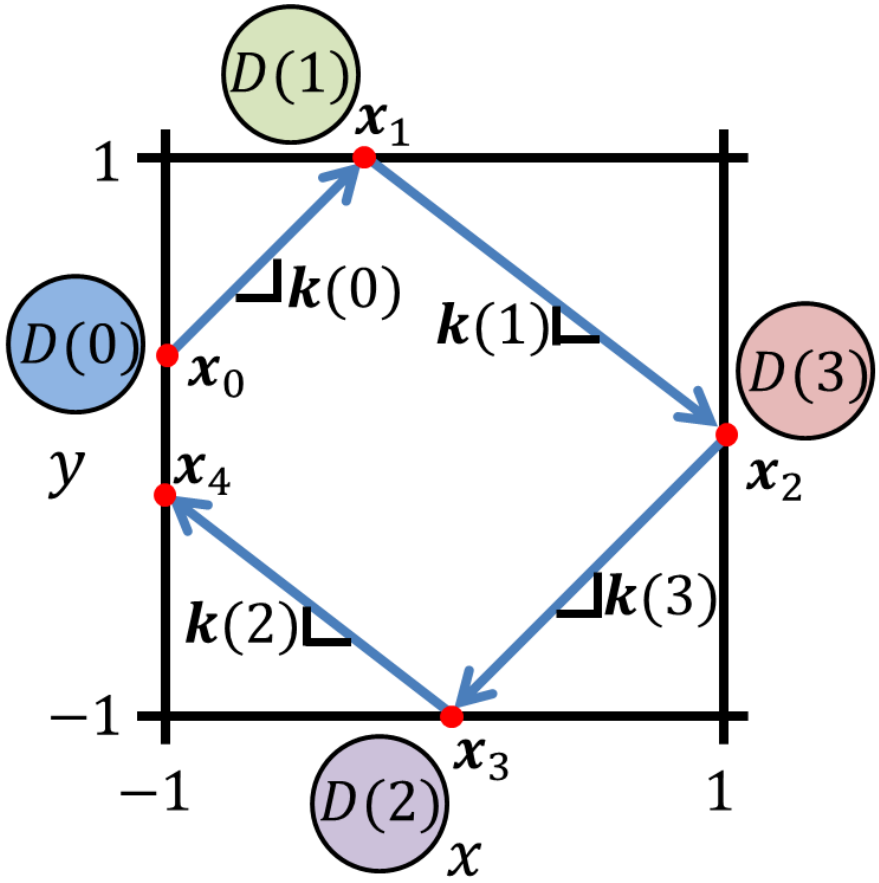

Figure 3.3.1 Example of oscillation behaviors.

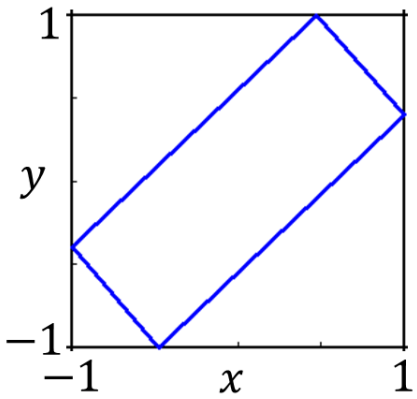

(a)

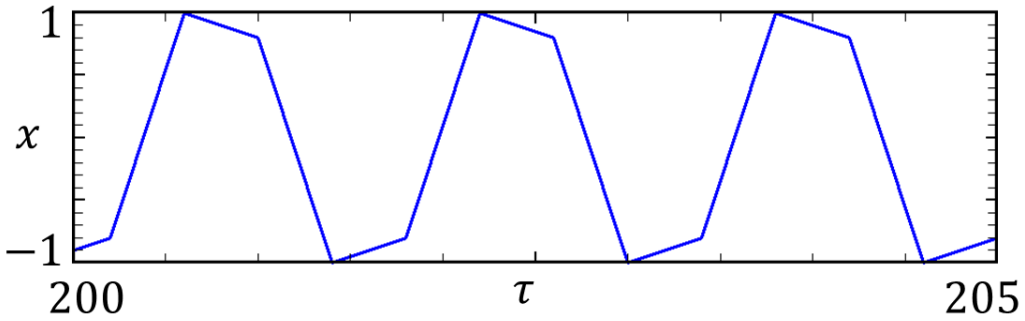

(b)

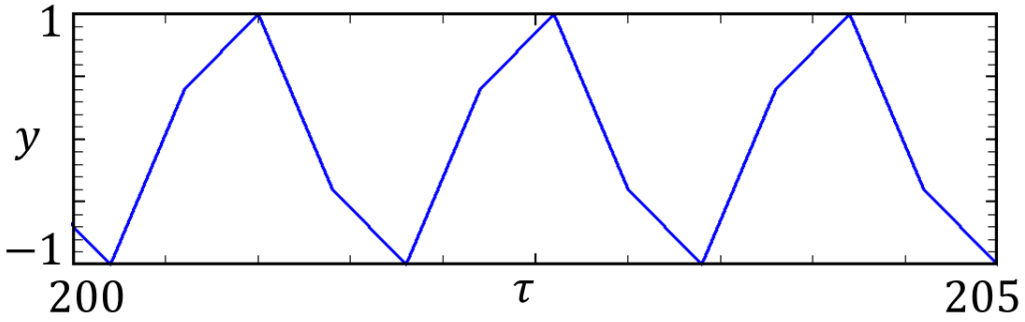

(c)

Figure 3.3.2 Periodic oscillation obtained at $\beta = 2.5, \gamma_1 = 2.5, \gamma_2 = 1.2$.

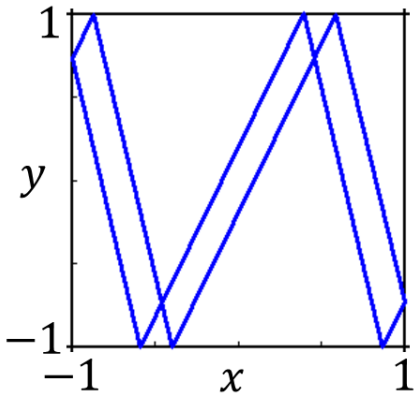

(a)

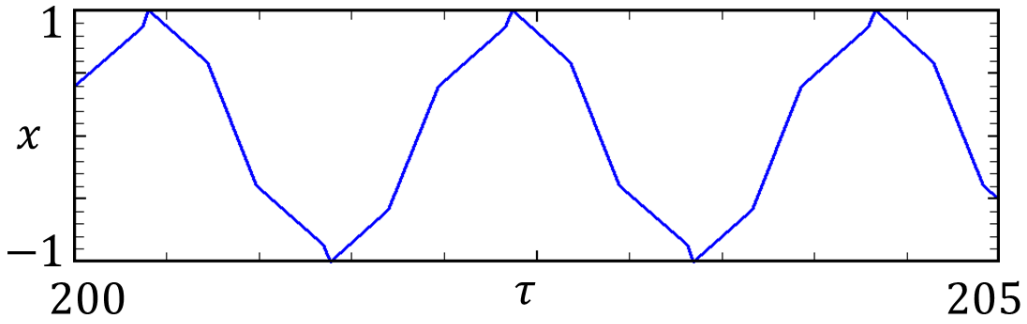

(b)

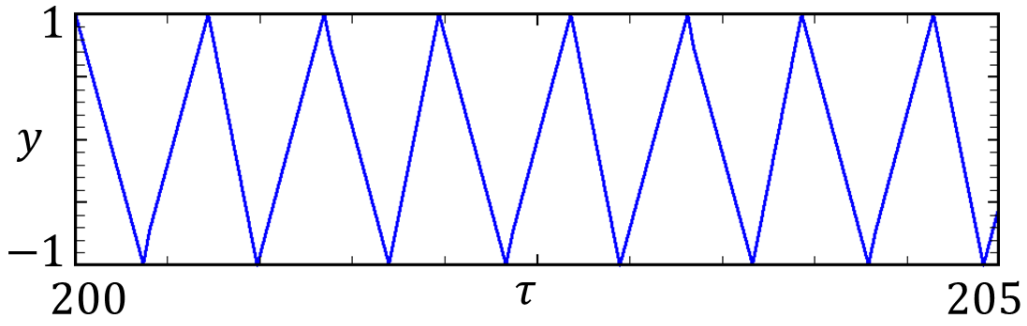

(c)

Figure 3.3.3 Periodic oscillation obtained at $\beta = 6.5, \gamma_1 = 2.5, \gamma_2 = 1.2$.

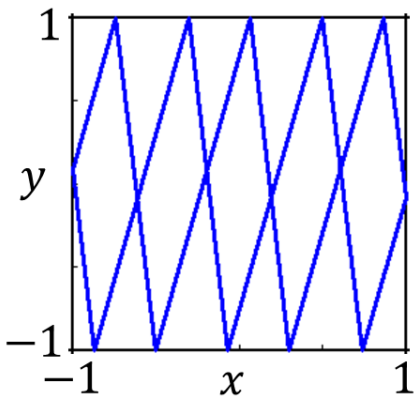

(a)

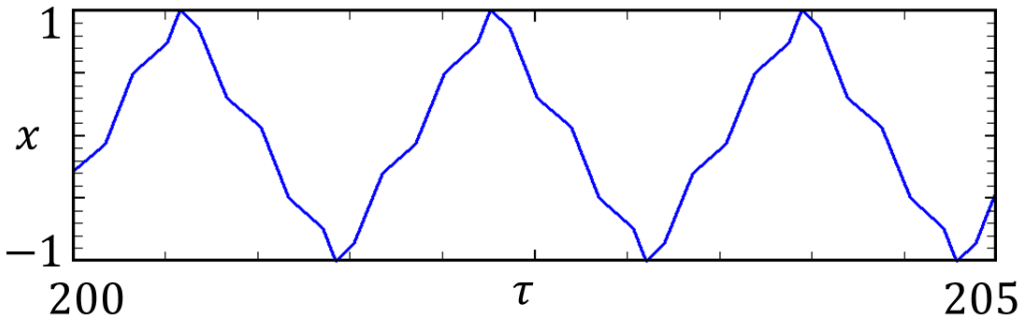

(b)

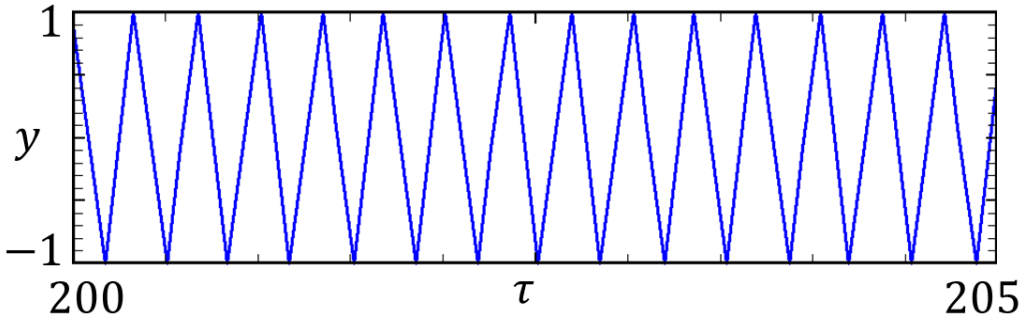

(c)

Figure 3.3.4 Periodic oscillation obtained at $\beta = 12.0, \gamma_1 = 2.5$, $\gamma_2 = 1.2$.

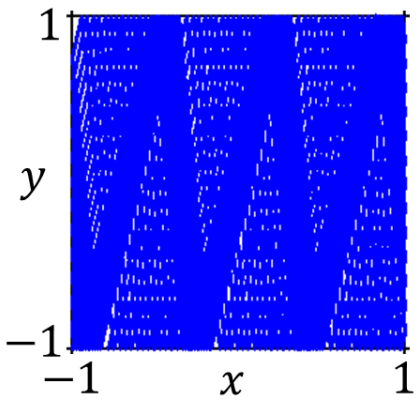

(a)

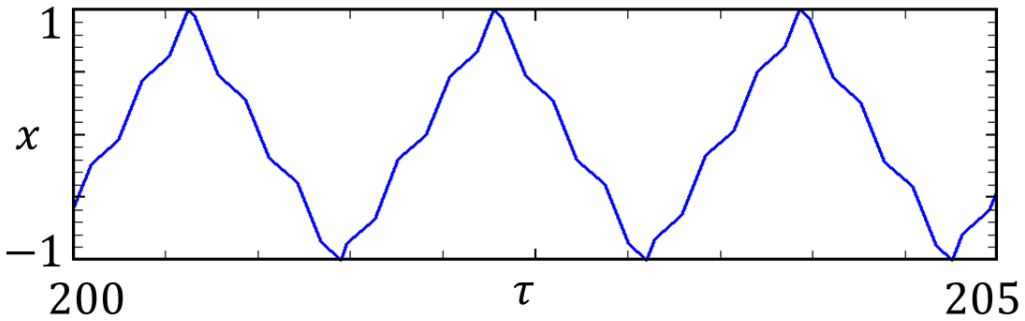

(b)

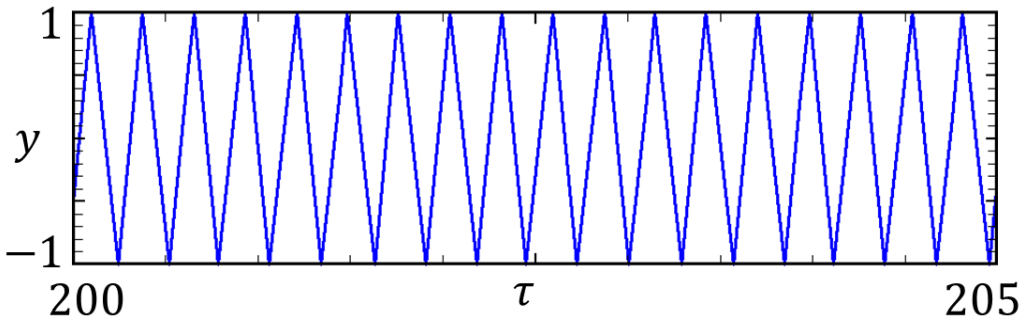

(c)

Figure 3.3.5 Quasi-periodic oscillation obtained at $\beta = 14.5, \gamma_1 = 2.5, \gamma_2 = 1.2$.

3.4 Calculation algorithm for the derivation of rigorous solutions

In this section, we introduce a calculation algorithm for deriving of the explicit solutions in the autonomous two-coupled PWCOs, which was reported in Ref. [25]. The calculation of the trajectories can be accomplished by the following 4 steps.

STEP 1

We provide the initial values $\big(x_0, y_0, h_1(x_0), h_2(y_0)\big)$ and obtain the region containing the initial values by referring to Table 3.1.

STEP 2

We calculate the time τ when the trajectory leaving $\boldsymbol{x}_0 = (x_0, y_0)^\top$ reaches $\boldsymbol{x}_1 = (x_1, y_1)^\top$ on the boundary, i.e., either one of $x = 1$, $x = -1$, $y = 1$ or $y = -1$. The state $\boldsymbol{x}_1$ is calculated by

$$\boldsymbol{x}_1 = \boldsymbol{x}_0 + \boldsymbol{k}(i) \cdot \tau, \tag{3.8}$$

where $\boldsymbol{k}(i)$ is obtained from Table 3.1. By introducing a normal vector $\boldsymbol{n}^\top$ for the boundary, the boundary condition is expressed as

$$\boldsymbol{n}^\top \cdot \boldsymbol{x}_1 = P, \tag{3.9}$$

where P is a constant value; $\boldsymbol{n}^\top$ and P are listed in Table 3.2. For example, if the trajectory arrives at $y = 1$ containing the normal vector $\boldsymbol{n}^\top = (0\ 1)$ at $\boldsymbol{x}_1 = (x_1, y_1)^\top = (x_1, 1)^\top$, the scalar P is $P = 1$.

Substituting Eq. 3.8 into Eq. 3.9 yields

$$\tau = \frac{P - \boldsymbol{n}^\top \cdot \boldsymbol{x}_0}{\boldsymbol{n}^\top \cdot \boldsymbol{k}(i)}. \tag{3.10}$$

For example, we calculate the time when the trajectory leaving $\boldsymbol{x}_0$ on the boundary $x = -1$ corresponding region $D(0)$ hits the boundary $y = 1$ or $x = 1$ corresponding region $D(1)$ or $D(2)$, respectively.

If the trajectory reaches $y = 1$, the time τ_0 is explicitly expressed as

$$\tau_0 = \frac{P - \boldsymbol{n}^\top \cdot \boldsymbol{x}_0}{\boldsymbol{n}^\top \cdot \boldsymbol{k}(0)}, \tag{3.11}$$

where $\boldsymbol{n}^\top = (0\ 1)$, $P = 1$, and $\boldsymbol{k}(0) = (\gamma_1 + \gamma_2, 1 + \beta)^\top$.

If the trajectory reaches $x = 1$, the time τ_1 is explicitly expressed as

$$\tau_1 = \frac{P - \boldsymbol{n}^\top \cdot \boldsymbol{x}_0}{\boldsymbol{n}^\top \cdot \boldsymbol{k}(0)}, \tag{3.12}$$

where $\boldsymbol{n}^\top = (1\ 0)$, $P = 1$, and $\boldsymbol{k}(0) = (\gamma_1 + \gamma_2, 1 + \beta)^\top$.

By comparing τ_0 and τ_1, the minimum positive time is the actual switching time τ.

STEP 3

By substituting τ to Eq. 3.8, $\boldsymbol{x}_1$ is explicitly calculated. Depending on the region $D(i)$ containing $\boldsymbol{x}_1$, $\boldsymbol{k}(i)$ is also obtained.

STEP 4

We substitute $\boldsymbol{x}_1$ into $\boldsymbol{x}_0$ and go to **STEP 2**.

Table 3.2 Vector $\boldsymbol{n}^\top$ and values of P.

	$\boldsymbol{n}^\top$	P
$x = 1$	(1 0)	1
$x = -1$	(1 0)	-1
$y = 1$	(0 1)	1
$y = -1$	(0 1)	-1

3.5 Determination of periodic solution

To conduct bifurcation analysis for the Arnol'd tongue, it is necessary to classify the periodic solution. The periodic solution can be obtained by using the local map.

Figure 3.5.1 shows the behavior of the periodic solutions projected on phase space. Assuming that the trajectory starting from $\boldsymbol{x}_0$ on the boundary $x = -1$ will return to itself in finite time as shown in Fig. 3.5.1(a). The trajectory passes through following regions:

$$D(0) \to D(1) \to D(3) \to D(2) \to D(0).$$

Here, we define a local map T_{ij} from region $D(i)$ to region $D(j)$. Let $\boldsymbol{x}_k$ be an initial point on $D(i)$, and $\boldsymbol{x}_{k+1}$ be a point at which the solution leaving $D(i)$ strikes $D(j)$. The local map T_{ij} that transforms a point on $D(i)$ to a point on $D(j)$ is defined as follows.

$$T_{ij} : D(i) \longrightarrow D(j), \quad \boldsymbol{x}_k \longmapsto \boldsymbol{x}_{k+1} = T_{ij}(\boldsymbol{x}_k). \tag{3.13}$$

Substituting Eq. 3.10 to Eq. 3.8 yields the following equation:

$$T_{ij}(\boldsymbol{x}_0) = \boldsymbol{x}_1 = \left(I_n - \frac{\boldsymbol{k}(i)\boldsymbol{n}^\top}{\boldsymbol{n}^\top \boldsymbol{k}(i)}\right)\boldsymbol{x}_0 + \frac{\boldsymbol{k}(i)P}{\boldsymbol{n}^\top \boldsymbol{k}(i)}, \tag{3.14}$$

where I_n denotes an identity matrix of dimension 2.

In general, we can recast Eq. 3.14 by

$$T_{ij}(\boldsymbol{x}_k) = \boldsymbol{x}_{k+1} = \left(I_n - \frac{\boldsymbol{k}(i)\boldsymbol{n}^\top}{\boldsymbol{n}^\top \boldsymbol{k}(i)}\right)\boldsymbol{x}_k + \frac{\boldsymbol{k}(i)P}{\boldsymbol{n}^\top \boldsymbol{k}(i)}, \tag{3.15}$$

Using the local map T_{ij}, we can determine the periodic solution in Fig. 3.5.1(a) as follows:

$$\begin{aligned}
&\boldsymbol{x}_1 = T_{01}(\boldsymbol{x}_0),\\
&\boldsymbol{x}_2 = T_{13}(\boldsymbol{x}_1) = T_{13} \circ T_{01}(\boldsymbol{x}_0),\\
&\boldsymbol{x}_3 = T_{32}(\boldsymbol{x}_2) = T_{32} \circ T_{13} \circ T_{01}(\boldsymbol{x}_0),\\
&\boldsymbol{x}_4 = T_{20}(\boldsymbol{x}_3) = T_{20} \circ T_{32} \circ T_{13} \circ T_{01}(\boldsymbol{x}_0),
\end{aligned} \tag{3.16}$$

where $\circ$ represents a composition of maps.

Noting that $\boldsymbol{x}_4$ is equal to $\boldsymbol{x}_0$, and solving Eq. 3.16 for $\boldsymbol{x}_0 = (-1, y_0)^\top$, we can obtain y_0 by

$$y_0 = -1 - 2\frac{k_{y2}}{k_{x2}} + 2\frac{k_{y2}k_{x3}}{k_{x2}k_{y3}} + 2\frac{k_{y2}k_{x3}k_{y1}}{k_{x2}k_{y3}k_{x1}} - \frac{k_{y2}k_{x3}k_{y1}k_{x0}}{k_{x2}k_{y3}k_{x1}k_{y0}}(1 - y_0), \tag{3.17}$$

where $\boldsymbol{k}(i) = (k_{x(i)}, k_{y(i)})^\top$ is listed in Table 3.1.

Similarly, we can determine the periodic solution in Fig. 3.5.1(b) by

$$\begin{aligned}
\boldsymbol{x}_1 &= T_{01}(\boldsymbol{x}_0),\\
\boldsymbol{x}_2 &= T_{12}(\boldsymbol{x}_1) = T_{12} \circ T_{01}(\boldsymbol{x}_0),\\
&\vdots\\
\boldsymbol{x}_8 &= T_{20}(\boldsymbol{x}_7)\\
&= T_{20} \circ T_{12} \circ T_{21} \circ T_{32} \circ T_{13} \circ T_{21} \circ T_{12} \circ T_{01}(\boldsymbol{x}_0),
\end{aligned} \tag{3.18}$$

If $\boldsymbol{x}_8$ is equal to $\boldsymbol{x}_0$, we obtain y_0 by solving Eq. 3.18 for $\boldsymbol{x}_0 = (-1, y_0)^\top$.

The stability of the periodic solutions can be determined by eigenvalues of the Jacobian matrix from composition of local map T_{ij}. The eigenvalue μ is a solution of following equation:

$$\det(\mu I_n - DT_{ij}^m) = 0, \tag{3.19}$$

where T_{ij}^m denotes m-fold compostion of T_{ij}; DT_{ij}^m is a Jacobian matrix of T_{ij}^m. If the largest value of $|\mu|$ is less than 1, the periodic solution is stable; otherwise, it is unstable.

Specifically, we consider the stability of the periodic solution shown in Fig. 3.5.1(a). The Jacobian matrix of 4-fold composition of T_{ij} is derived as follows:

$$DT_{ij}^4 = \begin{pmatrix} 0 & 0 \\ -\dfrac{k_{x3}k_{y1}k_{y2}}{k_{x1}k_{x2}k_{y3}} & -\dfrac{k_{x0}k_{x3}k_{y1}k_{y2}}{k_{x1}k_{x2}k_{y0}k_{y3}} \end{pmatrix}. \tag{3.20}$$

Eigenvalue of Eq. 3.20 is calculated by

$$\mu = \begin{pmatrix} \mu_1 \\ \mu_2 \end{pmatrix} = \begin{pmatrix} \dfrac{k_{x0}k_{x3}k_{y1}k_{y2}}{k_{x1}k_{x2}k_{y0}k_{y3}} \\ 0 \end{pmatrix} = \begin{pmatrix} \dfrac{111}{91} \\ 0 \end{pmatrix}. \tag{3.21}$$

Because $\mu_1 > 1$, the periodic solution is unstable.

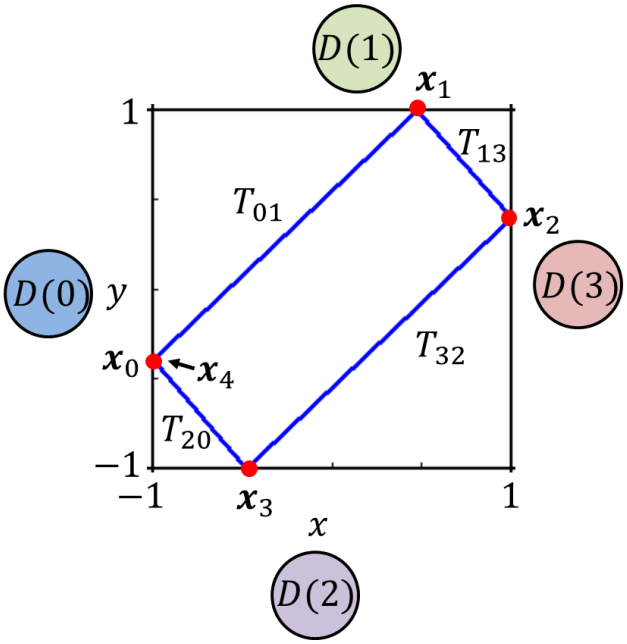

(a) $\beta = 2.5, \gamma_1 = 2.5, \gamma_2 = 1.2$

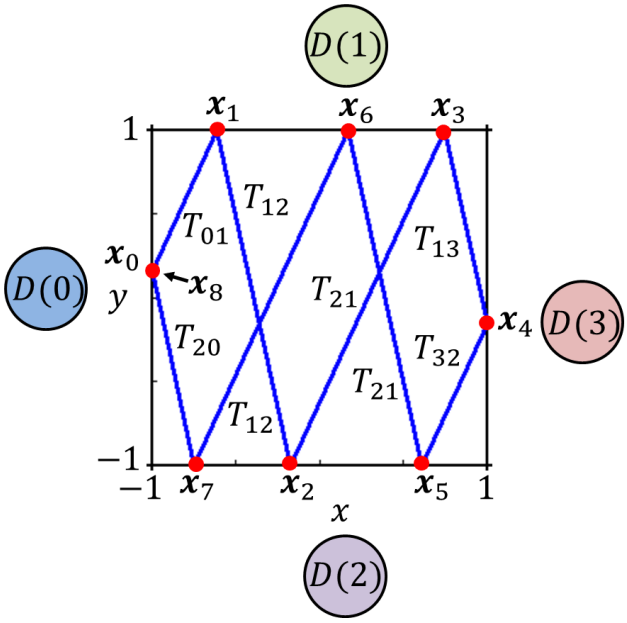

(b) $\beta = 7.0, \gamma_1 = 2.5, \gamma_2 = 1.2$

Figure 3.5.1 Local map.

3.6 Lyapunov analysis

In this section, we conduct Lyapunov analysis to determine the solutions as periodic or quasi-periodic by using the calculation algorithm, which is described in Section 3.4. Lyapunov exponent or Lyapunov characteristic exponent of a dynamical system expresses the rate how the solutions that are located in close proximity diverge or converge. Using Lyapunov exponent λ, the behavior of trajectory can be classified as follows:

- The solution is periodic if $\lambda < 0$.
- The solution is quasi-periodic if $\lambda = 0$.
- The solution is chaotic if $\lambda > 0$.

The computational algorithm of Lyapunov exponent has been reported in many literatures such as Ref. [62,63]. To calculate the Lyapunov, we use the procedure of derivation Lyapunov exponent in Ref. [63].

At first, we conduct the Jacobian matrices. It is clear from Eq. 3.14 that the local Jacobian matrix is represented by

$$A = \frac{\mathrm{d}\boldsymbol{x}_1}{\mathrm{d}\boldsymbol{x}_0} = I_n - \frac{\boldsymbol{k}(i)\boldsymbol{n}^\top}{\boldsymbol{n}^\top \boldsymbol{k}(i)}. \tag{3.22}$$

Then, if the solution strikes $x = 1$ or $x = -1$,

$$A_0 = \begin{pmatrix} 0 & 0 \\ -k_{yi}/k_{xi} & 1 \end{pmatrix}, \tag{3.23}$$

if the solution strikes $y = 1$ or $y = -1$,

$$A_1 = \begin{pmatrix} 1 & -k_{xi}/k_{yi} \\ 0 & 0 \end{pmatrix}. \tag{3.24}$$

Next, based on the procedure of calculating Lyapunov exponent in Ref. [63], we use Eq. (3.14) and (3.22) to define the first and the second Lyapunov exponent as follows.

$$\begin{aligned} \lambda_1 &\simeq \frac{1}{N} \sum_{j=M+1}^{M+N} \ln \left| A_i^j e_1^j \right|, \\ \lambda_1 + \lambda_2 &\simeq \frac{1}{N} \sum_{j=M+1}^{M+N} \ln \left| A_i^j e_1^j \times A_i^j e_2^j \right|, \end{aligned} \tag{3.25}$$

where e_1^j and e_2^j are orthonormal bases, and $A_i^j = \dfrac{\mathrm{d}\boldsymbol{x}_1}{\mathrm{d}\boldsymbol{x}_0}$ is the Jacobian matrix, which is one of A_0 and A_1. M and N are integers. It is reasonable to argue that for $M = N = 2 \times 10^7$ the two Lyapunov exponents converge to zero. Therefore, Lyapunov exponent can be regarded to be zero if calculated exponent satisfies following condition.

$$|\lambda_i| < 1/10^6. \tag{3.26}$$

We use the first Lyapunov exponent to conduct a two-parameter Lyapunov diagram as shown in Fig. 3.6.1. A continuous deformation method is used when the bifurcation parameters are varied. Parameter β is varied from β_{present} to β_{next} as tracing parameter from left-hand side to right-hand side ($\beta_{\text{present}} < \beta_{\text{next}}$). The relationship between β_{present} and β_{next} is described by

$$\beta_{\text{next}} = \beta_{\text{present}} + \Delta\beta, \tag{3.27}$$

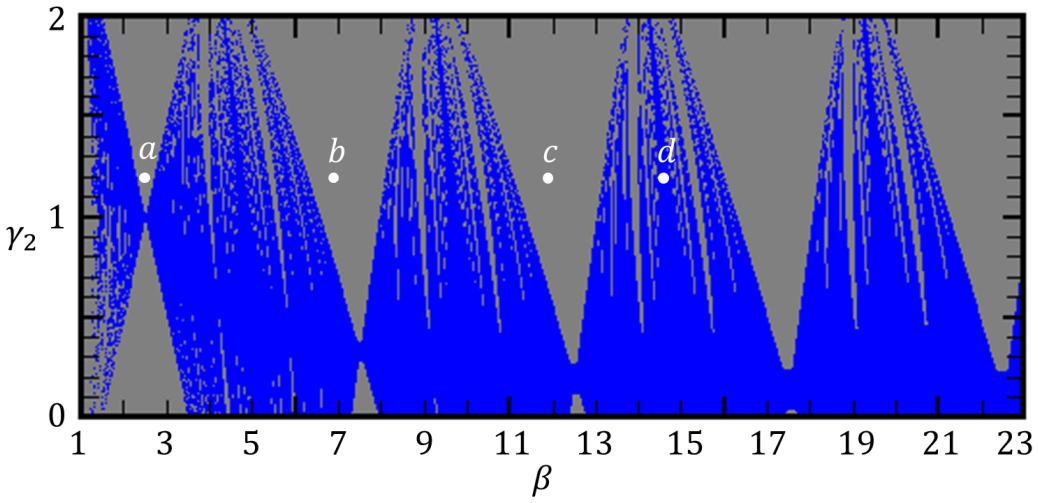

Figure 3.6.1 Two-parameter Lyapunov diagram ($\gamma_1 = 2.5$).

where $\Delta\beta$ is chosen to be small ($0 < \Delta\beta < 1$).

The final value $\big(x_1, y_1, h_1(x_1), h_2(y_1)\big)$ at β_{present} is substituted into the initial value $\big(x_0, y_0, h_1(x_0), h_2(y_0)\big)$ at β_{next}. Subsequently, let β_{present} be replaced by β_{next}. This procedure is repeated untill β reaches the final value at $\beta = 23$. Parameter value γ_2 is traced in the same procedure as varying β.

In the Fig. 3.6.1, the regions generating periodic ($\lambda < 0$) and quasi-periodic solutions ($\lambda = 0$) are marked by gray and blue, respectively. Points a–c indicate various types of periodic oscillation as shown in Fig. 3.3.2, Fig. 3.3.3, and Fig. 3.3.4. These regions are known to be synchronization regions, or Arnol'd tongues. Outside the Arnol'd tongues, quasi-periodic oscillation is observed as shown in Fig. 3.3.5, which is marked by point d in Fig. 3.6.1.

3.7 Analysis of Arnol'd tongues

3.7.1 1-D return map

We now derive the mechanism causing the generation of Arnol'd tongues in detail for the two-coupled PWCOs using the 1-D return map.

First, we define 4 subsets of solutions as follows.

$$A = \{x, y, h_1(x), h_2(y) \mid -1 \leq x \leq 1, y = -1\}. \tag{3.28}$$

$$B = \{x, y, h_1(x), h_2(y) \mid -1 \leq y \leq 1, x = -1\}. \tag{3.29}$$

$$C = \{x, y, h_1(x), h_2(y) \mid -1 \leq x \leq 1, y = 1\}. \tag{3.30}$$

$$D = \{x, y, h_1(x), h_2(y) \mid -1 \leq y \leq 1, x = 1\}. \tag{3.31}$$

Noting that, each subset includes two pairs of hysteresis element. For instance, we consider the case that the solution of the trajectory is on A. Meanwhile $h_2(y) = 1$, $h_1(x)$ takes two values: -1 or 1. Thus, the trajectory starting from A contains $\boldsymbol{k}(0) = (k_{x0}, k_{y0})^\top$ or $\boldsymbol{k}(2) = (k_{x2}, k_{y2})^\top$.

Second, we consider that the trajectory containing $\boldsymbol{k}(2) = (k_{x2}, k_{y2})^\top$ starts from point $\boldsymbol{x}_0 = (x_0, y_0)^\top = (x_0, -1)^\top$ on A. Depending on the location of x_0, the trajectory will strike B or C as shown in Fig. 3.7.1. Let $\boldsymbol{x}_{th} = (x_{th}, -1)^\top$ be a point on A such that the trajectory starting from $\boldsymbol{x}_{th} = (x_{th}, -1)^\top$ strikes a point $\boldsymbol{x}_1 = (-1, 1)^\top$, which is a intersection point of B and C. Based on Eq. 3.8, x_{th} is calculated by

$$x_{th} = -1 - 2\frac{k_{x2}}{k_{y2}}. \tag{3.32}$$

It is clearly that if $x_0 < x_{th}$ the trajectory starting from point $\boldsymbol{x}_0 = (x_0, -1)^\top$ will reach B at $\boldsymbol{x}_1 = (-1, y_B)^\top$. In constrast, if $x_0 \geq x_{th}$ the trajectory will reach C at $\boldsymbol{x}_1 = (x_C, 1)^\top$. By using Eq. 3.8 and Eq. 3.10, x_C and y_B are calculated manually as follows.

$$\begin{aligned} x_C &= x_0 + 2\frac{k_{x2}}{k_{y2}} && \text{for} \quad x_0 \geq -1 - 2\frac{k_{x2}}{k_{y2}}, \\ y_B &= -1 - \frac{k_{y2}}{k_{x2}}(1 + x_0) && \text{for} \quad x_0 < -1 - 2\frac{k_{x2}}{k_{y2}}. \end{aligned} \tag{3.33}$$

Similarly, the trajectory containing $\boldsymbol{k}(0) = (k_{x0}, k_{y0})^\top$ that leaves $\boldsymbol{x}_0 = (x_0, y_0)^\top = (x_0, -1)^\top$ on A will hit C at $\boldsymbol{x}_1 = (x_1, y_1)^\top = (x_C, 1)^\top$ or D at $\boldsymbol{x}_1 = (x_1, y_1)^\top = (1, y_D)^\top$. Then,

$$\begin{aligned} x_C &= x_0 + 2\frac{k_{x0}}{k_{y0}} && \text{for} \quad x_0 < 1 - 2\frac{k_{x0}}{k_{y0}}, \\ y_D &= -1 + \frac{k_{y0}}{k_{x0}}(1 - x_0) && \text{for} \quad x_0 \geq 1 - 2\frac{k_{x0}}{k_{y0}}. \end{aligned} \tag{3.34}$$

In a similar manner, we can derive two-routes of the trajectory on each subset. The trajectory started from $\boldsymbol{x}_0 = (x_0, y_0)^\top = (-1, y_0)^\top$ on B:

- The trajectory containing $\boldsymbol{k}(0) = (k_{x0}, k_{y0})^\top$ will hit C at $\boldsymbol{x}_1 = (x_1, y_1)^\top = (x_C, 1)^\top$ or D at $\boldsymbol{x}_1 = (x_1, y_1)^\top = (1, y_D)^\top$. Then,

$$\begin{aligned} x_C &= -1 + \frac{k_{x0}}{k_{y0}}(1 - y_0) && \text{for} \quad y_0 \geq 1 - 2\frac{k_{y0}}{k_{x0}}, \\ y_D &= y_0 + 2\frac{k_{y0}}{k_{x0}} && \text{for} \quad y_0 < 1 - 2\frac{k_{y0}}{k_{x0}}. \end{aligned} \tag{3.35}$$

- The trajectory containing $\boldsymbol{k}(1) = (k_{x1}, k_{y1})^\top$ will hit A at $\boldsymbol{x}_1 = (x_1, y_1)^\top =$

$(x_A, -1)^\top$ or D at $\boldsymbol{x}_1 = (x_1, y_1)^\top = (1, y_D)^\top$. Then,

$$\begin{aligned} x_A &= -1 - \frac{k_{x1}}{k_{y1}}(1 + y_0) \quad \text{for} \quad y_0 < -1 - 2\frac{k_{y1}}{k_{x1}}, \\ y_D &= y_0 + 2\frac{k_{y1}}{k_{x1}} \qquad\quad \text{for} \quad y_0 \geq -1 - 2\frac{k_{y1}}{k_{x1}}. \end{aligned} \tag{3.36}$$

The trajectory started from $\boldsymbol{x}_0 = (x_0, y_0)^\top = (x_0, 1)^\top$ on C:

- The trajectory containing $\boldsymbol{k}(1) = (k_{x1}, k_{y1})^\top$ will hit D at $\boldsymbol{x}_1 = (x_1, y_1)^\top = (1, y_D)^\top$ or A at $\boldsymbol{x}_1 = (x_1, y_1)^\top = (x_A, -1)^\top$. Then,

$$\begin{aligned} x_A &= x_0 - 2\frac{k_{x1}}{k_{y1}} \qquad\quad \text{for} \quad x_0 < 1 + 2\frac{k_{x1}}{k_{y1}}, \\ y_D &= 1 + \frac{k_{y1}}{k_{x1}}(1 - x_0) \quad \text{for} \quad x_0 \geq 1 + 2\frac{k_{x1}}{k_{y1}}. \end{aligned} \tag{3.37}$$

- The trajectory containing $\boldsymbol{k}(3) = (k_{x3}, k_{y3})^\top$ will hit A at $\boldsymbol{x}_1 = (x_1, y_1)^\top = (x_A, -1)^\top$ or B at $\boldsymbol{x}_1 = (x_1, y_1)^\top = (-1, y_B)^\top$. Then,

$$\begin{aligned} x_A &= x_0 - 2\frac{k_{x3}}{k_{y3}} \qquad\quad \text{for} \quad x_0 \geq -1 + 2\frac{k_{x3}}{k_{y3}}, \\ y_B &= 1 - \frac{k_{y3}}{k_{x3}}(1 + x_0) \quad \text{for} \quad x_0 < -1 + 2\frac{k_{x3}}{k_{y3}}. \end{aligned} \tag{3.38}$$

The trajectory started from $\boldsymbol{x}_0 = (x_0, y_0)^\top = (1, y_0)^\top$ on D:

- The trajectory containing $\boldsymbol{k}(3) = (k_{x3}, k_{y3})^\top$ will hit A at $\boldsymbol{x}_1 = (x_1, y_1)^\top = (x_A, -1)^\top$ or B at $\boldsymbol{x}_1 = (x_1, y_1)^\top = (-1, y_B)^\top$. Then,

$$\begin{aligned} x_A &= 1 - \frac{k_{x3}}{k_{y3}}(1 + y_0) \quad \text{for} \quad y_0 < -1 + 2\frac{k_{y3}}{k_{x3}}, \\ y_B &= y_0 - 2\frac{k_{y3}}{k_{x3}} \qquad\quad \text{for} \quad y_0 \geq -1 + 2\frac{k_{y3}}{k_{x3}}. \end{aligned} \tag{3.39}$$

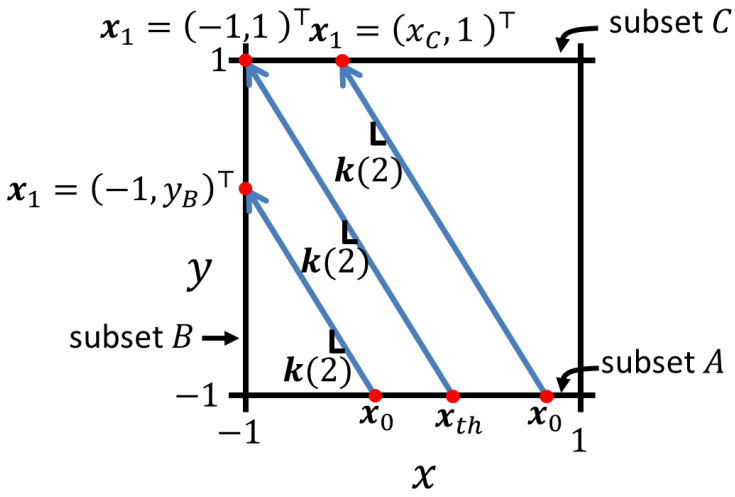

Figure 3.7.1 Two routes of the trajectory on A.

- The trajectory containing $\boldsymbol{k}(2) = (k_{x2}, k_{y2})^\top$ will hit B at $\boldsymbol{x}_1 = (x_1, y_1)^\top = (-1, y_B)^\top$ or C at $\boldsymbol{x}_1 = (x_1, y_1)^\top = (x_C, 1)^\top$. Then,

$$\begin{aligned} y_B &= y_0 - 2\frac{k_{y2}}{k_{x2}} \qquad \text{for} \quad y_0 < 1 + 2\frac{k_{y2}}{k_{x2}}, \\ x_C &= 1 + \frac{k_{x2}}{k_{y2}}(1 - y_0) \quad \text{for} \quad y_0 \geq 1 + 2\frac{k_{y2}}{k_{x2}}. \end{aligned} \tag{3.40}$$

In order to derive 1-D return map, we define a domain L as follows.

$$\begin{aligned} L =&\{x, y, h_1(x), h_2(y) \mid -1 \leq y \leq 1, x = -1, h_1(x) = 1, h_2(y) = 1\} \\ &\cup\{x, y, h_1(x), h_2(y) \mid -1 \leq x \leq 1, y = -1, h_1(x) = 1, h_2(y) = 1\}. \end{aligned} \tag{3.41}$$

Noting that, domain L is corresponding to subset A and B, on which the trajectory is always containing $\boldsymbol{k}(0)$. The trajectory leaving L eventually return to L.

We introduce a dummy variable θ to represent a point on domain L. Hence, solution x on A and y on B will be assigned to θ by following equation:

$$\begin{aligned} \theta &= 0 + (1 + x), \\ \theta &= 2 + (1 + y). \end{aligned} \tag{3.42}$$

Since $-1 \leq x \leq 1$ and $-1 \leq y \leq 1$, subset A and B is assigned to space $[0, 2)$ and space $[2, 4]$, respectively. Let θ_0 be an initial point on L and θ_1 be a point on L at which the solution leaving L returns. The 1-D return map F is defined as follows.

$$F : [0, 4] \longrightarrow [0, 4], \qquad \theta_n \longmapsto \theta_{n+1} = F(\theta_n). \tag{3.43}$$

Figure 3.7.2 shows an example of 1-D return map. Figure 3.7.3 is an example of quasi-periodic trajectory.

In order to discuss bifurcation phenomena, we give the following definition. *Definition*: $\theta_n \in L$ is called a p-periodic point with period p if $\theta_n = F^p(\theta_n)$ and $\theta_n \neq F^k(\theta_n)$ for $0 < k < p$, where F^p denotes the p-times composition of F.

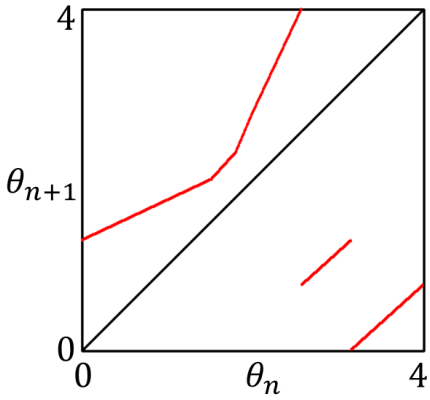

Figure 3.7.2 Example of 1-D return map ($\gamma_1 = 2.5, \gamma_2 = 1.2, \beta = 3.1$).

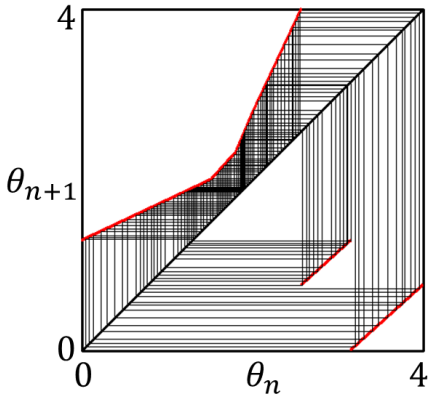

Figure 3.7.3 Quasi-periodic attractor ($\gamma_1 = 2.5, \gamma_2 = 1.2, \beta = 3.1$).

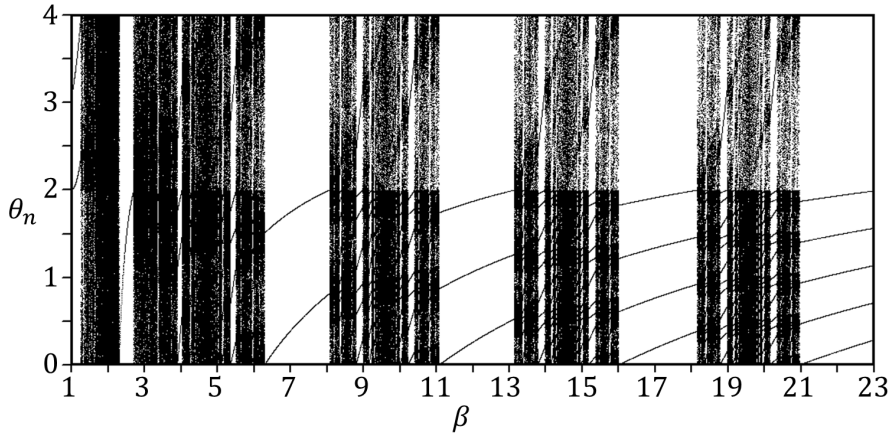

Figure 3.7.4 One-parameter bifurcation diagram of F ($\gamma_1 = 2.5, \gamma_2 = 1.2$).

We fixed the parameter values $\gamma_1 = 2.5$ and $\gamma_2 = 1.2$. One-parameter bifurcation diagram is obtained when the bifurcation parameter varies β along the horizontal axis as shown in Fig. 3.7.4. A continuous deformation method, which is mentioned in section 3.7.2, is used to trace the bifurcation parameter β from left to right. For each parameter value of β, after transient time, a set of state variables θ_n on domain L are plotted for 10^3 iterations on the vertical axis.

We can see that for β close to 2.5, the diagram shows one point on domain L. This one point attractor corresponds to obtained periodic attractor as shown in Fig. 3.3.2. Similarly, for β close to $7, 12, 17$ and 22, the diagram shows two, three, four and five points attractor, respectively. The two and three points attractor correspond to obtained attractor shown in Fig. 3.3.3 and Fig. 3.3.4. These periodic regions correspond to Arnol'd tongues marked by gray in Fig. 3.6.1.

3.7.2 Derivation of the Arnol'd tongue boundaries

Next, we explain the mechanism causing the Arnol'd tongues. For simplicity, we derive the boundaries of Arnol'd tongue of periodic solutions with period one and two. Figure 3.7.5 shows magnified view of the two-parameter bifurcation diagram shown in Fig. 3.6.1. The boundaries are marked by black lines. Figure 3.7.6 shows magnified view of the one-parameter bifurcation diagram in Fig. 3.7.4.

Figures 3.7.7, 3.7.8, and 3.7.9 show 1-D return maps obtained at the parameter values marked A_1, B_1, and C_1 in Fig. 3.7.5, respectively. Stable fixed point θ_{n_s} and unstable fixed point θ_{n_u} coexist in Fig. 3.7.7. They are brought together as β increasing and merge at $\theta_n = 2$ in Fig. 3.7.8. Afterward, they disappear as shown in Fig. 3.7.9. This bifurcation is called non-smooth tangent (ab. NsT) bifurcation.

Noting that, stable fixed point θ_{n_s} and unstable fixed point θ_{n_u} is on the subset A and B, respectively. Thus, using Eq. 3.42, we can obtain x_s and y_u, which is corresponding stable fixed point θ_{n_s} and θ_{n_u}, respectively. Figures 3.7.10, 3.7.11, and 3.7.12 show attractor corresponding to the 1-D return maps in Fig. 3.7.7, 3.7.8, and 3.7.9, respectively. There exists a periodic attractor with stable fixed point x_s and unstable fixed point y_u in Fig. 3.7.10. As β increases, x_s collides y_u at the intersection point of the boundary $x = -1$ and the boundary $y = -1$ as shown in Fig. 3.7.11. Thus, we can obtain $x_s = y_u = -1$, which

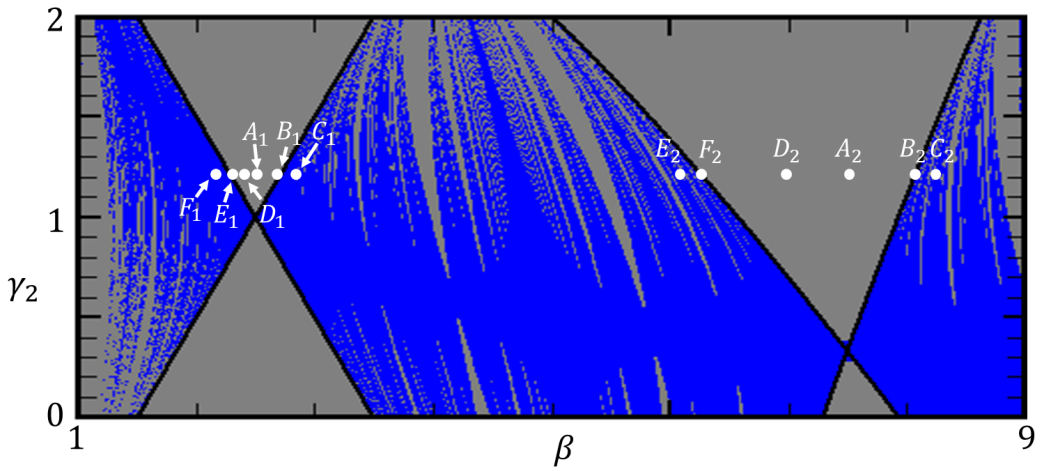

Figure 3.7.5 Magnified view of the two-parameter bifurcation diagram in Fig. 3.6.1 ($\gamma_1 = 2.5$).

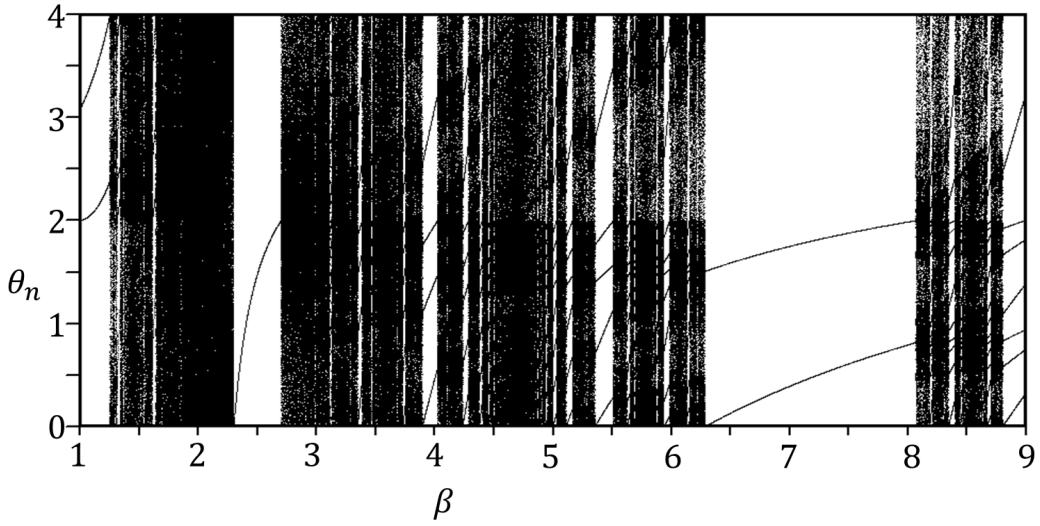

Figure 3.7.6 Magnified view of the one-parameter bifurcation diagram in Fig. 3.7.4 ($\gamma_1 = 2.5, \gamma_2 = 1.2$).

is correspond to $\theta_{n\_s} = \theta_{n\_u} = 2$ in Fig. 3.7.8. This parameter value is called bifurcation point. After pass the bifurcation point, F has no fixed point and a quasi-periodic attractor emerges as shown in Fig. 3.7.12.

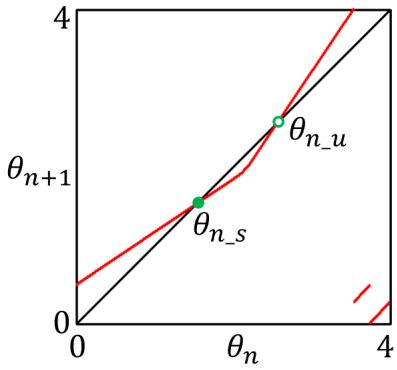

Figure 3.7.7 1-D return map F at A_1 in Fig. 3.7.5 $(\beta = 2.5, \gamma_1 = 2.5, \gamma_2 = 1.2)$.

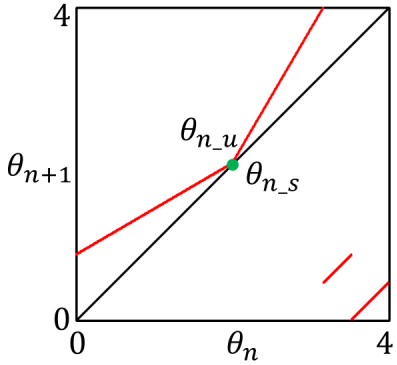

Figure 3.7.8 1-D return map F at B_1 in Fig. 3.7.5 $(\beta = 2.7, \gamma_1 = 2.5, \gamma_2 = 1.2)$.

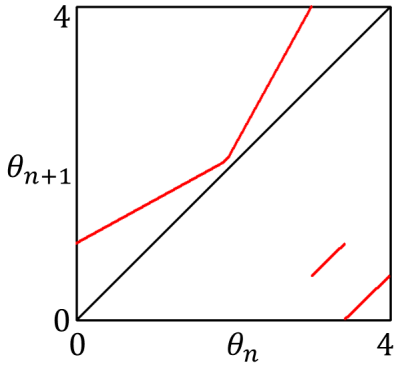

Figure 3.7.9 1-D return map F at C_1 in Fig. 3.7.5 $(\beta = 2.8, \gamma_1 = 2.5, \gamma_2 = 1.2)$.

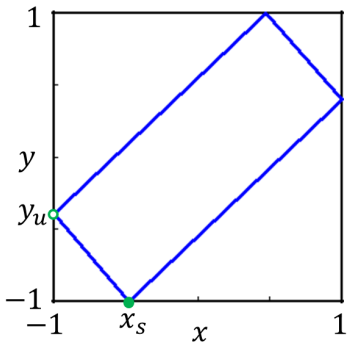

Figure 3.7.10 Periodic attractor with period one obtained at A_1 in Fig. 3.7.5 ($\beta = 2.5, \gamma_1 = 2.5, \gamma_2 = 1.2$).

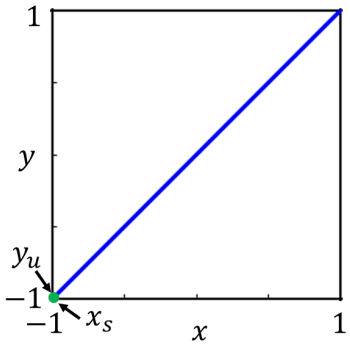

Figure 3.7.11 NsT bifurcation occurring at B_1 in Fig. 3.7.5 ($\beta = 2.7, \gamma_1 = 2.5, \gamma_2 = 1.2$).

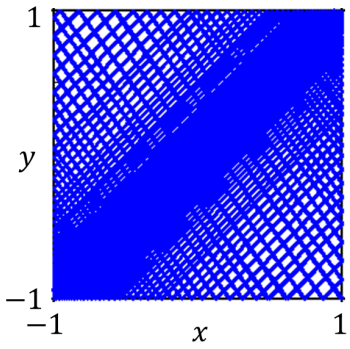

Figure 3.7.12 Quasi-periodic attractor obtained at C_1 in Fig. 3.7.5 ($\beta = 2.8, \gamma_1 = 2.5, \gamma_2 = 1.2$).

Furthermore, we demonstrate the bifurcation structure when β decreases. Figures 3.7.13, 3.7.14, and 3.7.15 show 1-D return maps obtained at parameter values marked D_1, E_1, and F_1 in Fig. 3.7.5, respectively. Figures 3.7.16, 3.7.17, and 3.7.18 show the attractors corresponding to the 1-D return maps shown in Fig. 3.7.13, 3.7.14, and 3.7.15, respectively.

The two fixed points in Fig. 3.7.13 move to the opposite directions as β decreases. They hit the point $\theta_{n\_s} = 0$ (or $\theta_{n\_u} = 4$) as shown in Fig. 3.7.14, which corresponds to $x_s = 1$ (or $y_u = 1$, respectively) in Fig. 3.7.17. Figure 3.7.18 shows a quasi-periodic attractor observed after the bifurcation.

It is clear that the bifurcation begins at $\beta = 2.3$ and finishes at $\beta = 2.7$ as shown in Fig. 3.7.4 corresponding to points marked E_1 and B_1, respectively, as shown in Fig. 3.7.5. The left-hand side bifurcation boundary marked by green is obtained by solving the following equation:

$$x_s = y_u = -1. \tag{3.44}$$

The right-hand side bifurcation boundary marked by white is obtained by solving the following equation.

$$x_s = y_u = 1. \tag{3.45}$$

Using Eq. 3.15 and Eq. 3.18, x_s and y_u can be calculated explicitly as follows.

$$x_s = -1 - 2\frac{k_{x1}}{k_{y1}} + 2\frac{k_{x1}k_{y3}}{k_{y1}k_{x3}} + 2\frac{k_{x1}k_{y3}k_{x2}}{k_{y1}k_{x3}k_{y2}} - \frac{k_{x1}k_{y3}k_{x2}k_{y0}}{k_{y1}k_{x3}k_{y2}k_{x0}}(1 - x_s). \tag{3.46}$$

$$y_u = -1 - 2\frac{k_{y2}}{k_{x2}} + 2\frac{k_{y2}k_{x3}}{k_{x2}k_{y3}} + 2\frac{k_{y2}k_{x3}k_{y1}}{k_{x2}k_{y3}k_{x1}} - \frac{k_{y2}k_{x3}k_{y1}k_{x0}}{k_{x2}k_{y3}k_{x1}k_{y0}}(1 - y_u). \tag{3.47}$$

By solving Eq. 3.44, the left-hand side of bifurcation boundary is obtained as

$$\gamma_1 + \gamma_2 = \beta + 1. \tag{3.48}$$

By solving Eq. 3.45, the right-hand side of bifurcation boundary is obtained as

$$\gamma_1 - \gamma_2 = \beta - 1. \tag{3.49}$$

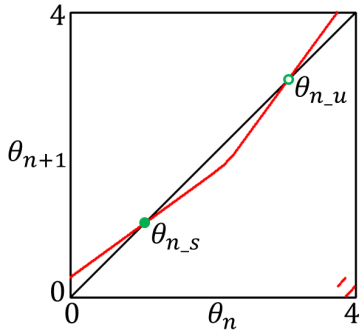

Figure 3.7.13 1-D return map F at D_1 in Fig. 3.7.5 $(\beta = 2.4, \gamma_1 = 2.5, \gamma_2 = 1.2)$.

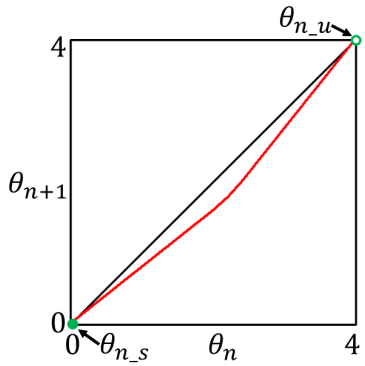

Figure 3.7.14 1-D return map F at E_1 in Fig. 3.7.5 $(\beta = 2.3, \gamma_1 = 2.5, \gamma_2 = 1.2)$.

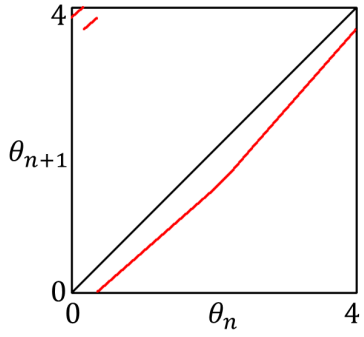

Figure 3.7.15 1-D return map F at F_1 in Fig. 3.7.5 $(\beta = 2.2, \gamma_1 = 2.5, \gamma_2 = 1.2)$.

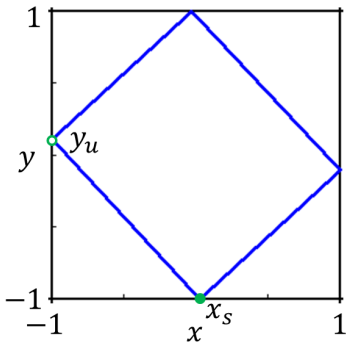

Figure 3.7.16 Periodic attractor with period one obtained at D_1 in Fig. 3.7.5 ($\beta = 2.4, \gamma_1 = 2.5, \gamma_2 = 1.2$).

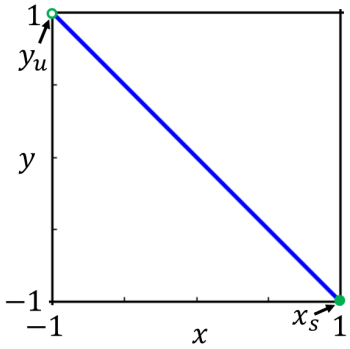

Figure 3.7.17 NsT bifurcation occurring at E_1 in Fig. 3.7.5 ($\beta = 2.3, \gamma_1 = 2.5, \gamma_2 = 1.2$).

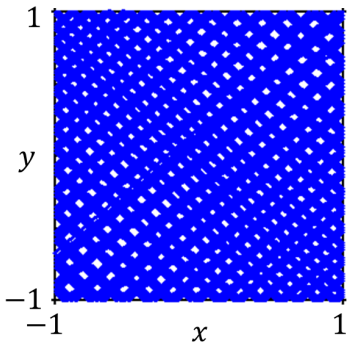

Figure 3.7.18 Quasi-periodic attractor obtained at F_1 in Fig. 3.7.5 ($\beta = 2.2, \gamma_1 = 2.5, \gamma_2 = 1.2$).

To derive Arnol'd tongue boundaries of the solution with period two, we investigate two-times composition of 1-D return map. Figures 3.7.19, 3.7.20, and 3.7.21 show 1-D return map obtained at parameter values marked A_2, B_2, and C_2 in Fig. 3.7.5, respectively. There exist two pairs of stable and unstable fixed points as shown in Fig. 3.7.19. A non-smooth tangent bifurcation occurs when the stable and unstable fixed points θ_{n_s1} and θ_{n_u1} merge together as shown in Fig. 3.7.20. Thus, the bifurcation equation for this is given by

$$\theta_{n+1} = \theta_n = 2. \tag{3.50}$$

Moreover, θ_{n_s1}, θ_{n_u1}, θ_{n_s2}, and θ_{n_u2} correspond to x_{s1}, y_{u1}, x_{s2}, and x_{u2}, respectively. Hence, Eq. 3.50 is rewritten as follows.

$$y_{u1} = x_{s1} = -1. \tag{3.51}$$

Furthermore, we investigate the bifurcation structure when β decreases. Figures 3.7.25, 3.7.26, and 3.7.27 show 1-D return maps obtained at the parameter values marked D_2, E_2, and F_2 in Fig. 3.7.5, respectively. Figures 3.7.28, 3.7.29, and 3.7.30 show the attractors corresponding to 1-D return maps in Fig. 3.7.25, 3.7.26, and 3.7.27, respectively. The bifurcation occurs when $\theta_{n\_s2} = 0$ (or $\theta_{n\_u1} = 4$). Thus, using Eq. 3.42, we can obtain

$$x_{s2} = y_{u1} = 1. \tag{3.52}$$

Using Eq. 3.15 and Eq. 3.18, x_{s2} are calculated explicitly as follows:

$$\left(\frac{k_{x1}k_{x2}k_{y0}k_{y3}}{k_{x0}k_{x3}k_{y1}k_{y2}}-1\right)x_{s2}= \frac{k_{x1}k_{x2}k_{y0}k_{y3}}{k_{x0}k_{x3}k_{y1}k_{y2}}-\frac{6k_{x1}k_{x2}k_{y3}}{k_{x3}k_{y1}k_{y2}}+\frac{2k_{x1}^2k_{x2}k_{y0}k_{y3}}{k_{x0}k_{x3}k_{y1}^2k_{y2}} -\frac{2k_{x1}k_{y3}}{k_{x3}k_{y1}}+\frac{4k_{x1}}{k_{y1}}+1. \tag{3.53}$$

By solving Eq. 3.51 for x_{s2}, the left-hand side of bifurcation boundary is explicitly obtained as

$$2\beta=\gamma_1+\gamma_2+\sqrt{(\gamma_1+\gamma_2)^2-4(\gamma_1+\gamma_2-1)}. \tag{3.54}$$

By solving Eq. 3.52 for y_{u1}, the right-hand side of bifurcation boundary is also explicitly obtained as

$$2\beta=\gamma_1-\gamma_2+\sqrt{(\gamma_1-\gamma_2)^2-4(-\gamma_1+\gamma_2-1)}. \tag{3.55}$$

Similarly, we can obtain the bifurcation boundary for a periodic attractor with period $n+2$, where $n=0,1,2,...$

The left-hand side of bifurcation boundaries is explicitly obtained as follows:

$$2\beta=(2n+1)\gamma_1+\gamma_2+\sqrt{\big((2n+1)\gamma_1+\gamma_2\big)^2-4\big(\gamma_1+(2n+1)\gamma_2-1\big)}. \tag{3.56}$$

The right-hand side of bifurcation boundaries is also explicitly obtained as follows:

$$2\beta=(2n+1)\gamma_1-\gamma_2+\sqrt{\big((2n+1)\gamma_1-\gamma_2\big)^2-4\big(-\gamma_1+(2n+1)\gamma_2-1\big)}. \tag{3.57}$$

The bifurcation boundaries of Arnol'd tongues in the two-parameter Lyapunov diagram are shown in Fig. 3.7.31. The boundaries between the regions generating periodic solution and regions generating quasi-periodic solution obtained by

using Lyapunov analysis coincide with the bifurcation curves using 1-D return map.

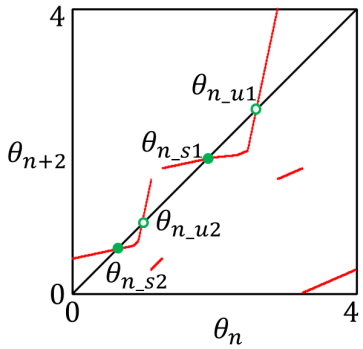

Figure 3.7.19 1-D return map F at A_2 in Fig. 3.7.5 $(\beta = 7.5, \gamma_1 = 2.5, \gamma_2 = 1.2)$.

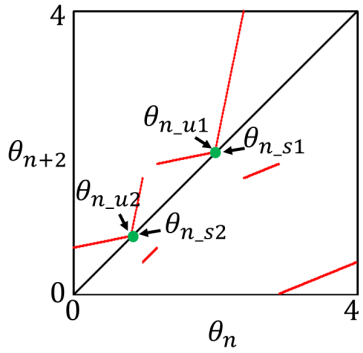

Figure 3.7.20 1-D return map F at B_2 in Fig. 3.7.5 $(\beta \cong 8.06786, \gamma_1 = 2.5, \gamma_2 = 1.2)$.

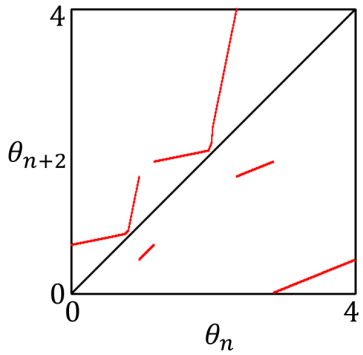

Figure 3.7.21 1-D return map F at C_2 in Fig. 3.7.5 $(\beta = 8.15, \gamma_1 = 2.5, \gamma_2 = 1.2)$.

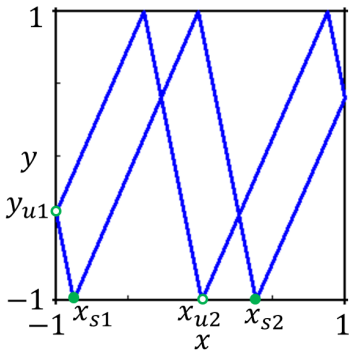

Figure 3.7.22 Periodic attractor with period two obtained at A_2 in Fig. 3.7.5 ($\beta = 7.5, \gamma_1 = 2.5, \gamma_2 = 1.2$).

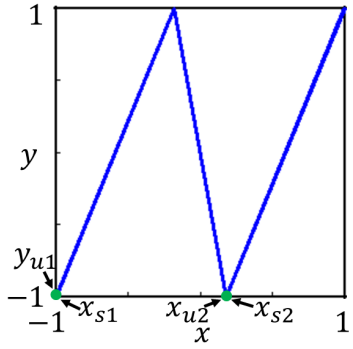

Figure 3.7.23 NsT bifurcation occurring at B_2 in Fig. 3.7.5 ($\beta \cong 8.06786, \gamma_1 = 2.5, \gamma_2 = 1.2$).

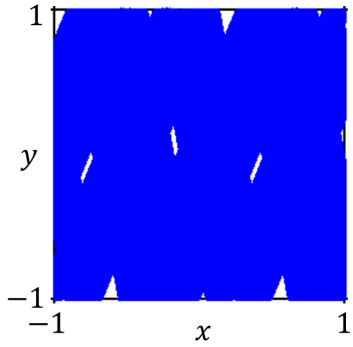

Figure 3.7.24 Quasi-periodic attractor obtained at C_2 in Fig. 3.7.5 ($\beta = 8.15, \gamma_1 = 2.5, \gamma_2 = 1.2$).

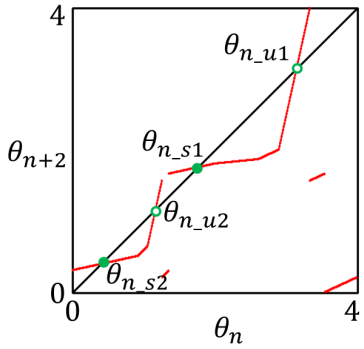

Figure 3.7.25 1-D return map F at D_2 in Fig. 3.7.5 ($\beta = 7.0, \gamma_1 = 2.5, \gamma_2 = 1.2$).

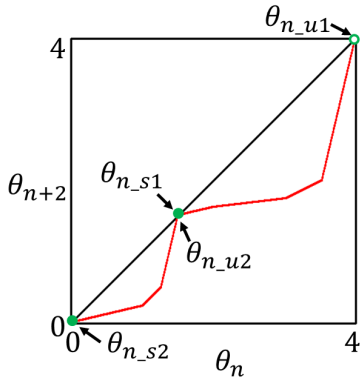

Figure 3.7.26 1-D return map F at E_2 in Fig. 3.7.5 ($\beta \cong 6.28408, \gamma_1 = 2.5, \gamma_2 = 1.2$).

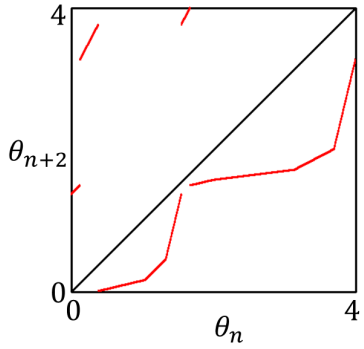

Figure 3.7.27 1-D return map F at F_2 in Fig. 3.7.5 ($\beta = 6.1, \gamma_1 = 2.5, \gamma_2 = 1.2$).

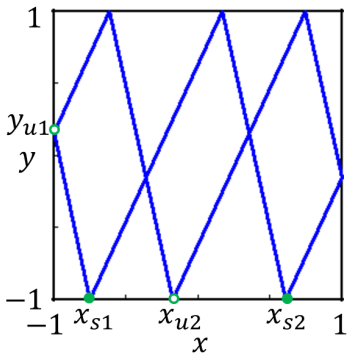

Figure 3.7.28 Periodic attractor with period two obtained at D_2 in Fig. 3.7.5 ($\beta = 7.0, \gamma_1 = 2.5, \gamma_2 = 1.2$).

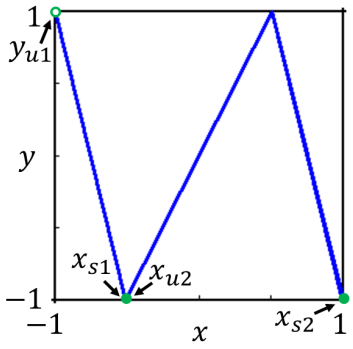

Figure 3.7.29 NsT bifurcation occurring at E_2 in Fig. 3.7.5 ($\beta \cong 6.28408, \gamma_1 = 2.5, \gamma_2 = 1.2$).

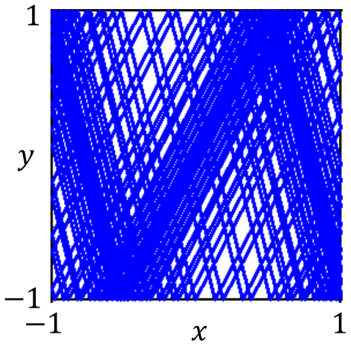

Figure 3.7.30 Quasi-periodic attractor obtained at F_2 in Fig. 3.7.5 ($\beta = 6.1, \gamma_1 = 2.5, \gamma_2 = 1.2$).

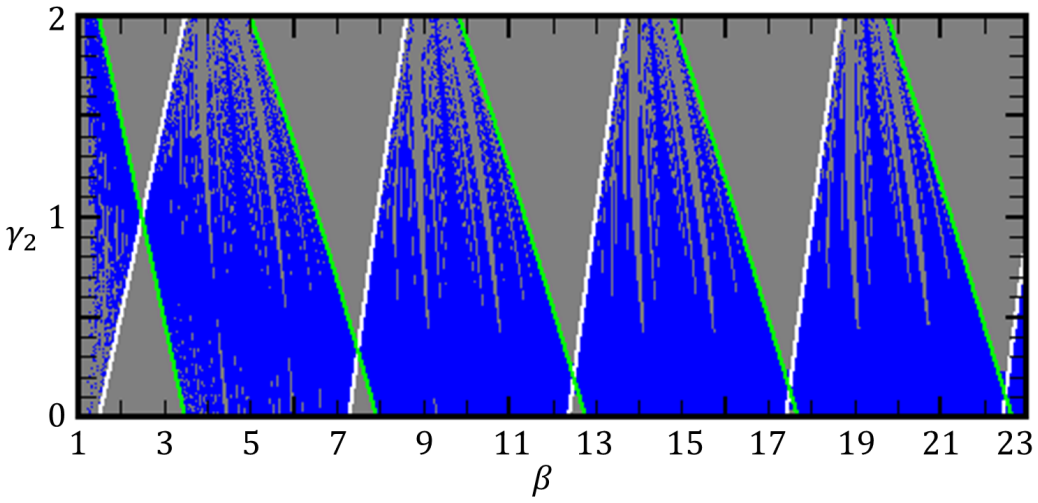

Figure 3.7.31 Boundaries of Arnol'd tongues in two-parameter bifurcation diagram ($\gamma_1 = 2.5$).

3.8 Conclusions

We analyzed bifurcation structures of an autonomous two-coupled PWCOs. Arnol'd tongues are observed in a two-parameter bifurcation diagram by a Lyapunov analysis using explicit solutions. Several bifurcation boundaries of Arnol'd tongues are explicitly derived using a 1-D return map. We explain that Arnol'd tongues occur as a result of non-smooth tangent bifurcation. The Arnol'd tongues occurring in this system is similar to that of the fundamental PWCO driven by a rectangular wave force in Ref [24]. In future work, we plan to discuss the entire bifurcation sets of the system.

Chapter 4

Arnol'd Resonance Web and Chenciner Bubbles Generated in Two-coupled Piecewise-Constant Oscillators Driven by a Rectangular Wave Forcing

4.1 Introduction

Quasi-periodic oscillations that contain multiple oscillation frequencies with irrational ratio are observed in various systems [1–3, 12–15]. In coupled oscillators or forced oscillators that have two fundamental oscillation frequencies, we can observe infinitely many regions generating periodic oscillations, where two independent frequencies become rational, in parameter space. Such bifurcation structures are well-known as Arnol'd tongues [16, 21, 22, 24].

By contrast, higher-dimensional systems that have three- or higher oscillation frequencies have been studied extensively. In such higher dimensional quasi-periodic generating dynamics, much more complex entrainment structures emerge. For example, in three-dimensional tori-generating dynamics,

infinitely many regions generating two-dimensional tori, where two of three independent frequencies become irrational, are generated in region generating three-dimensional tori. Moreover, these two-dimensional tori generating regions overlap, and at the intersection, a periodic solution occurs. Such bifurcation structures are termed as "fractal devil's cobweb" in Ref [28]. In 1991, Baesens et. al. examined a family of torus maps, and introduced the concepts of *partial* and *full mode-locking* in [29]. The web-like bifurcation structures were called a "mode-locking web." In 2006, this "mode-locking web" were termed "Arnol'd resonance web" (ab. ARW) by Broer et. al. [30]. In addtition, periodic generating regions, which emerged at the intersections of two different two-dimensional tori, are called Chenciner bubbles.

ARW have generated intensive research interest in recent years in both discrete- and continuous-time dynamical systems [29, 35, 37, 53]. The analysis of ARW is usually performed by Lyapunov analysis, and has been rapidly progressing. Inaba et al. succeeded in observing ARW with high resolution in a driven electric circuit of two-coupled piecewise-constant oscillators (ab. PWCOs) [53]. PWCOs are simple continuous-time dynamics, of which the governing equation is represented by piecewise-constant dynamics [23, 24]. The Lyapunov exponents are obtained through a huge calculations in a resolution similar to those of discrete-time dynamical systems. However, Inaba et al. obtained the Lyapunov diagrams in an ad-hoc manner, and therefore, their

method appears to be difficult to apply to the Lyapunov analysis for higher dimensional piecewise-constant dynamics.

In this study, we investigate chaos and ARWs generated near the Chenciner bubbles from the same system as presented in [53]. The analysis is performed using explicit solutions in non-autonomous PWCOs, which is an extended algorithm discussed in [25]. By using this algorithm, two-parameter Lyapunov diagrams are systematically calculated. According to our numeric, chaos is observed in the neighborhood of Chenciner bubbles. Furthermore, we inevitably observe the hysteresis phenomenon, which distorts the Chenciner bubbles when the oscillators are weakly coupled. Moreover, we actually construct the driven piecewise-constant oscillators, and the numerical results are confirmed in circuit experiment.

4.2 Circuit model

Figure 4.2.1 shows a non-autonomous two-coupled circuit, which consists of two PWCOs and a rectangular wave current source $I_1(t)$. Each oscillator is connected by a capacitor. The voltages across three capacitors marked C_1, C_2, and C_3, are expressed as v_1, v_2 and v_3, respectively. $H_1(v_1)$ and $H_2(v_2)$ are hysteresis elements that are the same characteristics as those shown in Fig. 2.2.1(b). The governing equation of the non-autonomous two-coupled piece-constant circuit

is written by the following equations from Kirchhoff's law.

$$\begin{aligned}
\frac{C_1C_2+C_1C_3+C_2C_3}{C_3}\frac{\mathrm{d}v_1}{\mathrm{dt}} &= \frac{C_2+C_3}{C_3}H_1(v_1)+H_2(v_2)+I_1(t),\\
\frac{C_1C_2+C_1C_3+C_2C_3}{C_3}\frac{\mathrm{d}v_2}{\mathrm{dt}} &= \frac{C_1+C_3}{C_3}\Big(H_2(v_2)+I_1(t)\Big)+H_1(v_1).
\end{aligned} \tag{4.1}$$

By changing each variable and constant as in

$$\begin{aligned}
v_1 = V_{th1}x,\ v_2 = V_{th2}y,\ t=\gamma\tau,\\
h(x)I_{h1} = H_1(V_{th1}x),\ h(y)I_{h2} = H_2(V_{th2}y),\\
\frac{\gamma I_{h1}C_3}{V_{th1}(C_1C_2+C_1C_3+C_2C_3)} = 1,\\
\frac{I_{h2}}{I_{h1}} = D_1,\ \frac{V_{th1}}{V_{th2}} = D_2,\ \frac{I}{I_{h1}} = B,\\
\frac{C_2+C_3}{C_3} = D_3,\ \frac{C_1+C_3}{C_3} = D_4,\ \frac{T_0}{\gamma} = T,
\end{aligned} \tag{4.2}$$

the circuit dynamics is written by

$$\begin{aligned}
\dot{x} &= D_3h_1(x)+D_1h_2(y)+S(\tau),\\
\dot{y} &= D_2h_1(x)+D_2D_4\big(D_1h_2(y)+S(\tau)\big), \quad \left(\cdot = \frac{\mathrm{d}}{\mathrm{d}\tau}\right).
\end{aligned} \tag{4.3}$$

where $h_1(x)$ and $h_2(y)$ are the normalized hysteresis loops, of which characteristics are shown in Fig. 4.2.2(a) and Fig. 4.2.2(b), respectively. When x is on the upper branch, x increases in proportion to time. h switches from 1 to -1 if x reaches to the threshold $x=1$, and at instant, x jumps to the lower branch. Then, x decreases in proportion to time. h switches from -1 to 1 if x reaches to the threshold $x=-1$. The solution on the branch $h_2(y)$ behaves in the same manner.

The rectangular wave forcing $S(\tau)$ is expressed as follows:

$$S(\tau) = \begin{cases} B & \text{for } nT \leq \tau < (n+1)T, \\ -B & \text{for } (n+1)T \leq \tau < (n+2)T, \end{cases} (n = 0, 1, 2...), \tag{4.4}$$

where B and T is the amplitude and half-period of the rectangular wave force, respectively. The circuit dynamics include six parameters D_1, D_2, D_3, D_4, B, and T.

Throughout this study, we concentrate on the case where $-1 \leq x(\tau) \leq 1$ and $-1 \leq y(\tau) \leq 1$ hold for $\forall\tau$. In our assumption, the trajectory will hit boundary lines, i.e, $x = 1, x = -1, y = 1$, or $y = -1$.

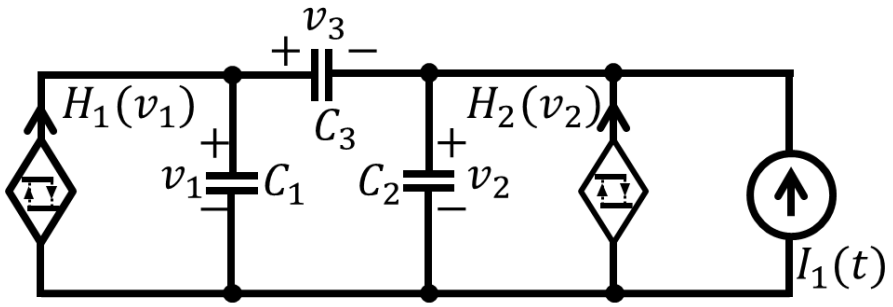

(a) Circuit model.

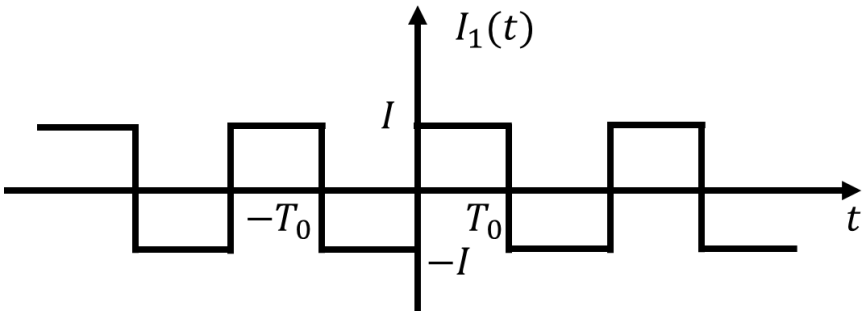

(b) Rectangular wave forcing.

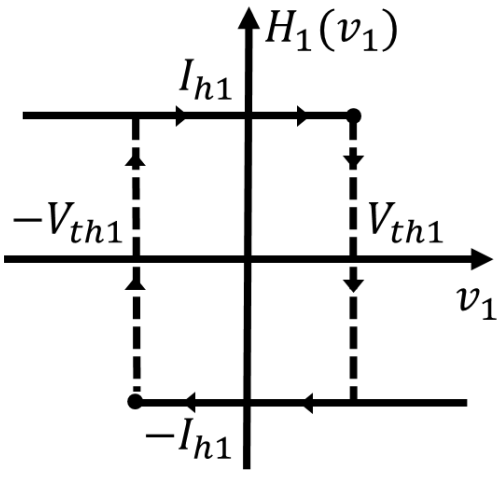

(c) $v - i$ characteristics of $H_1(v_1)$.

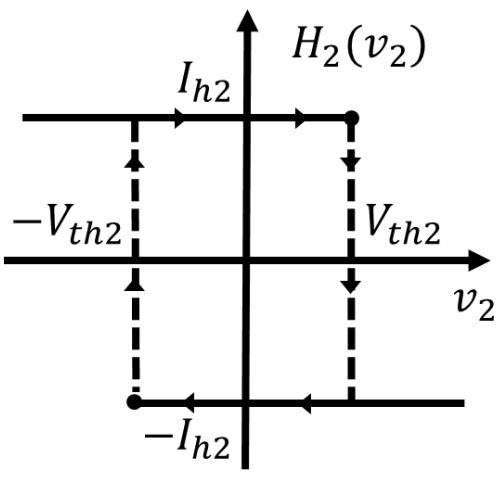

(d) $v - i$ characteristics of $H_2(v_2)$.

Figure 4.2.1 Circuit model of a two-coupled PWCOs driven by a rectangular wave forcing.

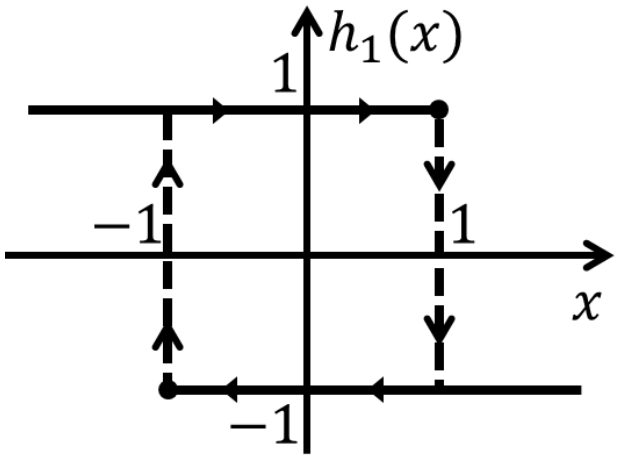

(a) $h_1(x)$.

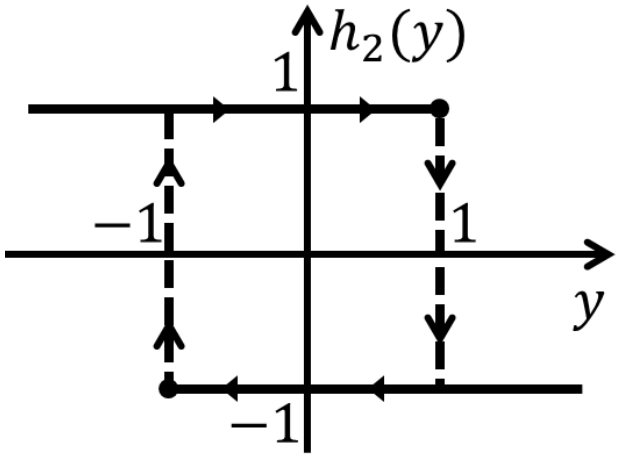

(b) $h_2(y)$.

Figure 4.2.2 Normalized hysteresis loops.

4.3 Oscillation behaviors

To facilitate the analysis of this system, we recast the governing equations into the autonomous form. By assuming τ as an independent variable, we can rewrite Eq. 4.3 as follows:

$$\begin{aligned} \dot{x} &= k_{xi} = D_3 h_1(x) + D_1 h_2(y) + S(z), \\ \dot{y} &= k_{yi} = D_2 h_1(x) + D_2 D_4\big(D_1 h_2(y) + S(z)\big), \\ \dot{z} &= k_{zi} = 1. \end{aligned} \tag{4.5}$$

Since $h_1(x)$ or $h_2(y)$ takes two values: -1 and 1, $\boldsymbol{k}(i) = (k_{xi}, k_{yi}, k_{zi})^\top$ takes constant values. The notation $^\top$ represents the transpose of the vector. Using these notations, the circuit dynamics are expressed as follows:

$$\dot{\boldsymbol{x}} = \boldsymbol{k}(i) \in D(i), \quad i \in \{0, 1, ..., 7\}, \tag{4.6}$$

where $\boldsymbol{x} = (x, y, z)^\top$, and i is an index for indicating the region $D(i)$. $\boldsymbol{k}(i)$ and region $D(i)$ are summarized in Table 4.1. For example, in the case of $i = 0$, since $h_1(x) = h_2(y) = 1$, $\boldsymbol{k}(0) = (k_{x0}, k_{y0}, k_{z0})^\top = \big(D_3 + D_1 + B, D_2 + D_2 D_4 (D_1 + B), 1\big)^\top$.

Figure 4.3.1 show the dynamics behavior on the phase space with a horizontal axis x and vertical axis y. The trajectory leaving $\boldsymbol{x}_0 = (x_0, y_0, z_0)^\top = (x_0, y_0, 0)^\top$, which is marked by the red solid circle on the boundary $x = -1$ of region $D(0)$, will reach the boundary $y = 1$. Since the state variable y reaches the threshold $y = 1$, $h_2(y)$ switches from 1 to -1. The trajectory tran-

Table 4.1 Values of $\boldsymbol{k}(i)$

i	$\boldsymbol{k}(i) = (k_{xi}, k_{yi}, k_{zi})^\top$	Regions $D(i)$
0	$\big(D_3 + D_1 + B, D_2 + D_2D_4(D_1 + B), 1\big)^\top$	$h_1(x) = 1,\ h_2(y) = 1,\ 0 \le z < T$
1	$\big(D_3 - D_1 + B, D_2 + D_2D_4(-D_1 + B), 1\big)^\top$	$h_1(x) = 1,\ h_2(y) = -1,\ 0 \le z < T$
2	$\big(-D_3 + D_1 + B, -D_2 + D_2D_4(D_1 + B), 1\big)^\top$	$h_1(x) = -1,\ h_2(y) = 1,\ 0 \le z < T$
3	$\big(-D_3 - D_1 + B, -D_2 + D_2D_4(-D_1 + B), 1\big)^\top$	$h_1(x) = -1,\ h_2(y) = -1,\ 0 \le z < T$
4	$\big(D_3 + D_1 - B, D_2 + D_2D_4(D_1 - B), 1\big)^\top$	$h_1(x) = 1,\ h_2(y) = 1,\ T \le z < 2T$
5	$\big(D_3 - D_1 - B, D_2 + D_2D_4(-D_1 - B), 1\big)^\top$	$h_1(x) = 1,\ h_2(y) = -1,\ T \le z < 2T$
6	$\big(-D_3 + D_1 - B, -D_2 + D_2D_4(D_1 - B), 1\big)^\top$	$h_1(x) = -1,\ h_2(y) = 1,\ T \le z < 2T$
7	$\big(-D_3 - D_1 - B, -D_2 + D_2D_4(-D_1 - B), 1\big)^\top$	$h_1(x) = -1,\ h_2(y) = -1,\ T \le z < 2T$

sitions from region $D(0)$ with $\boldsymbol{k}(0) = \big(D_3 + D_1 + B, D_2 + D_2D_4(D_1 + B), 1\big)^\top$ to region $D(1)$ with $\boldsymbol{k}(1) = \big(D_3 - D_1 + B, D_2 + D_2D_4(-D_1 + B), 1\big)^\top$. In such a case, x increases and y decreases. Thus, the trajectory reaches the boundary $x = 1$. At this instant, $h_1(x)$ switches from 1 to -1. The trajectory transitions from region $D(1)$ with $\boldsymbol{k}(1)$ to region $D(3)$ with $\boldsymbol{k}(3) = \big(-D_3 - D_1 + B, -D_2 + D_2D_4(-D_1 + B), 1\big)^\top$. It moves linearly to the boundary $y = -1$. Moreover, the trajectory is approaching to the next boundary, i.e., the rectangular wave forcing changes from B to $-B$ corresponding to $z = T$. Thus, the trajectory transitions from region $D(3)$ with $\boldsymbol{k}(3)$ to region $D(7)$ with $\boldsymbol{k}(7)$. Next, the trajectory will reach the boundary $y = -1$ of region $D(6)$ and $x = -1$ of region $D(4)$, respectively. Thus, the solution repeats again these behaviors.

Next, by changing D_2 and T, we discuss some patterns of the trajectory.

When $\tau = 0$, we set the initial values: $\big(x_0, y_0, z_0, h_1(x_0), h_2(y_0)\big) = (-0.4, 0.4, 0, 1, 1)$ with the information of the amplitude of the rectangular wave forcing is B. We draw the trajectory from $\tau = 100$ to $\tau = 100.1$. Our numerical results show that $\tau = 100$ is enough as a transient time. Figure (a) represents attractor on phase space $x - y$. In addition, Fig. (b)–(c) show time waveforms of the state variables x, and y, respectively. We fix the following parameter values: $D_2 = 1.1, D_3 = D_4 = 101$ and $B = 0.005$. The trajectory shows a periodic oscillation at $(D_1 = 0.911, T = 0.0199)$ as shown in Fig. 4.3.2. By contrast, a quasi-periodic oscillation is observed at $(D_1 = 0.911, T = 0.0199)$ as shown in Fig. 4.3.3.

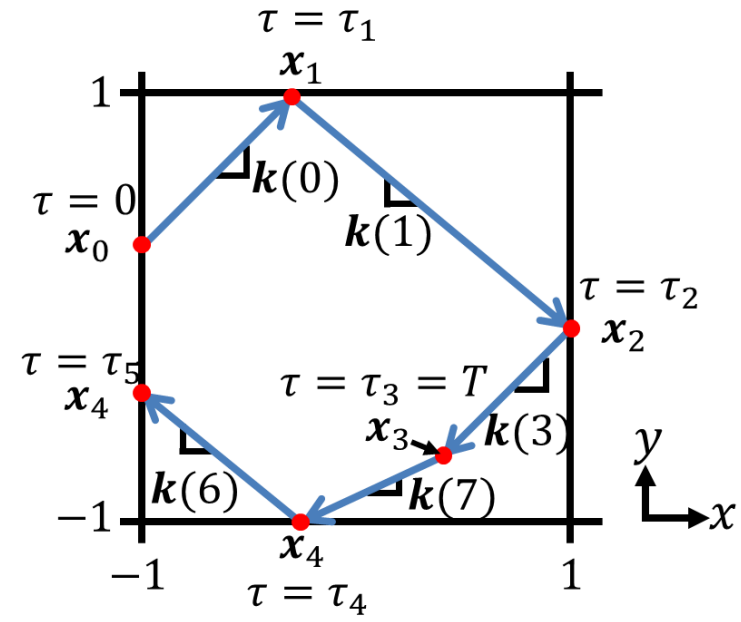

(a) Oscillation behaviors.

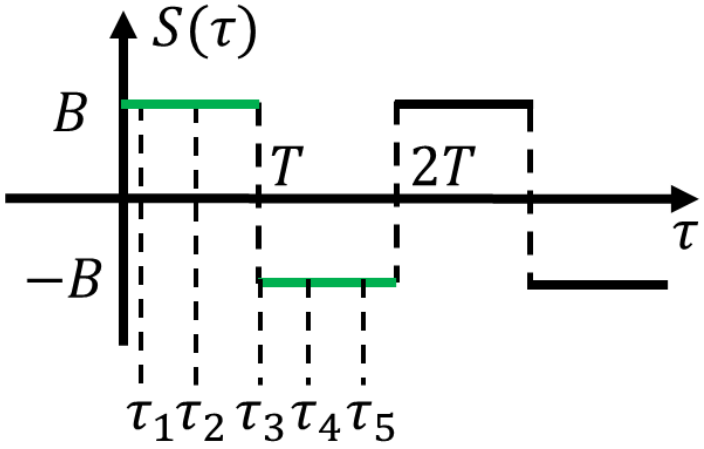

(b) Time corresponding to location of $\boldsymbol{x_i}$.

Figure 4.3.1 Example of oscillation behaviors.

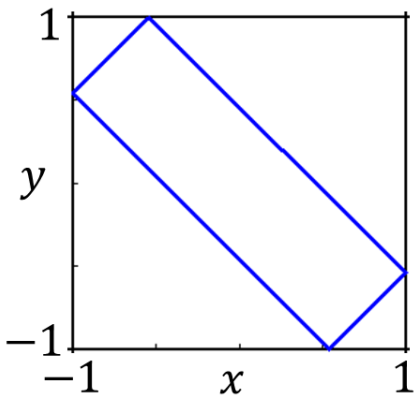

(a)

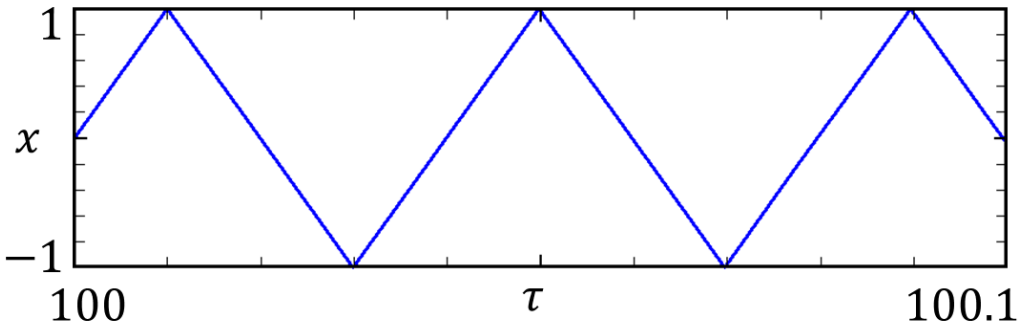

(b)

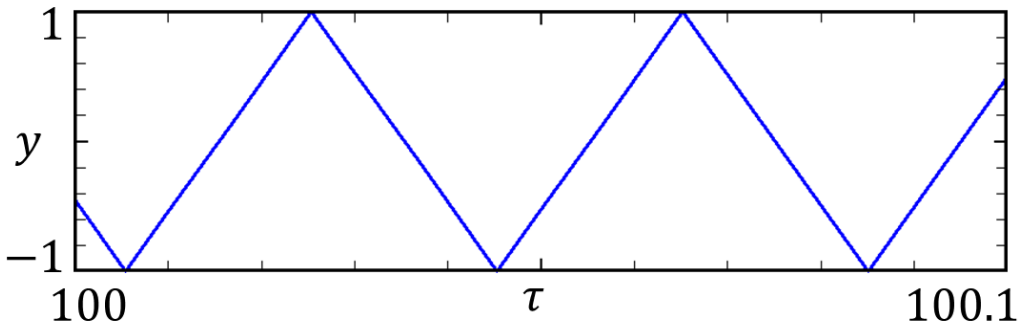

(c)

Figure 4.3.2 Periodic oscillation ($D_1 = 0.911, T = 0.0199$).

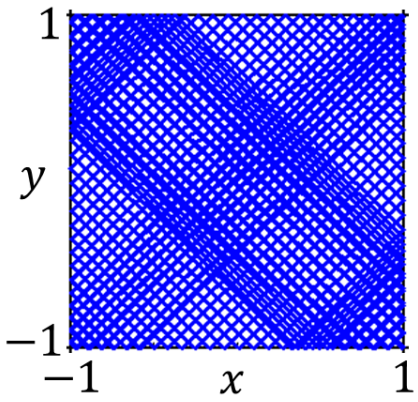

(a)

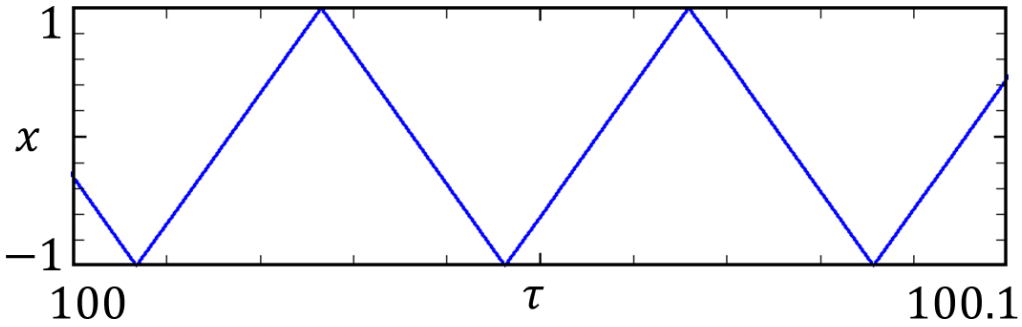

(b)

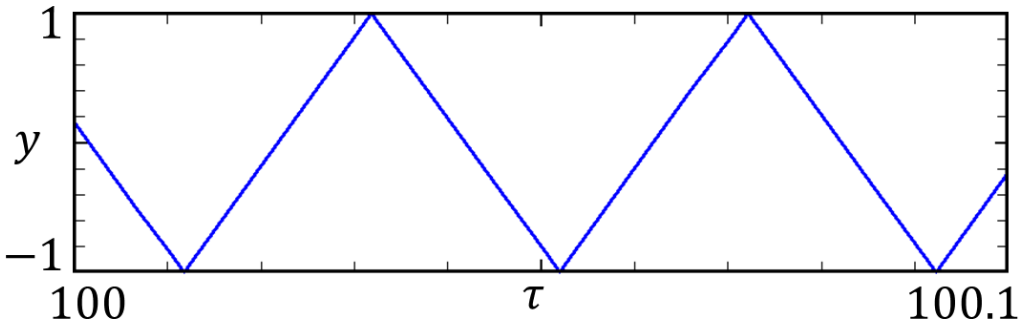

(c)

Figure 4.3.3 Quasi-periodic oscillation ($D_1 = 0.894, T = 0.0202$).

4.4 Calculation algorithm for deriving the rigorous solutions

Although a calculation algorithm for deriving of the explicit solutions have been proposed in Ref. [25], it is not sufficient for analysis of two- or higher-dimensional non-autonomous systems. In this section, we introduce a novel method [26], which can be applicable to both autonomous and non-autonomous systems. The calculation of the trajectories can be accomplished by the following 4 steps.

STEP 1

We provide the initial values $\big(x_0, y_0, z_0, h_1(x_0), h_2(y_0)\big)$ with the information of the amplitude of the rectangular wave forcing. We obtain the region containing the initial values by referring to the Table 4.1.

STEP 2

We calculate the time τ when the trajectory leaving $\boldsymbol{x}_0 = (x_0, y_0, z_0)^\top = (x_0, y_0, 0)^\top$ reaches $\boldsymbol{x}_1 = (x_1, y_1, z_1)^\top$ on the boundary, i.e., either one of $x = 1$, $x = -1$, $y = 1$, $y = -1$, $z = T$, or $z = 2T$. The state variable $\boldsymbol{x}_1$ is calculated by

$$\boldsymbol{x}_1 = \boldsymbol{x}_0 + \boldsymbol{k}(i) \cdot \tau, \tag{4.7}$$

where $\boldsymbol{k}(i)$ is obtained from Table 4.1. By introducing a normal vector $\boldsymbol{n}^\top$ for the boundary, the boundary condition can be expressed as follows:

$$\boldsymbol{n}^\top \cdot \boldsymbol{x}_1 = P, \tag{4.8}$$

where P is a constant value; $\boldsymbol{n}^\top$ and P are listed in Table 4.2. For example, if the trajectory arrives at $y = 1$ with the normal vector $\boldsymbol{n}^\top = (0\ 1\ 0)$ at $\boldsymbol{x}_1 = (x_1, y_1, z_1)^\top = (x_1, 1, z_1)^\top$, the scalar P is $P = 1$.

Substituting Eq. 4.7 into Eq. 4.8 yields

$$\tau = \frac{P - \boldsymbol{n}^\top \cdot \boldsymbol{x}_0}{\boldsymbol{n}^\top \cdot \boldsymbol{k}(i)}. \tag{4.9}$$

For example, we calculate the time when the trajectory leaving $\boldsymbol{x}_0$ on the boundary $x = -1$ corresponding to region $D(0)$ strikes the either boundary of $y = 1$ or $x = 1$ corresponding region $D(1)$ or $D(2)$, respectively.

If the trajectory hits $y = 1$, the time τ_0 is manually calculated as

$$\tau_0 = \frac{P - \boldsymbol{n}^\top \cdot \boldsymbol{x}_0}{\boldsymbol{n}^\top \cdot \boldsymbol{k}(0)}, \tag{4.10}$$

where $\boldsymbol{n}^\top = (0\ 1\ 0)$ and $P = 1$.

If the trajectory reaches $x = 1$, the time τ_1 is also calculated as

$$\tau_1 = \frac{P - \boldsymbol{n}^\top \cdot \boldsymbol{x}_0}{\boldsymbol{n}^\top \cdot \boldsymbol{k}(0)}, \tag{4.11}$$

where $\boldsymbol{n}^\top = (1\ 0\ 0)$ and $P = 1$.

Assume that the time when the trajectory strikes the closest boundary is τ_{cl}. τ_{cl} is the minimum positive time between τ_0 and τ_1. And it is defined by

$$\tau_{cl} = \min\{\tau_k\} \quad \text{for} \quad \tau_k > 0 \quad (k = 0, 1). \tag{4.12}$$

Next, we determine the time τ_{sw} when the rectangular wave forcing switches.

$$\tau_{sw} = \frac{T}{2} - (\tau_{cl} \bmod \frac{T}{2}). \tag{4.13}$$

By comparing τ_{cl} and τ_{sw}, the minimum positive time is the actual switching time τ. Noting that as the rectangular wave forcing resets, the amplitude changes from B to $-B$ or vice versa.

STEP 3

By substituting τ to Eq. 4.7, $\boldsymbol{x}_1$ is explicitly calculated. Depending on the region $D(i)$ containing $\boldsymbol{x}_1$, $\boldsymbol{k}(i)$ is also obtained.

STEP 4

We substitute $\boldsymbol{x}_1$ into $\boldsymbol{x}_0$ and go to **STEP 2**.

Table 4.2 Boundary conditions

	$\boldsymbol{n}^\top$	P
$x = 1$	(1 0 0)	1
$x = -1$	(1 0 0)	-1
$y = 1$	(0 1 0)	1
$y = -1$	(0 1 0)	-1
$z = T$	(0 0 1)	T
$z = 2T$	(0 0 1)	$2T$

4.5 Lyapunov analysis

In this section, we conduct Lyapunov analysis to determine the solutions as periodic, quasi-periodic, or chaotic by using the calculation algorithm, which is

presented in Section 4.4. The Lyapunov exponents or the Lyapunov characteristic exponents of a dynamical system expresses the rate how the solutions that are located in close proximity expand or converge. Computational algorithms for calculating the Lyapunov exponents were presented by Shimada and Nagashima [63]. In general, n-dimensional autonomous ODEs have n Lyapunov exponents. Let the first, second – and n-th Lyapunov exponents be denoted by λ_1, λ_2, $\cdots$, λ_n, respectively ($\lambda_1 \geq \lambda_2 \geq \cdots \geq \lambda_n$).

- The solution is periodic if $\lambda_1 < 0$.
- The solution is two-dimensinal tori if $\lambda_1 = 0$ and $\lambda_2 < 0$.
- The solution is three-dimensinal tori if $\lambda_1 = \lambda_2 = 0$ and $\lambda_3 < 0$.
- The solution is n-dimensinal tori if $\lambda_1 = \lambda_2 = ... = \lambda_{n-1} = 0$ and $\lambda_n < 0$.
- The solution is chaotic if $\lambda_1 > 0$.

Based on the procedure for calculating the Lyapunov exponents in Ref. [63], the first and the second Lyapunov exponent are defined as follows:

$$\begin{aligned} \lambda_1 &\simeq \frac{1}{N} \sum_{j=M+1}^{M+N} \ln \left| A_i^j e_1^j \right|, \\ \lambda_1 + \lambda_2 &\simeq \frac{1}{N} \sum_{j=M+1}^{M+N} \ln \left| A_i^j e_1^j \times A_i^j e_2^j \right|, \end{aligned} \tag{4.14}$$

where e_1^j and e_2^j are orthonormal bases, and A_i^j is the Jacobian matrix. M and N are positive integers.

The numerical methods for calculating the Lyapunov exponents in driven system of two-coupled PWCOs have been reported in Ref [53]. At first, to obtain the Jacobian matrix, some sections are defined as follows:

$$\begin{aligned} \pi_z^0 &= \{\boldsymbol{x}|z=0\}, \\ \pi_z^T &= \{\boldsymbol{x}|z=T\}. \end{aligned} \tag{4.15}$$

The Jacobian matrix is defined as

$$A_i = \begin{pmatrix} \dfrac{\partial x(2nT)}{\partial x(0)} & \dfrac{\partial x(2nT)}{\partial y(0)} \\ \dfrac{\partial y(2nT)}{\partial x(0)} & \dfrac{\partial y(2nT)}{\partial y(0)} \end{pmatrix}. \tag{4.16}$$

We consider the trajectory leaving from $\boldsymbol{x}_0 = (x_0, y_0)^\top$ with $\boldsymbol{k}(0) = (k_{x0}, k_{y0})^\top$ at $\tau = 0$ and arriving at $\boldsymbol{x}_4 = (x_4, y_4)^\top$ at $\tau = 2T$ via $\boldsymbol{x}_1 = (x_1, y_1)^\top$ with $\boldsymbol{k}(2) = (k_{x2}, k_{y2})^\top$, $\boldsymbol{x}_2 = (x_2, y_2)^\top$ with $\boldsymbol{k}(6) = (k_{x6}, k_{y6})^\top$ and $\boldsymbol{x}_3 = (x_3, y_3)^\top$ with $\boldsymbol{k}(7) = (k_{x7}, k_{y7})^\top$ as shown in Fig 4.5.1. Let τ_1 be denoted the time at $\boldsymbol{x}_1 = (x_1, y_1)^\top$ on the boundary $x = 1$. We obtain the following equation:

$$\begin{aligned} x_1 &= k_{x0}\tau_1 + x_0 = 1, \\ y_1 &= k_{y0}\tau_1 + y_0. \end{aligned} \tag{4.17}$$

Therefore, τ_1 and y_1 can be calculated as

$$\begin{aligned} \tau_1 &= \frac{(1-x_0)}{k_{x0}}, \\ y_1 &= -\frac{k_{y0}}{k_{x0}}x_0 + y_0 + \frac{k_{y0}}{k_{x0}}. \end{aligned} \tag{4.18}$$

When the solution is on the section π_z^0 corresponding to $\tau_2 = T$, we similarly obtain $\boldsymbol{x}_2 = (x_2, y_2)^\top$ as follows:

$$\begin{aligned} x_2 &= k_{x2}(T - \tau_1) + 1, \\ y_2 &= k_{y2}(T - \tau_1) + y_1. \end{aligned} \tag{4.19}$$

Therefore,

$$A_1 = \begin{pmatrix} \dfrac{\partial x_2}{\partial x_0} & \dfrac{\partial x_2}{\partial y_0} \\ \dfrac{\partial y_2}{\partial x_0} & \dfrac{\partial y_2}{\partial y_0} \end{pmatrix} = \begin{pmatrix} \dfrac{k_{x2}}{k_{x0}} & 0 \\ \dfrac{-k_{y0}+k_{y2}}{k_{x0}} & 1 \end{pmatrix}. \tag{4.20}$$

Similarly, when the solution is on the section π_z^T, the Jacobian matrix is obtained as follows:

$$A_2 = \begin{pmatrix} \dfrac{\partial x_4}{\partial x_2} & \dfrac{\partial x_4}{\partial y_2} \\ \dfrac{\partial y_4}{\partial x_2} & \dfrac{\partial y_4}{\partial y_2} \end{pmatrix} = \begin{pmatrix} 1 & \dfrac{k_{x7}-k_{x6}}{k_{y6}} \\ 0 & \dfrac{k_{y7}}{k_{y6}} \end{pmatrix}. \tag{4.21}$$

Therefore, the desired Jacobian matrix is expressed as

$$A_2 A_1 = \begin{pmatrix} \dfrac{\partial x_4}{\partial x_0} & \dfrac{\partial x_4}{\partial y_0} \\ \dfrac{\partial y_4}{\partial x_0} & \dfrac{\partial y_4}{\partial y_0} \end{pmatrix}. \tag{4.22}$$

If we use the above procedure, we must pay attention to the time when the rectangular wave forcing resets. Thus, bothersome treatment is required for each step. Moreover, it could be difficult to apply this procedure to higher-dimensional PWCOs.

To overcome these problems, we now conduct Lyapunov exponent by using the local Jacobian matrices. Substituting Eq. 4.9 to Eq. 4.7 yields the following equation:

$$\boldsymbol{x}_1 = \left(I_n - \frac{\boldsymbol{k}(i)\boldsymbol{n}^\top}{\boldsymbol{n}^\top \boldsymbol{k}(i)} \right) \boldsymbol{x}_0 + \frac{\boldsymbol{k}(i)P}{\boldsymbol{n}^\top \boldsymbol{k}(i)}, \tag{4.23}$$

It is clear from Eq. 4.23 that the local Jacobian matrix is represented by

$$A = \frac{\mathrm{d}\boldsymbol{x}_1}{\mathrm{d}\boldsymbol{x}_0} = I_n - \frac{\boldsymbol{k}(i)\boldsymbol{n}^\top}{\boldsymbol{n}^\top \boldsymbol{k}(i)}. \tag{4.24}$$

Then, if the solution strikes $x = 1$ or $x = -1$,

$$A_0 = \begin{pmatrix} 0 & 0 & 0 \\ -k_{yi}/k_{xi} & 1 & 0 \\ -1/k_{xi} & 0 & 1 \end{pmatrix}, \tag{4.25}$$

if the solution strikes $y = 1$ or $y = -1$,

$$A_1 = \begin{pmatrix} 1 & -k_{xi}/k_{yi} & 0 \\ 0 & 0 & 0 \\ 0 & -1/k_{yi} & 1 \end{pmatrix}, \tag{4.26}$$

and if the solution strikes $z = T$ or $z = 2T$,

$$A_2 = \begin{pmatrix} 1 & 0 & -k_{xi} \\ 0 & 1 & -k_{yi} \\ 0 & 0 & 0 \end{pmatrix}. \tag{4.27}$$

Because the piecewise-constant equation is simple, calculations with large integers are possible. Such as $M = N = 2 \times 10^7$ is conductable. In this study, the Lyapunov exponent can be regarded to be exact zero if the calculated Lyapunov exponent satisfies the following condition:

$$|\lambda_i| < 1/10^6. \tag{4.28}$$

The first and the second Lyapunov exponent are used to illustrate a two-parameter Lyapunov diagram as shown in Fig. 4.5.2. We fix the coupling parameters $C_3/C_1 = C_3/C_2 = 0.01$ that correspond to $D_3 = D_4 = 101$. In addition, we set the parameters $D_2 = 1.1$, $B = 0.005$. Let D_1 and $2T$ be the bifurcation parameters, which lie on the horizontal and vertical axis, respectively.

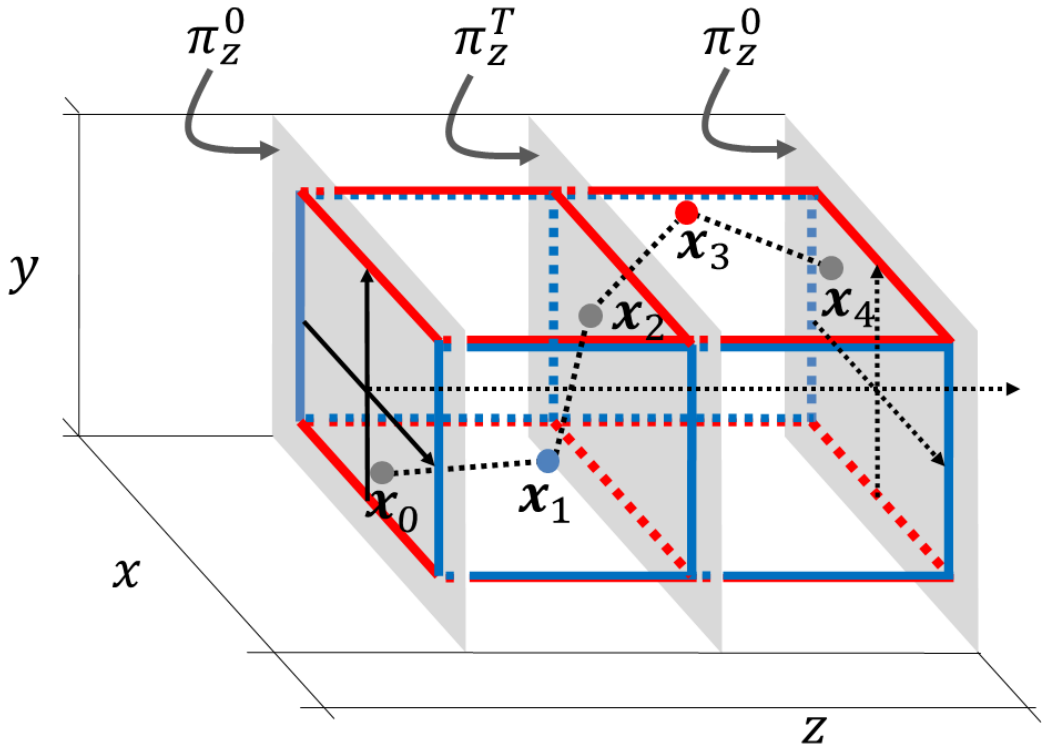

Figure 4.5.1 Schematic diagram of oscillation behaviors.

A continuous deformation method is used when the bifurcation parameters are varied. Parameter D_1 is varied from D_{1_present} to D_{1_next} as tracing parameter from left-hand side to right-hand side ($D_{1\_\text{present}} < D_{1\_\text{next}}$). The relationship between D_{1_present} and D_{1_next} is described by

$$D_{1\_\text{next}} = D_{1\_\text{present}} + \Delta D_1, \tag{4.29}$$

where ΔD_1 is chosen to be small ($0 < \Delta D_1 < 1$).

The final values $\big(x_1, y_1, z_1, h_1(x_1), h_2(y_1)\big)$ at D_{1_present} are substituted into the initial values $\big(x_0, y_0, z_0, h_1(x_0), h_2(y_0)\big)$ at D_{1_next}. Subsequently, let D_{1_present} be replaced by D_{1_next}. This procedure is repeated until D_1 reaches the final

values at $D_1 = 0.925$. Parameter value $2T$ is traced in the same procedure as that of D_1.

In Fig. 4.5.2(a) and (b), the regions generating periodic solution ($\lambda_1 < 0$) are marked by gray where the ratio of the two oscillations and the external force is $1 : 1 : 1$. This region is called Chenciner bubbles. The regions generating two-dimensional tori ($\lambda_1 = 0, \lambda_2 < 0$) and three-dimensional tori ($\lambda_1 = 0, \lambda_2 = 0$) are marked by blue and yellow, respectively. The regions generating chaos are marked by black. As seen in these figures, infinitely many of regions generating two-dimensional tori, which exist in regions generating three-dimensional tori, extend in numerous directions. It is clear from the figure that a Arnol'd resonance web is observed. Moreover, chaos is inevitably observed in close to the Chenciner bubbles.

In these figures, the red arrows show the direction of tracing parameter. We set the same initial values, i.e. $(x_0, y_0, h_1(x_0), h_2(y_0))$ for initial parameter values. For example, in Fig. 4.5.2(a), we choose the initial values at the bottom left and set initial parameter values by varying D_1 from the bottom left to the bottom right. We trace the parameter $2T$ from the bottom to the top. In contrast, in Fig. 4.5.2(b) we trace $2T$ from the top to the bottom with the same manner indicated in Fig. 4.5.2(a). According to the results, the bifurcation structures depend on the initial parameter values. Periodic solution and two-dimensional tori coexist in the phase space for different initial values, although

we set up the same values of parameters. The coexistence of these solutions gives rise to a hysteresis phenomenon [10, 14].

We can observe that the hysteresis erodes the Chenciner bubbles as shown in Fig. 4.5.2. Figures 4.5.3 show the two-parameter Lyapunov diagram with $B = 0.015$ and $D_3 = D_4 = 1001$. The Chenciner bubbles-generating region becomes more narrow as B decreases. This results suggest that the Chenciner bubbles do not necessarily occur due to the simple phase-locking of two-dimensional tori.

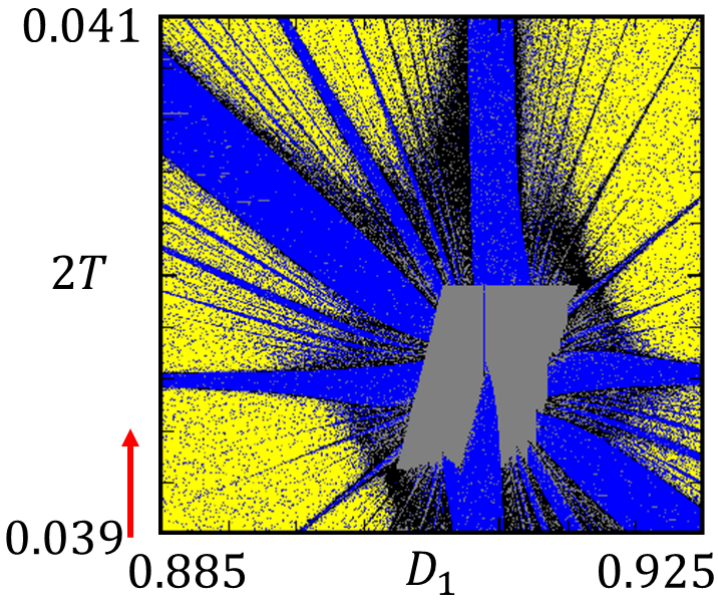

(a) Bottom left.

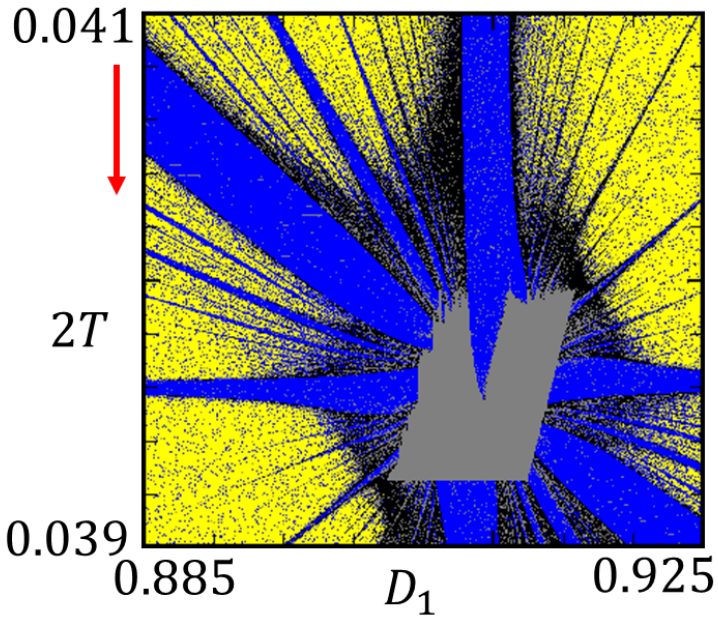

(b) Top left.

Figure 4.5.2 Two-parameter Lyapunov diagram obtained at initial parameter values: $D_2 = 1.1, D_3 = D_4 = 101$, and $B = 0.005$.

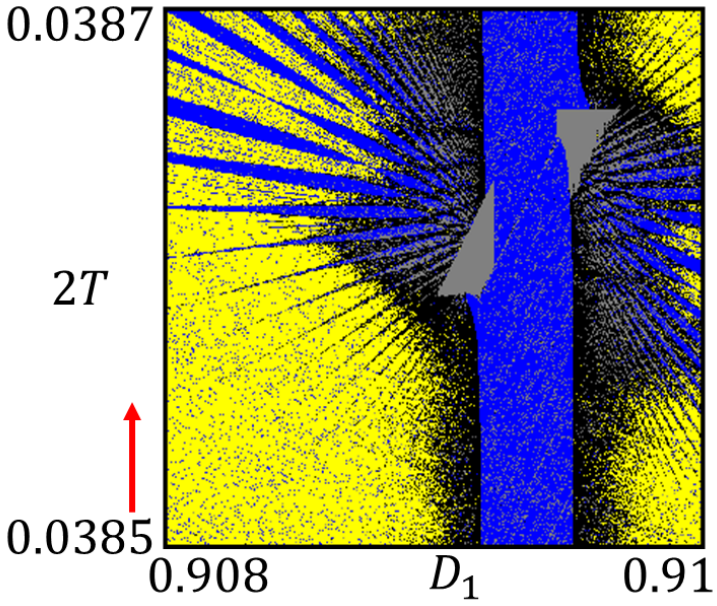

(a) Bottom left.

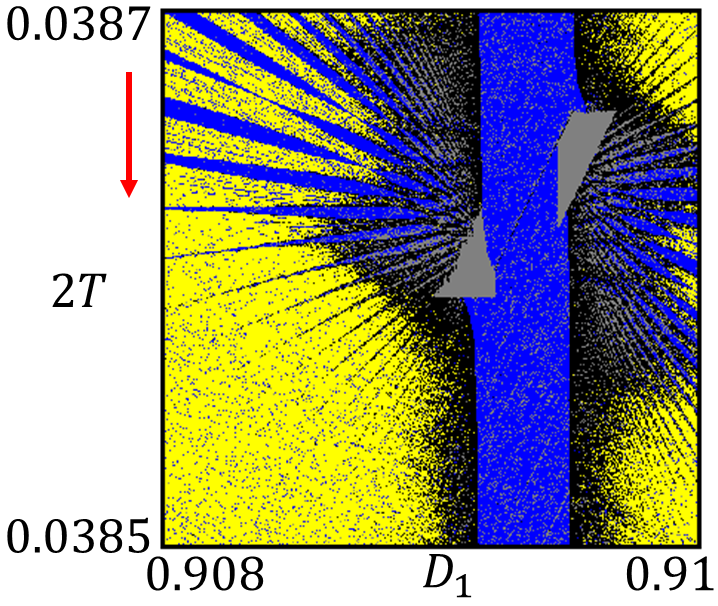

(b) Top left.

Figure 4.5.3 Two-parameter Lyapunov diagram obtained at initial parameter values: $D_2 = 1.1, D_3 = D_4 = 1001$, and $B = 0.015$.

To confirm the coexistence of the periodic solution and two-dimensional tori, we fix all parameter values: $D_1 = 0.906, D_2 = 1.1, D_3 = D_4 = 101, B = 0.005, 2T = 0.0398$. By changing initial values, we can observe different solutions as shown in Fig. 4.5.4. By using the initial values $\big(x_0, y_0, h_1(x), h_2(y)\big) = (0.25, -0.9, 1, 1)$, the periodic solution projecting onto the $x - y$ plane is shown in Fig. 5.5.3(a). And the corresponding point obtained on the section π_z^0 is shown in Fig. 4.5.4(b). By contrast, we use the slightly different initial values $\big(x_0, y_0, h_1(x), h_2(y)\big) = (0.9, -0.9, 1, 1)$, the two-dimensional tori is shown in Fig. 4.5.4(c). And the corresponding attractor obtained on the section π_z^0 is shown in Fig. 4.5.4(d).

Next, it is necessary to clarify the boundaries between the initial values obtaining the periodic solution and two-dimensional tori. We calculate the basins of the attractors as shown in Fig. 4.5.5. Let us consider a flow that leaves a point on the section π_z^0 with $h_1(x) = h_2(y) = 1$. Since we restrict our attention to the case when $-1 \leq x, y \leq 1$, x and y vary in a range of $[-1, 1]$. Let x and y be located on the horizontal and vertical axis, respectively. If the flow is a periodic solution, i.e. $\lambda_1 < 0$, we plot the gray point. If the flow is a two-dimensional tori, i.e. $\lambda_1 = 0, \lambda_2 < 0$, we plot the blue point. In the situation of Fig. 4.5.5, which of the periodic solution or two-dimensional tori is observed depends on the region which the intial values is located.

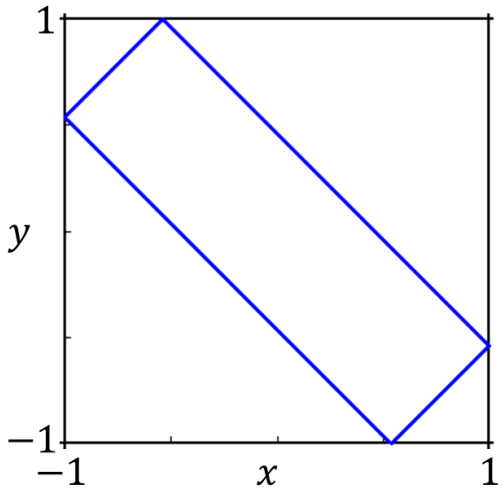

(a) Periodic oscillation with initial values: $\big(x_0, y_0, h_1(x), h_2(y)\big) = (0.25, -0.9, 1, 1)$.

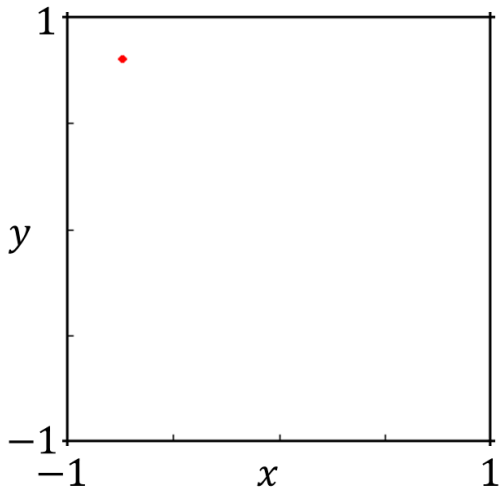

(b) Corresponding attractor on the section π_z^0 with initial values: $\big(x_0, y_0, h_1(x), h_2(y)\big) = (0.25, -0.9, 1, 1)$.

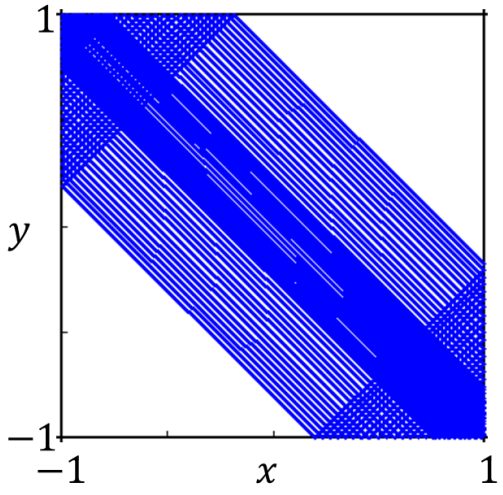

(c) Two-dimensional tori with initial values: $\big(x_0, y_0, h_1(x), h_2(y)\big) = (0.9, -0.9, 1, 1)$.

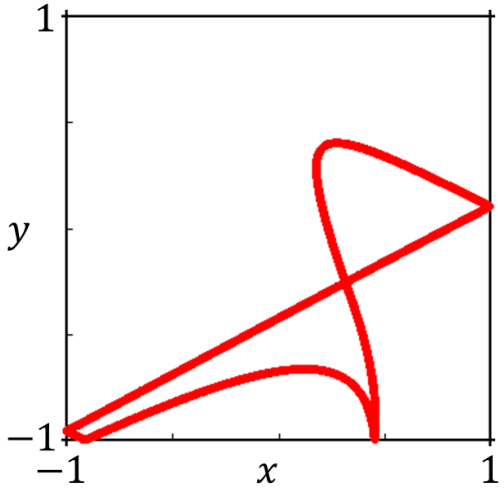

(d) Corresponding attractor on the section π_z^0 with initial values: $\big(x_0, y_0, h_1(x), h_2(y)\big) = (0.9, -0.9, 1, 1)$.

Figure 4.5.4 The coexistence of the periodic solution and two-dimensional tori ($D_1 = 0.906, D_2 = 1.1, D_3 = D_4 = 101, B = 0.005, 2T = 0.0398$).

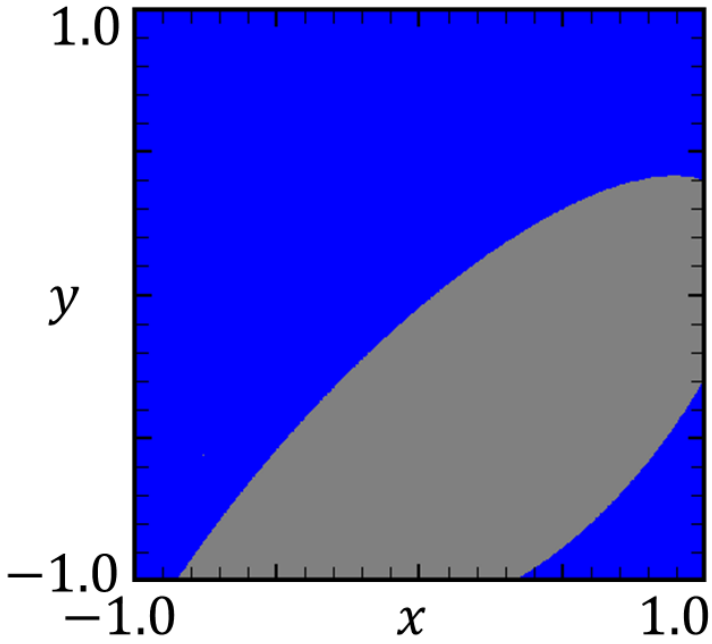

Figure 4.5.5 Basins of the periodic solution and two-dimensional tori ($D_1 = 0.906, D_2 = 1.1, D_3 = D_4 = 101, B = 0.005$, and $2T = 0.0398$).

4.6 Farey sequences

The Farey sequence is found to be related to the generation patterns of the two-dimensional tori. Numerical observation of this series that generated in two-coupled driven PWCOs, have been proposed in Ref [53]. However, the Farey sequence was not observed in laboratory measurements. In this section, we observe Farey sequence both numerically and experimentally.

The Farey sequence is a ascending sequence of irreducible fractions between 0 and 1. For example, we give the following Farey sequence:

$$F = \left\{ \frac{0}{1}, \frac{1}{4}, \frac{1}{3}, \frac{2}{5}, \frac{1}{2} \right\}. \tag{4.30}$$

If $\frac{a}{b}, \frac{c}{d}$, and $\frac{e}{f}$ are consecutive fractions in a Farey sequence then

$$\frac{c}{d} = \frac{a+e}{b+f}. \tag{4.31}$$

The main reason that Farey sequence was not observed in laboratory measurement, was that the coupling parameter value is very small, i.e., $\frac{C_3}{C_1} = \frac{C_3}{C_2} = 0.01$ corresponding to $D_3 = D_4 = 101$. In such cases, the regions generating two-dimensional tori are narrow. To confirm numerical and experimental observation of the Farey sequence, we conduct a two-parameter Lyapunov diagram with parameter values: $D_3 = D_4 = 11$ as shown in Fig. 4.7.1.

Figure 4.7.2 shows various types of two-dimensional tori on the section π_z^0 projected on the $x-y$ plane. Figures (a)–(e) correspond to the parameter values marked by R_1–R_5 in Fig. 4.7.1. The number of times the two-dimensional tori

reaches the boundary $x = -1$ is denoted by H. The number of times the two-dimensional tori reaches the boundary $y = -1$ is denoted by K. In Fig 4.7.2, since $H = 1$ and $K = 0$, we can obtain the fraction $\frac{K}{H} = \frac{0}{1}$. In the same way, we can obtain the series $\left\{\frac{0}{1}, \frac{1}{4}, \frac{1}{3}, \frac{2}{5}, \frac{1}{2}\right\}$. Between R_1 and R_5, there exists R_3, i.e., $\frac{1}{3} = \frac{0+1}{1+2}$. Similarly, between R_1 and R_3, there exists R_2, i.e., $\frac{1}{4} = \frac{0+1}{1+3}$. In the same vein, R_4 exist between R_3 and R_5, and R_3 exists between R_2 and R_4. Figures 4.7.3(b), (d), and (f) show the associated experimental observation of Farey sequence corresponding to points R_1, R_3, R_5 in Fig. 4.7.1. Remarkable agreement can be confirmed.

4.7 Conclusions

We analyzed chaos and quasi-periodic phenomena generated in a non-autonomous two-coupled PWCOs. We formulated the numerical procedure for conducting the Lyapunov analysis in PWCOs. This procedure is applicable in both autonomous and non-autonomous PWCOs driven by a rectangular wave forcing. The extremely simple procedure will contribute to the study on bifurcation analysis of the family of PWCOs. Two-parameter Lyapunov diagrams were obtained, which show the complex bifurcation structures. According to the numerical results, chaos occurred around the regions generating the Chenciner bubbles. Inevitably, we observed the hysteresis phenomenon, which distorts the Chenciner bubbles in the cases of weak coupling. Furthermore, the generation

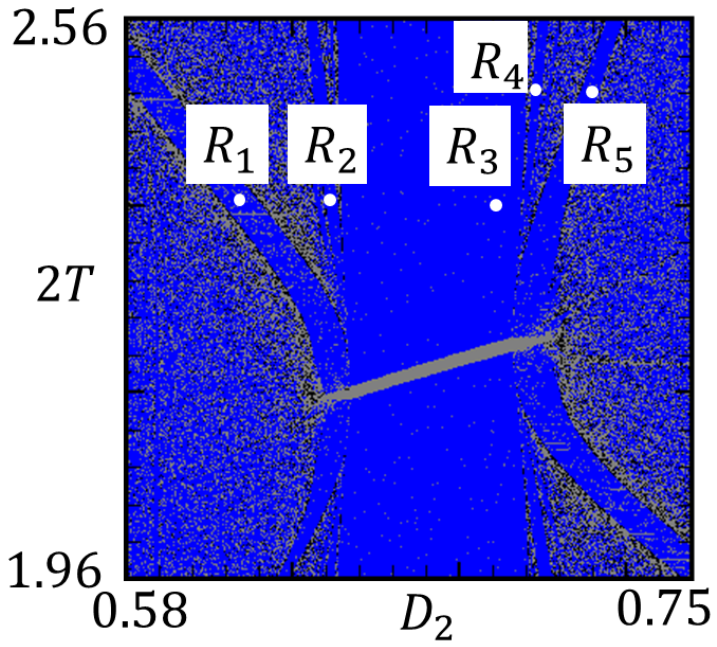

Figure 4.7.1 Two-parameter Lyapunov diagram ($D_1 = 0.5, D_3 = D_4 = 11$, and $B = 0.005$).

pattern of two-dimensional tori was demonstrated numerically and experimentally. In future work, we plan to clarify the bifurcation mechanism causing the hysteresis phenomenon.

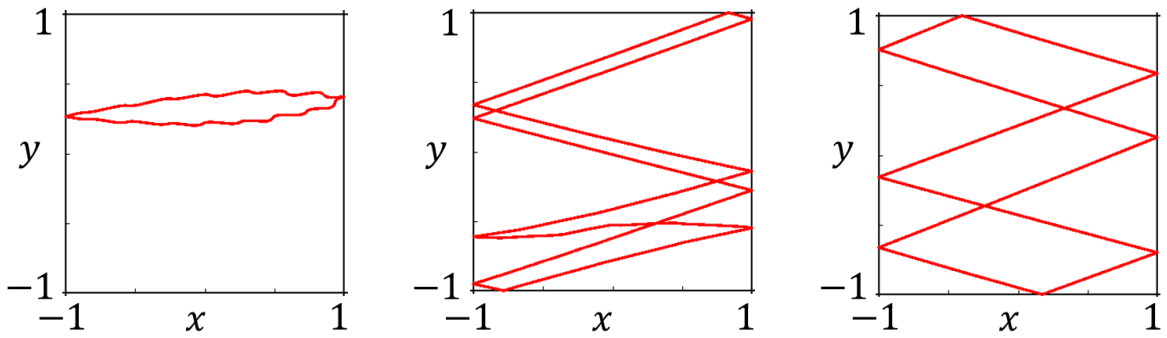

(a) $R_1(0:1)$.

(b) $R_2(1:4)$.

(c) $R_3(1:3)$.

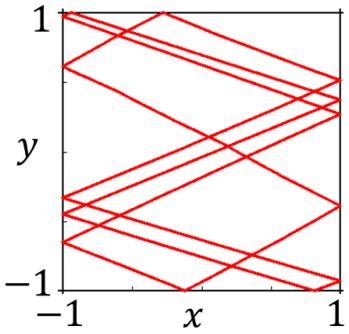

(d) $R_4(2:5)$.

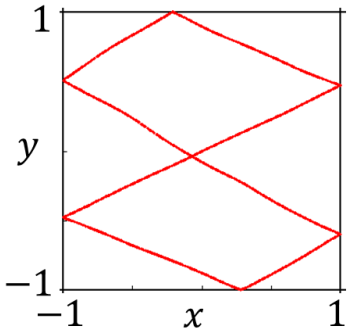

(e) $R_5(1:2)$.

Figure 4.7.2 Farey sequences ($D_1 = 0.5, D_3 = D_4 = 11$, and $B = 0.005$): (a) $D_2 = 0.61$, $T = 1.188$; (b) $D_2 = 0.64135$, $T = 1.188$; (c) $D_2 = 0.68$, $T = 1.188$; (d) $D_2 = 0.70199$, $T = 1.2298$; (e) $D_2 = 0.7166$, $T = 1.2298$.

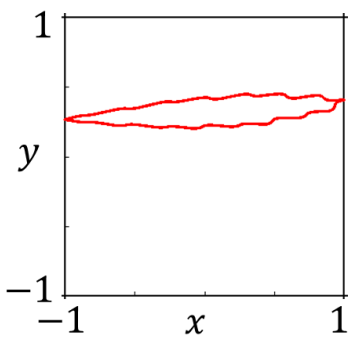

(a) $(D_2, T) = (0.61, 1.188)$.

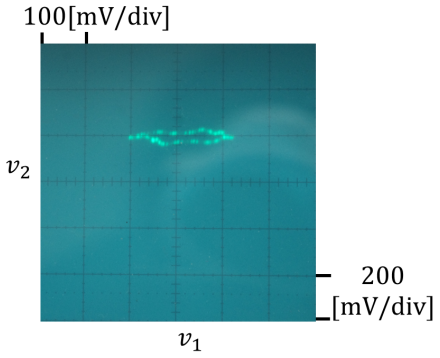

(b) $v_{th2} = 655.7[\mathrm{mV}], 2T_0 = 0.207[ms]$.

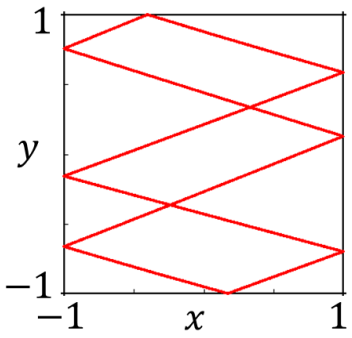

(c) $(D_2, T) = (0.64135, 1.188)$.

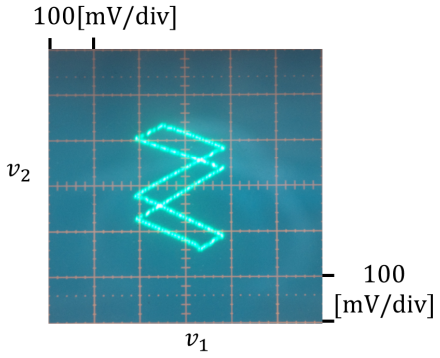

(d) $v_{th2} = 597[\mathrm{mV}], 2T_0 = 0.207[ms]$.

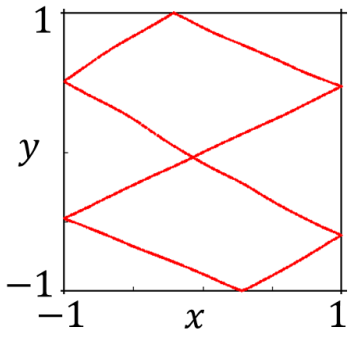

(e) $(D_2, T) = (0.7166, 1.2298)$.

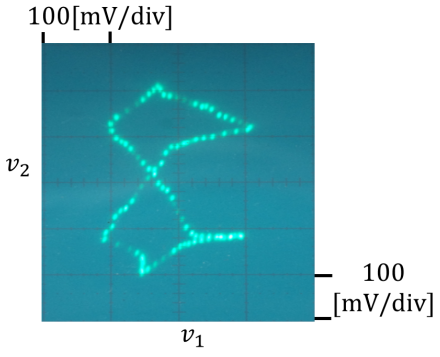

(f) $v_{th2} = 560[\mathrm{mV}], 2T_0 = 0.214[ms]$.

Figure 4.7.3 Experimental observation of Farey sequences.

Chapter 5

Arnol'd Resonance Web and Chenciner Bubbles Generated in Three-coupled Piecewise-Constant Oscillators

5.1 Introduction

Quasi-periodic bifurcations have a subject of intensive research interest in recent years [1–3, 12–15]. In coupled oscillators or forced oscillators that have two fundamental oscillation frequencies, a quasi-periodic oscillation is observed if the rotation number that represents the ratio between the two frequencies is irrational. Such quasi-periodic oscillation is called two-dimensional tori. In two-dimensional tori-generating dynamics, it is known that there exist infinitely many periodic solution-generating regions, where the ratio becomes rational. Such regions are well known as Arnol'd tongues and have been studied for several decades [16, 21, 22, 24].

However, in three- or higher dimensional tori-generating dynamics have revealed the existence of significantly more complex bifurcation structures. In

these dynamics, infinitely many regions generating two-dimensional tori exist in region generating three-dimensional tori wherein they extend in numerous directions like a "cobweb" in parameter space. Such bifurcation structures are termed "fractal devil's cobweb" in Ref [28]. In 1991, Baesens et. al. examined a family of torus maps, and introduced the concepts of *partial* and *full mode-locking* [29]. They called the web-like bifurcation structure "mode-locking web." In 2006, this "mode-locking web" were finally termed "Arnol'd resonance web" (ab. ARW) by Broer et. al. [30]. In addtition, periodic generating regions, which emerged at the intersections of two different two-dimensional tori, are called Chenciner bubbles.

ARW have attracted intensive research interest in recent years in both discrete- and continuous-time dynamical systems [29, 35, 37, 53]. The study of ARW is usually performed by Lyapunov analysis, and has been rapidly progressings. However, the main concerns for observing ARW in continuous-time dynamics are the precision and computational cost. By using a computational cost similar to that of discrete-time dynamics, Inaba et al. succeeded in observing ARW with high resolution in a driven continuous-time electric circuit of two-coupled piecewise-constant oscillators (ab. PWCOs) [53]. Afterward, we analyzed this circuit in detail by using a systematic procedure, which can be applicable to a wide class of PWCOs. Our numerical results showed that a hysteresis phenomenon occurs near the Chenciner bubbles. Although this phenomenon is

evident, we could not fully clarify the bifurcation mechanism causing it.

In this study, we analyze the ARW and the Chenciner bubbles generated in a three-coupled PWCOs. Because the governing equation is piecewise-constant dynamics, it is relatively easy to conduct rigorous analysis. The analysis can be performed by using a calculation algorithm for using the explicit solutions derived in autonomous piecewise-constant systems [27]. By using this algorithm, the Lyapunov exponents are calculated with a precision similar to that of maps. According to the numerical experiments, a hysteresis phenomenon erodes the Chenciner bubbles in a manner similar to that of the driven PWCOs discussed in Chapter 4. However, the hysteresis does not penetrate the Chenciner bubbles as observed in the non-autonomous system. In order to clarify the mechanism of the hysteresis phenomenon, a two-coupled delayed logistic map is considered. The hysteresis phenomenon is partially clarified as a result of a subcritical Neimark-Sacker bifurcations.

5.2 Circuit setup

Figure 5.2.1 shows an autonomous three-coupled circuit, which consists of three PWCOs as introduced in Chapter 2. Each oscillator is connected by a capacitor. The voltage across three capacitors C_1, C_2, and C_3, are denoted by v_1, v_2 and v_3, respectively. $H_1(v_1)$, $H_2(v_2)$ and $H_3(v_3)$ are the three hysteresis elements with the characteristics that are explained in Fig. 2.2.1(b). The governing equation of the three-coupled autonomous circuits is represented as the following equations

from Kirchhoff's law.

$$
\begin{aligned}
C\frac{\mathrm{d}v_1}{\mathrm{d}t} &= \left(\frac{(C_b+C_3)(C_a+C_2+C_b)}{C_aC_b} - \frac{C_b^2}{C_aC_b}\right)H_1(v_1) + \frac{C_b+C_3}{C_b}H_2(v_2) + H_3(v_3),\\
C\frac{\mathrm{d}v_2}{\mathrm{d}t} &= \frac{C_b+C_3}{C_b}H_1(v_1) + \frac{(C_a+C_1)(C_b+C_3)}{C_aC_b}H_2(v_2) + \frac{C_a+C_1}{C_a}H_3(v_3),\\
C\frac{\mathrm{d}v_3}{\mathrm{d}t} &= H_1(v_1) + \frac{C_a+C_1}{C_a}H_2(v_2) + \left(\frac{(C_a+C_1)(C_a+C_2+C_b)}{C_aC_b} - \frac{C_a^2}{C_aC_b}\right)H_3(v_3),
\end{aligned}
\tag{5.1}
$$

where

$$
\begin{aligned}
C_1 =\ & C_2 = C_3,\\
C =\ & \frac{(C_1+C_a)(C_a+C_b+C_2)(C_b+C_3)}{C_aC_b}\\
& \frac{-C_1^2(C_b+C_3) - C_b^2(C_1+C_a)}{C_aC_b}.
\end{aligned}
\tag{5.2}
$$

Via rescaling,

$$
\begin{gathered}
v_1 = V_{th1}x,\ v_2 = V_{th2}y,\ v_3 = V_{th3}z,\ t = \gamma\tau,\\
h_1(x)I_{h1} = H_1(V_{th1}x),\ h_2(y)I_{h2} = H_2(V_{th2}y),\ h_3(z)I_{h3} = H_3(V_{th3}z),\\
\frac{\gamma I_{h1}C_aC_b}{V_{th1}\big((C_1+C_a)(C_a+C_2+C_b)(C_b+C_3) - C_1^2(C_b+C_3) - C_b^2(C_1+C_a)\big)} = 1,\\
\frac{I_{h2}}{I_{h1}} = D_1,\ \frac{V_{th1}}{V_{th2}} = D_2,\ \frac{I_{h3}}{I_{h1}} = D_3,\ \frac{V_{th1}}{V_{th3}} = D_4,\\
\frac{C_a+C_1}{C_a} = D_5,\ \frac{C_b+C_1}{C_b} = D_6,
\end{gathered}
\tag{5.3}
$$

the circuit dynamics is written by

$$\begin{aligned}
\dot{x} &= (D_5 + D_5D_6 - 1)h_1(x) + D_1D_6h_2(y) + D_3h_3(z), \\
\dot{y} &= D_2D_6h_1(x) + D_1D_2D_5D_6h_2(y) + D_2D_3D_5h_3(z), \\
\dot{z} &= D_4h_1(x) + D_1D_4D_5h_2(y) + D_3D_4(D_6 + D_5D_6 - 1)h_3(z),
\end{aligned} \tag{5.4}$$

where $\left(\cdot = \dfrac{\mathrm{d}}{\mathrm{d}\tau}\right)$ denotes a differentiation by the normalized time τ. $h_1(x)$, $h_2(y)$, and $h_3(z)$ are normalized hysteresis loops, which are denoted in Fig. 5.2.2. The circuit dynamics contain six parameters: D_1, D_2, D_3, D_4, D_5, and D_6. Throughout this study, we restrict our attention to the case for which $-1 \leq x(\tau) \leq 1$, $-1 \leq y(\tau) \leq 1$ and $-1 \leq z(\tau) \leq 1$ hold for $\forall\tau$. In our assumption, the trajectory must hit the boundaries $x = 1, x = -1, y = 1, y = -1, z = 1$ or $z = -1$, successively.

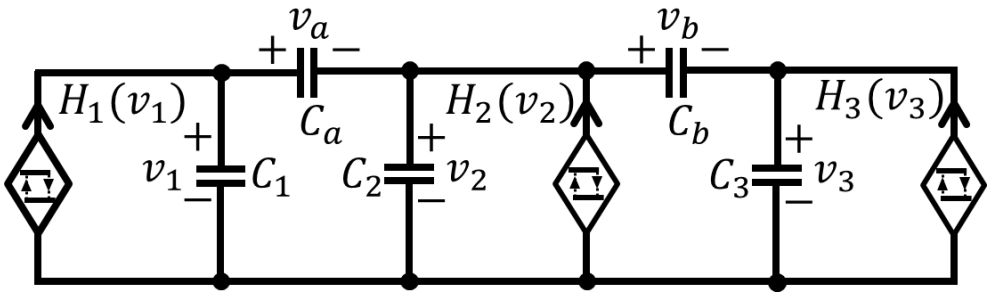

(a) Circuit model.

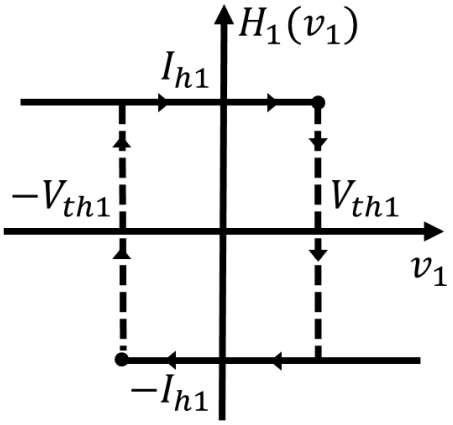

(b) $v-i$ characteristics of $H_1(v_1)$.

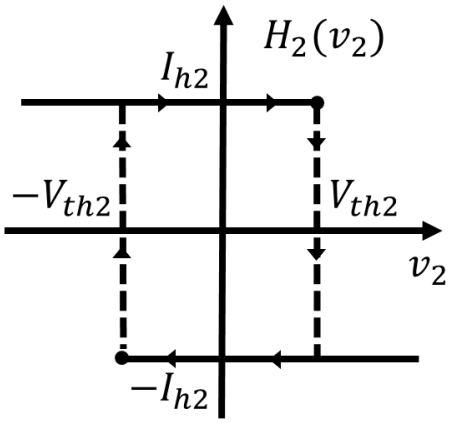

(c) $v-i$ characteristics of $H_2(v_2)$.

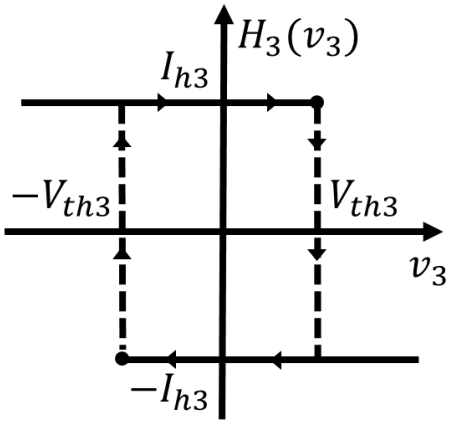

(d) $v-i$ characteristics of $H_3(v_3)$.

Figure 5.2.1 Circuit model of a three-coupled PWCOs.

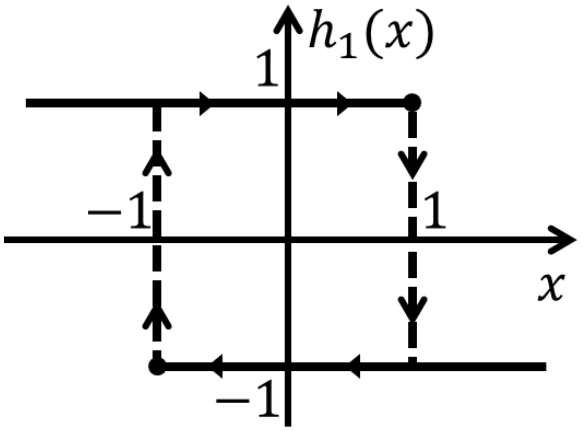

(a) $h_1(x)$.

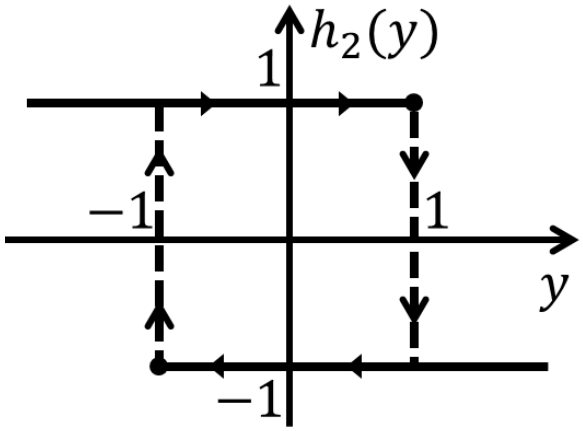

(b) $h_2(y)$.

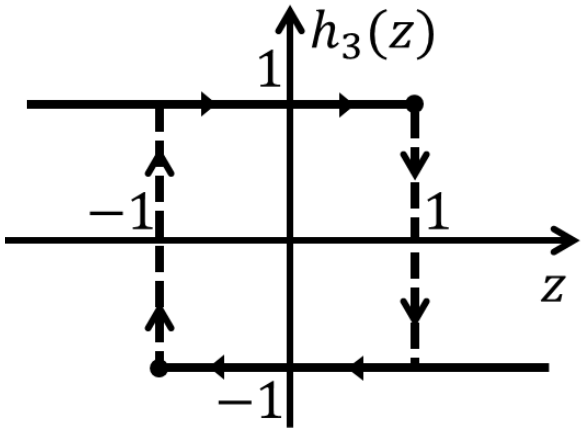

(c) $h_3(z)$.

Figure 5.2.2 Normalized hysteresis loops.

5.3 Oscillation behaviors

In order to explain the behaviors of the circuit dynamics, we rewrite Eq. 5.4 as follows:

$$\begin{aligned}
\dot{x} &= k_{xi} = (D_5 + D_5D_6 - 1)h_1(x) + D_1D_6h_2(y) + D_3h_3(z), \\
\dot{y} &= k_{yi} = D_2D_6h_1(x) + D_1D_2D_5D_6h_2(y) + D_2D_3D_5h_3(z), \\
\dot{z} &= k_{zi} = D_4h_1(x) + D_1D_4D_5h_2(y) + D_3D_4(D_6 + D_5D_6 - 1)h_3(z).
\end{aligned} \tag{5.5}$$

Since the hysteresis loop takes two values: 1 and -1, $\boldsymbol{k}(i) = (k_{xi}, k_{yi}, k_{zi})^\top$ takes constant values. The notation $^\top$ represents the transpose of the vector. Using these notations, the circuit dynamics are expressed as follows:

$$\dot{\boldsymbol{x}} = \boldsymbol{k}(i) \in D(i), \quad i \in \{0, 1, ..., 7\}, \tag{5.6}$$

where $\boldsymbol{x} = (x, y, z)^\top$, and i is an index for indicating the region $D(i)$. $\boldsymbol{k}(i)$ and region $D(i)$ are summarized in Table 5.1. For example, in the case of $i = 0$, since $h_1(x) = h_2(y) = h_3(z) = 1$, we can obtain $\boldsymbol{k}(0)$ as follows:

$$\boldsymbol{k}(0) = \begin{pmatrix} k_{x0} \\ k_{y0} \\ k_{z0} \end{pmatrix} = \begin{pmatrix} D_5 + D_5D_6 - 1 + D_1D_6 + D_3 \\ D_2D_6 + D_1D_2D_5D_6 + D_2D_3D_5 \\ D_4 + D_1D_4D_5 + D_3D_4(D_6 + D_5D_6 - 1) \end{pmatrix}.$$

Figures 5.3.1(a)–(c) represent the oscillatory behaviors projected onto the $x-y$, $x-z$, and $y-z$ plane, respectively. In these figures, the trajectory leaving $\boldsymbol{x}_0 = (x_0, y_0, z_0)^\top$, which is marked by the red solid circle on the boundary $x = -1$ of region $D(0)$, will arrive at $\boldsymbol{x}_1$, which is marked by the green solid

Table 5.1 Values of $\boldsymbol{k}(i)$

i	$\boldsymbol{k}(i) = (k_{xi}, k_{yi}, k_{zi})^\top$	Regions $D(i)$
0	$\begin{pmatrix} (D_5 + D_5D_6 - 1) + D_1D_6 + D_3 \\ D_2D_6 + D_1D_2D_5D_6 + D_2D_3D_5 \\ D_4 + D_1D_4D_5 + D_3D_4(D_6 + D_5D_6 - 1) \end{pmatrix}$	$h_1(x) = 1,\ h_2(y) = 1,\ h_3(z) = 1$
1	$\begin{pmatrix} (D_5 + D_5D_6 - 1) + D_1D_6 - D_3 \\ D_2D_6 + D_1D_2D_5D_6 - D_2D_3D_5 \\ D_4 + D_1D_4D_5 - D_3D_4(D_6 + D_5D_6 - 1) \end{pmatrix}$	$h_1(x) = 1,\ h_2(y) = 1,\ h_3(z) = -1$
2	$\begin{pmatrix} (D_5 + D_5D_6 - 1) - D_1D_6 + D_3 \\ D_2D_6 - D_1D_2D_5D_6 + D_2D_3D_5 \\ D_4 - D_1D_4D_5 + D_3D_4(D_6 + D_5D_6 - 1) \end{pmatrix}$	$h_1(x) = 1,\ h_2(y) = -1,\ h_3(z) = 1$
3	$\begin{pmatrix} (D_5 + D_5D_6 - 1) - D_1D_6 - D_3 \\ D_2D_6 - D_1D_2D_5D_6 - D_2D_3D_5 \\ D_4 - D_1D_4D_5 - D_3D_4(D_6 + D_5D_6 - 1) \end{pmatrix}$	$h_1(x) = 1,\ h_2(y) = -1,\ h_3(z) = -1$
4	$\begin{pmatrix} -(D_5 + D_5D_6 - 1) + D_1D_6 + D_3 \\ -D_2D_6 + D_1D_2D_5D_6 + D_2D_3D_5 \\ -D_4 + D_1D_4D_5 + D_3D_4(D_6 + D_5D_6 - 1) \end{pmatrix}$	$h_1(x) = -1,\ h_2(y) = 1,\ h_3(z) = 1$
5	$\begin{pmatrix} -(D_5 + D_5D_6 - 1) + D_1D_6 - D_3 \\ -D_2D_6 + D_1D_2D_5D_6 - D_2D_3D_5 \\ -D_4 + D_1D_4D_5 - D_3D_4(D_6 + D_5D_6 - 1) \end{pmatrix}$	$h_1(x) = -1,\ h_2(y) = 1,\ h_3(z) = -1$
6	$\begin{pmatrix} -(D_5 + D_5D_6 - 1) - D_1D_6 + D_3 \\ -D_2D_6 - D_1D_2D_5D_6 + D_2D_3D_5 \\ -D_4 - D_1D_4D_5 + D_3D_4(D_6 + D_5D_6 - 1) \end{pmatrix}$	$h_1(x) = -1,\ h_2(y) = -1,\ h_3(z) = 1$
7	$\begin{pmatrix} -(D_5 + D_5D_6 - 1) - D_1D_6 - D_3 \\ -D_2D_6 - D_1D_2D_5D_6 - D_2D_3D_5 \\ -D_4 - D_1D_4D_5 - D_3D_4(D_6 + D_5D_6 - 1) \end{pmatrix}$	$h_1(x) = -1,\ h_2(y) = -1,\ h_3(z) = -1$

circle on the boundary $z = 1$. If z reaches the threshold $z = 1$, $h_3(z)$ switches from 1 to -1. The trajectory transitions from region $D(0)$ with $\boldsymbol{k}(0)$ to region $D(1)$ with $\boldsymbol{k}(1)$. In such a case, x and y increase and z decreases. Next, the trajectory arrives $\boldsymbol{x}_2$, which is marked by the blue solid circle on the boundary

$y = 1$. At this instant, $h_2(y)$ switches from 1 to -1. The trajectory transitions from region $D(1)$ with $\boldsymbol{k}(1)$ to region $D(3)$ with $\boldsymbol{k}(3)$. It moves linearly to the boundary $x = 1$. Similarly, the trajectory transitions from region $D(i)$ to region $D(j)$, $i, j \in \{0, 1, ..., 7\}$, when it strikes the boundary $x = 1, x = -1, y = 1, y = -1, z = 1$ or $z = -1$. The trajectory will repeat again these behaviors.

Next, by changing D_2 and D_4, we introduce some patterns of the trajectory. We set initial values: $\big(x_0, y_0, z_0, h_1(x_0), h_2(y_0), h_3(z_0)\big) = (-1.0, 0.1, 0.7, 1, 1, 1)$ at $\tau = 0$. We draw the trajectory from $\tau = 50$ to $\tau = 50.005$. Our numerical results show that $\tau = 50$ is enough as a transient time. In these simulations, Fig. (a)–(c) show attractors projected onto the $x - y$, $x - z$, and $y - z$ plane, respectively; Fig. (d)–(f) show time waveforms of the state variables x, y, and z, respectively. We fix the constant parameters as follows: $D_1 = 1.2, D_3 = 1.5, D_5 = D_6 = 101$. The trajectory shows a periodic oscillation at $D_2 = 0.84, D_4 = 0.67$ as shown in Fig. 5.3.2. By contrast, a quasi-periodic oscillation is observed at $D_2 = 0.8525, D_4 = 0.669$ as shown in Fig. 5.3.3.

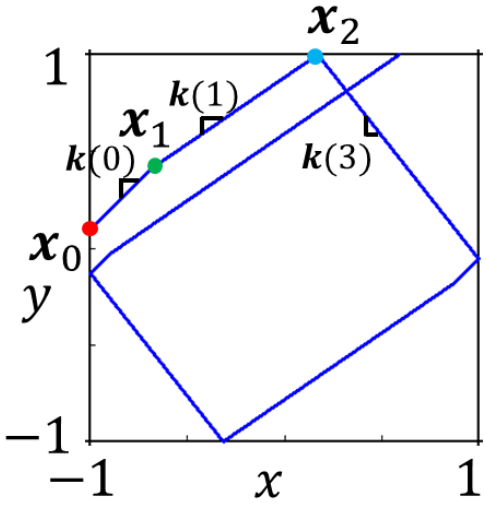

(a) $x - y$.

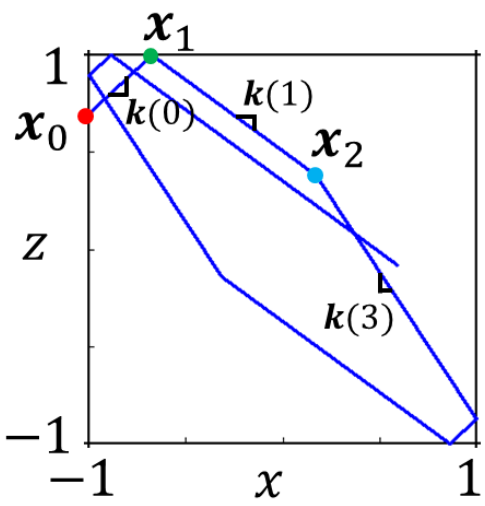

(b) $x - z$.

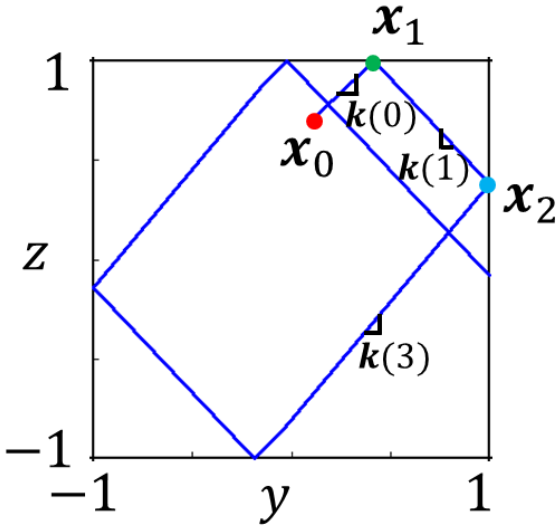

(c) $y - z$.

Figure 5.3.1 Example of oscillation behaviors.

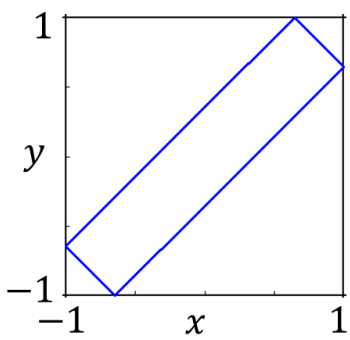

(a) $x - y$.

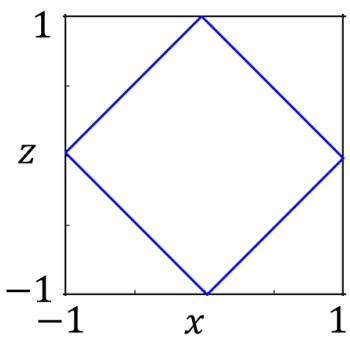

(b) $x - z$.

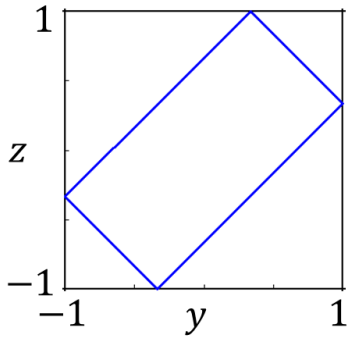

(c) $y - z$.

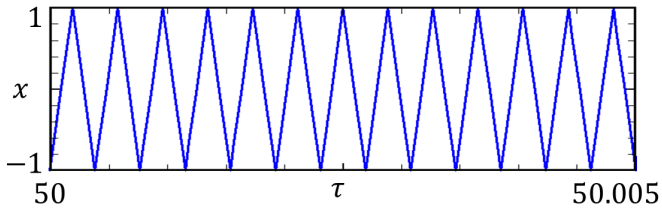

(d) Time waveform of x.

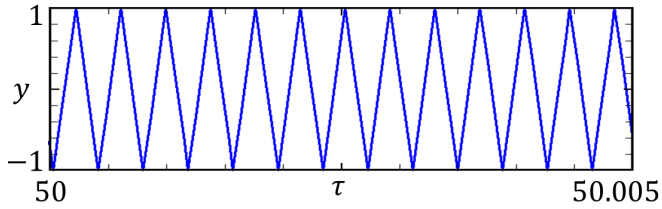

(e) Time waveform of y.

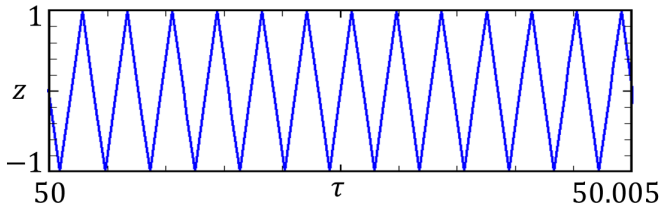

(f) Time waveform of z.

Figure 5.3.2 Periodic oscillation ($D_2 = 0.84, D_4 = 0.67$).

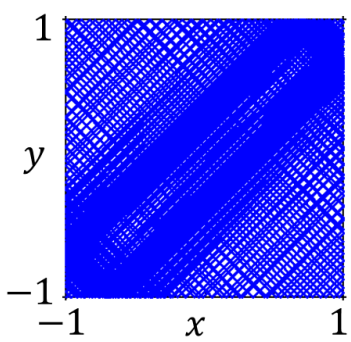

(a) $x - y$.

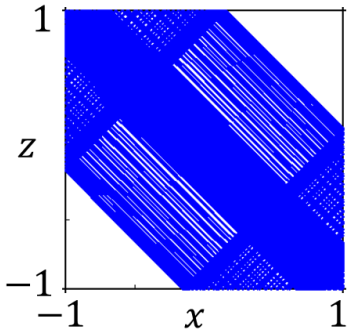

(b) $x - z$.

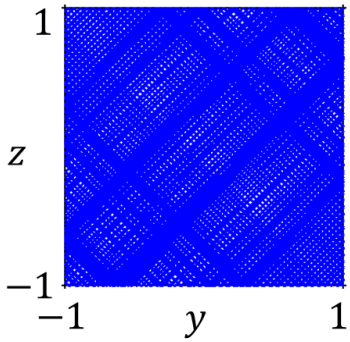

(c) $y - z$.

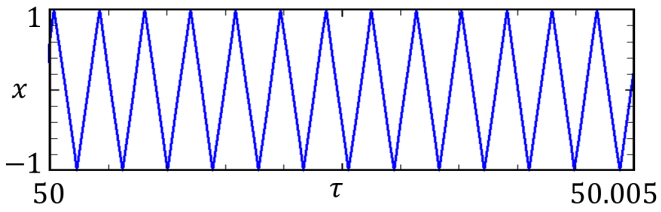

(d) Time waveform of x.

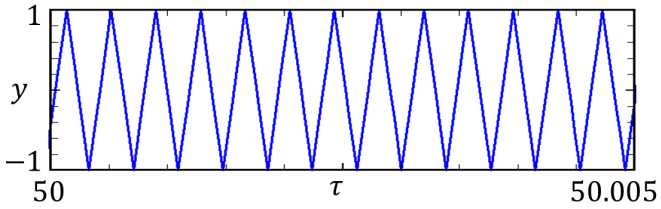

(e) Time waveform of y.

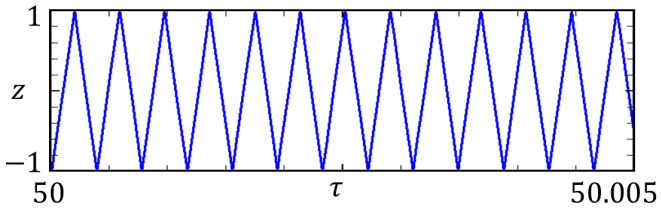

(f) Time waveform of z.

Figure 5.3.3 Quasi-periodic oscillation ($D_2 = 0.8525, D_4 = 0.669$).

5.4 Calculation algorithm for deriving the rigorous solutions

In this section, we introduce a calculation algorithm for deriving the explicit solutions in the autonomous three-coupled PWCOs. The calculation of the trajectories can be accomplished by the following 4 steps.

STEP 1

We provide the initial values $\big(x_0, y_0, z_0, h_1(x_0), h_2(y_0), h_3(z_0)\big)$ and obtain the region containing the initial values by referring to Table 5.1.

STEP 2

We calculate the time τ when the trajectory leaving $\boldsymbol{x}_0 = (x_0, y_0, z_0)^\top$ arrives at $\boldsymbol{x}_1 = (x_1, y_1, z_1)^\top$ on the boundary, i.e., either one of $x = 1$, $x = -1$, $y = 1$, $y = -1$, $z = 1$, and $z = -1$. The state $\boldsymbol{x}_1$ is calculated by

$$\boldsymbol{x}_1 = \boldsymbol{x}_0 + \boldsymbol{k}(i) \cdot \tau, \tag{5.7}$$

where $\boldsymbol{k}(i)$ is obtained from Table 5.1. By introducing a normal vector $\boldsymbol{n}^\top$, the boundary condition can be expressed as the following form:

$$\boldsymbol{n}^\top \cdot \boldsymbol{x}_1 = P, \tag{5.8}$$

where P is a constant value; $\boldsymbol{n}^\top$ and P are listed in Table 5.2. For example, if the trajectory arrives at $y = 1$ with the normal vector $\boldsymbol{n}^\top = (0\ 1\ 0)$ at $\boldsymbol{x}_1 = (x_1, y_1, z_1)^\top = (x_1, 1, z_1)^\top$, the scalar P is $P = 1$.

Substituting Eq. 5.7 into Eq. 5.8 yields

$$\tau = \frac{P - \boldsymbol{n}^\top \cdot \boldsymbol{x}_0}{\boldsymbol{n}^\top \cdot \boldsymbol{k}(i)}. \tag{5.9}$$

For example, we calculate the time when the trajectory leaving $\boldsymbol{x}_0$ on the boundary $x = -1$ corresponding to region $D(0)$ hits the boundary $x = 1$, $y = 1$, $z = 1$ corresponding to region $D(4)$, $D(2)$, and $D(1)$ respectively.

If the trajectory reaches the boundary $x = 1$, the time τ_1 is explicitly expressed as

$$\tau_1 = \frac{P - \boldsymbol{n}^\top \cdot \boldsymbol{x}_0}{\boldsymbol{n}^\top \cdot \boldsymbol{k}(0)}, \tag{5.10}$$

where $\boldsymbol{n}^\top = (1\ 0\ 0)$, and $P = 1$.

If the trajectory reaches the boundary $y = 1$, the time τ_2 is explicitly expressed as

$$\tau_2 = \frac{P - \boldsymbol{n}^\top \cdot \boldsymbol{x}_0}{\boldsymbol{n}^\top \cdot \boldsymbol{k}(0)}, \tag{5.11}$$

where $\boldsymbol{n}^\top = (0\ 1\ 0)$ and $P = 1$.

If the trajectory reaches the boundary $z = 1$, the time τ_3 is explicitly expressed as

$$\tau_3 = \frac{P - \boldsymbol{n}^\top \cdot \boldsymbol{x}_0}{\boldsymbol{n}^\top \cdot \boldsymbol{k}(0)}, \tag{5.12}$$

where $\boldsymbol{n}^\top = (0\ 0\ 1)$, and $P = 1$.

By comparing τ_1, τ_2 and τ_3, the minimum positive time is the actual switching time τ.

STEP 3

By substituting τ to Eq. 5.7, $\boldsymbol{x}_1$ is explicitly calculated. Depending on the region $D(i)$, $\boldsymbol{k}(i)$ is also obtained.

STEP 4

We substitute $\boldsymbol{x}_1$ into $\boldsymbol{x}_0$ and go to **STEP 2**.

Table 5.2 Boundary conditions.

	$\boldsymbol{n}^\top$	P
$x = 1$	(1 0 0)	1
$x = -1$	(1 0 0)	-1
$y = 1$	(0 1 0)	1
$y = -1$	(0 1 0)	-1
$z = 1$	(0 0 1)	1
$z = -1$	(0 0 1)	-1

5.5 Lyapunov analysis

In this section, we conduct Lyapunov analysis to determine the solutions as periodic, quasi-periodic, or chaotic by using the calculation algorithm, which is described in Section 5.4. The Lyapunov exponents or the Lyapunov characteristic exponents of a dynamical system express the rate how the solutions that are located in close proximity expand or converge. Computational algorithms for deriving the Lyapunov exponents were given by Shimada and Nagashima [63]. In general, n-dimensional autonomous ODEs have n Lyapunov exponents. Let

the first, second and n-th Lyapunov exponents be denoted by λ_1, λ_2, $\cdots$, λ_n, respectively ($\lambda_1 \geq \lambda_2 \geq \cdots \geq \lambda_n$).

- The solution is periodic if $\lambda_1 < 0$.
- The solution is two-dimensinal tori if $\lambda_1 = 0$ and $\lambda_2 < 0$.
- The solution is three-dimensinal tori if $\lambda_1 = \lambda_2 = 0$ and $\lambda_3 < 0$.
- The solution is n-dimensinal tori if $\lambda_1 = \lambda_2 = ... = \lambda_{n-1} = 0$ and $\lambda_n < 0$.
- The solution is chaotic if $\lambda_1 > 0$.

At first, we derive the Jacobian matrices. Substituting Eq. 5.9 to Eq. 5.7 yields the following equation:

$$\boldsymbol{x}_1 = \left(I_n - \frac{\boldsymbol{k}(i)\boldsymbol{n}^\top}{\boldsymbol{n}^\top \boldsymbol{k}(i)} \right) \boldsymbol{x}_0 + \frac{\boldsymbol{k}(i)P}{\boldsymbol{n}^\top \boldsymbol{k}(i)}, \tag{5.13}$$

It is clear from Eq. 5.13 that the local Jacobian matrix is represented by

$$A = \frac{\mathrm{d}\boldsymbol{x}_1}{\mathrm{d}\boldsymbol{x}_0} = I_n - \frac{\boldsymbol{k}(i)\boldsymbol{n}^\top}{\boldsymbol{n}^\top \boldsymbol{k}(i)}, \tag{5.14}$$

where I_n denotes an identity matrix.

Then, if the solution strikes $x = 1$ or $x = -1$,

$$A_0 = \begin{pmatrix} 0 & 0 & 0 \\ -k_{yi}/k_{xi} & 1 & 0 \\ -1/k_{xi} & 0 & 1 \end{pmatrix}, \tag{5.15}$$

if the solution strikes $y = 1$ or $y = -1$,

$$A_1 = \begin{pmatrix} 1 & -k_{xi}/k_{yi} & 0 \\ 0 & 0 & 0 \\ 0 & -1/k_{yi} & 1 \end{pmatrix}, \tag{5.16}$$

and if the solution strikes $z = 1$ or $z = -1$,

$$A_2 = \begin{pmatrix} 1 & 0 & -k_{xi} \\ 0 & 1 & -k_{yi} \\ 0 & 0 & 0 \end{pmatrix}. \tag{5.17}$$

Next, based on the procedure of calculating Lyapunov exponent in Ref. [63], we use Eq. (5.13) and (5.14) to define the first and the second Lyapunov exponent as follows.

$$\begin{aligned} \lambda_1 &\simeq \frac{1}{N} \sum_{j=M+1}^{M+N} \ln \left| A_i^j e_1^j \right|, \\ \lambda_1 + \lambda_2 &\simeq \frac{1}{N} \sum_{j=M+1}^{M+N} \ln \left| A_i^j e_1^j \times A_i^j e_2^j \right|, \end{aligned} \tag{5.18}$$

where e_1^j and e_2^j are orthonormal bases, and $A_i^j = \dfrac{\mathrm{d}\boldsymbol{x}_1}{\mathrm{d}\boldsymbol{x}_0}$ is the Jacobian matrix, which is one of A_0, A_1 and A_2. M and N are positive integers. It is reasonable to set $M = N = 2 \times 10^7$ to exactly calculate the two Lyapunov exponents. Each Lyapunov exponent can be regarded to be zero if calculated exponent satisfies following condition.

$$|\lambda_i| < 1/10^6. \tag{5.19}$$

We use the first and the second Lyapunov exponent to obtain some two-parameter Lyapunov diagrams as shown in Fig. 5.5.1. We fix the coupling

parameters $C_a/C = C_b/C = 0.01$ that correspond to $D_5 = D_6 = 101$. Let D_2 and D_4 be the bifurcation parameters, which lie on the horizontal and vertical axis, respectively. We set up the parameters $D_1 = 1.2, D_3 = 1.5$ and $D_5 = D_6 = 101$. A continuous deformation method is used when the bifurcation parameters are varied. D_2 is varied from D_{2_present} to D_{2_next} as tracing parameter from left-hand side to right-hand side ($D_{2\_\mathrm{present}} < D_{2\_\mathrm{next}}$). The relationship between D_{2_present} and D_{2_next} is described by

$$D_{2\_\mathrm{next}} = D_{2\_\mathrm{present}} + \Delta D_2, \tag{5.20}$$

where ΔD_2 is chosen to be small ($0 < \Delta D_2 < 1$).
The final value $\big(x_1, y_1, z_1, h_1(x_1), h_2(y_1), h_3(z_1)\big)$ at D_{2_present} is substituted into the initial value $\big(x_0, y_0, z_0, h_1(x_0), h_2(y_0), h_3(z_0)\big)$ at D_{2_next}. Subsequently, let D_{2_present} be replaced by D_{2_next}. This procedure is repeated untill D_2 reaches the final value at $D_2 = 0.865$. D_4 is traced in the same procedure as varying D_2.

In the Fig. 5.5.1, the region generating periodic solutions ($\lambda_1 < 0$) is marked by gray where the ratio of the three oscillations is $1 : 1 : 1$. This region can be denoted as Chenciner bubbles. The regions generating two-dimensional tori ($\lambda_1 = 0, \lambda_2 < 0$) and three-dimensional tori ($\lambda_1 = 0, \lambda_2 = 0$) are marked by blue and yellow, respectively. The regions generating chaos are marked by black. As seen in this figure, the bifurcation structure called an Arnol'd resonance web is observed. Moreover, chaos is inevitably observed in a region near the Chenciner

bubbles.

In these figures, the red arrows show the direction of the tracing parameter. We set the same initial values, i.e. $(x_0, y_0, z_0, h_1(x_0), h_2(y_0), h_3(z_0))$ for different initial parameter values. For example, in Fig. 5.5.1(a), we choose the initial values at the bottom left and set initial parameter values by varying D_2 from the bottom left to the bottom right. We trace the parameter D_4 from the bottom to the top. By contrast, in Fig. 5.5.1(b) we trace D_4 from the top to the bottom with the same manner indicated in Fig. 5.5.1(a). The results represent that the bifurcation structures depend on the initial parameter values. The periodic solution and two-dimentional tori coexist in the phase space for differrent initial conditions, although we set up the same values of parameters. Figures 5.5.2(a) and (b) are enlargements of Fig. 5.5.1(a) and (b), respectively. At point Q, there exist both the periodic solution and two-dimensional tori. The coexistence of these solutions is evident if we choose the initial parameter point at the left bottom and we trace D_2 from left to right as shown in Fig. 5.5.1(c). The coexistence gives rise to a hysteresis phenomenon.

Let us assume that D_2 and D_4 are $D_2 = 0.83, D_4 = 0.657$. By changing initial values, we can observe both the periodic solution and two-dimensional tori, which are obtained at point Q, as shown in Fig. 5.5.3. By using the initial values $(x_0, y_0, z_0) = (-0.25, -0.1, 0.9)$ with hysteresis informations $\big(h_1(x), h_2(y), h_3(z)\big) = (1, 1, 1)$, the periodic oscillation projecting onto the $y - z$ plane is shown in

Fig. 5.5.3(a). The corresponding attractor that becomes a single point on section $\pi_{x1} = \{\boldsymbol{x}|x = 1\}$ is shown in Fig. 5.5.3(b). By contrast, when we use the slightly different initial values $(x_0, y_0, z_0) = (0.1, -0.9, 0.9)$ with hysteresis informations $\big(h_1(x), h_2(y), h_3(z)\big) = (1, 1, 1)$, the two-dimensional tori appears as shown in Fig. 5.5.3(c). The corresponding attractor on section π_{x1} is shown in Fig. 5.5.3(b).

Next, we clarify the basin boundary between the periodic solution and two-dimensional tori. For simplicity, we fix the hysteresis informations: $h_1(x) = h_2(y) = h_3(z) = 1$. If the solution is a periodic solution or two-dimensional tori, we plot the gray or blue point, respectively, on the plane $x - y$. Let x and y denote the horizontal and vertical axis in the figure. Noting that, because we restrict our attention to the case when $-1 \leq x, y \leq 1$, x and y is varied in a range of $[-1, 1]$. The basins of these solutions obtained at the point Q $(D_2 = 0.83, D_4 = 0.657)$ is shown in Fig. 5.5.4. It shows a complicated basin boundary. In the situation of Fig. 5.5.4, which of the periodic solution or two-dimensional tori is observed depends on the region which the intial values are located.

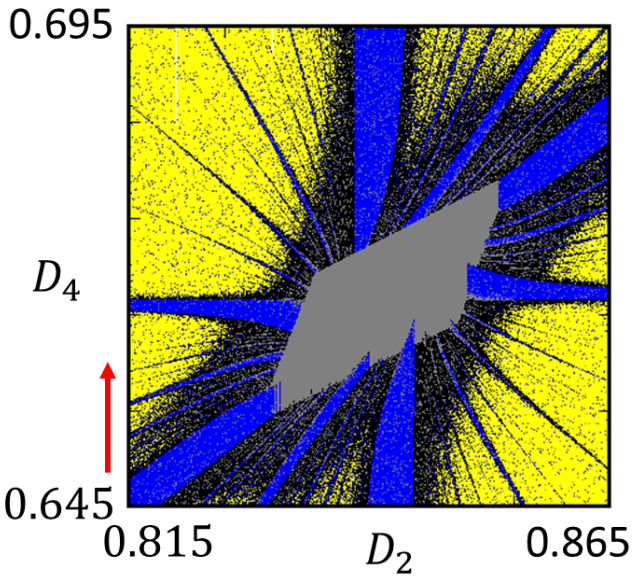

(a) Bottom left.

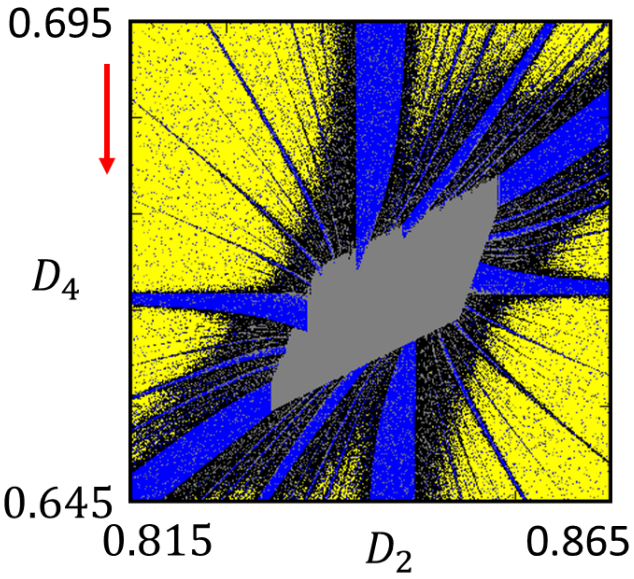

(b) Top left.

Figure 5.5.1 Lyapunov diagrams obtained using different initial parameter values ($D_1 = 1.2, D_3 = 1.5$, and $D_5 = D_6 = 101$).

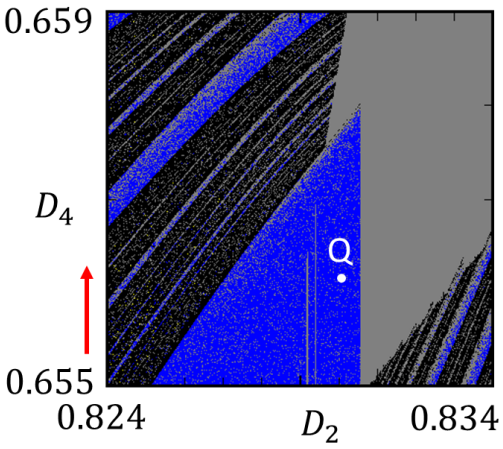

(a) Magnified view of Fig. 5.5.1(a).

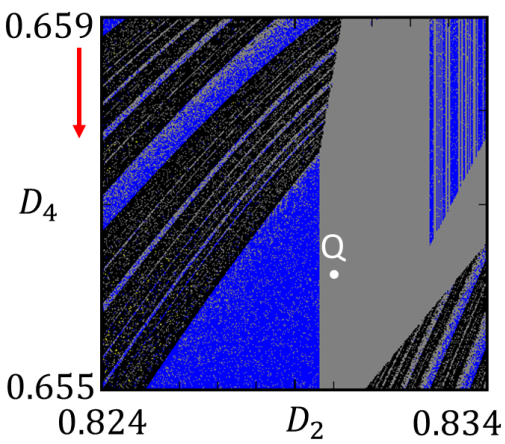

(b) Magnified view of Fig. 5.5.1(b).

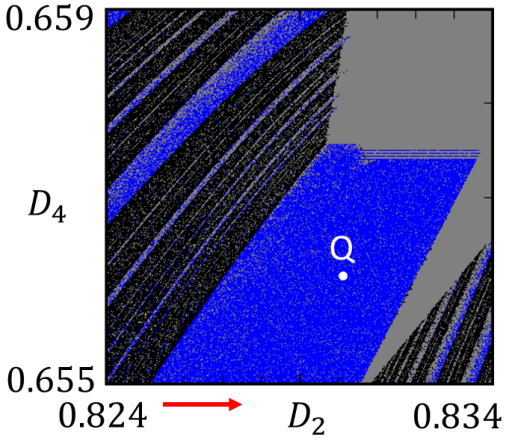

(c) Magnified view of Fig. 5.5.1(b) with D_2 tracing from left to right.

Figure 5.5.2 Magnified view of Fig. 5.5.1 ($D_1 = 1.2, D_3 = 1.5$, and $D_5 = D_6 = 101$).

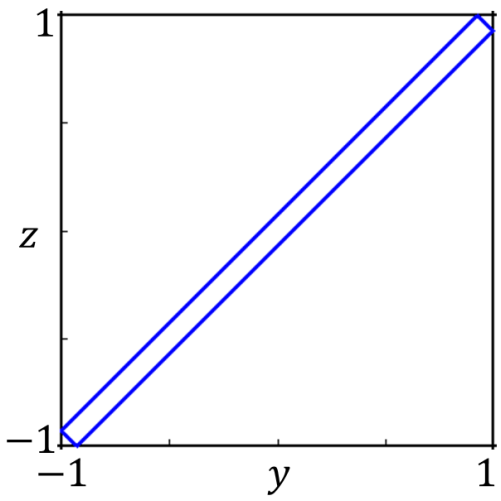

(a) Periodic solution with the initial values $(x_0, y_0, z_0) = (-0.25, -0.1, 0.9)$ and $h_1(x) = h_2(y) = h_3(z) = 1$.

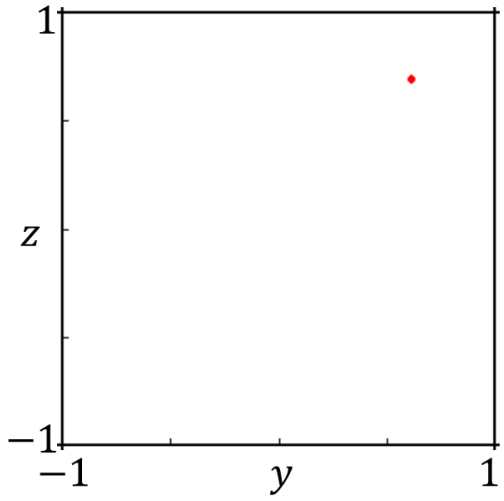

(b) Corresponding point on the section π_{x_1}.

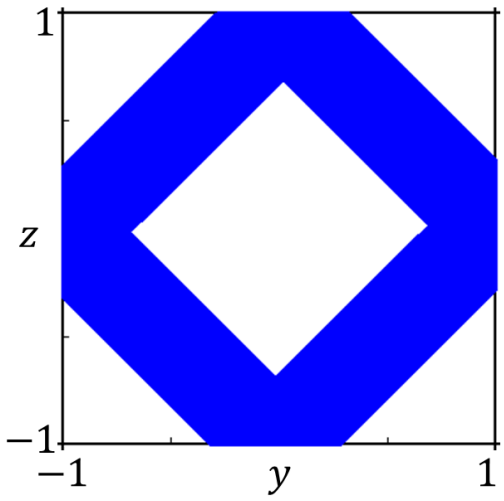

(c) Two-dimensional tori with the initial values $(x_0, y_0, z_0) = (0.1, -0.9, 0.9)$ and $h_1(x) = h_2(y) = h_3(z) = 1$.

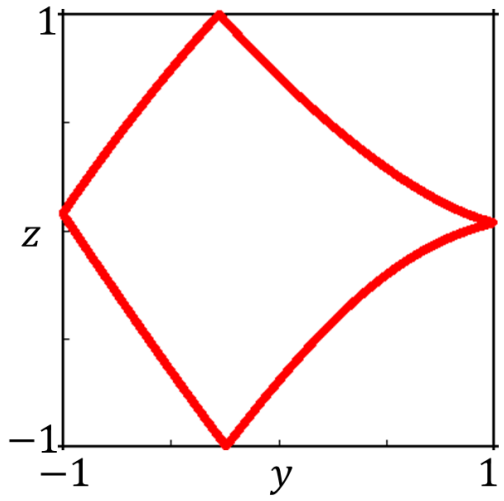

(d) Corresponding attractor on the section π_{x_1}.

Figure 5.5.3 Coexistence of the periodic solution and two-dimensional tori obtained at point Q $(D_2 = 0.83, D_4 = 0.657)$.

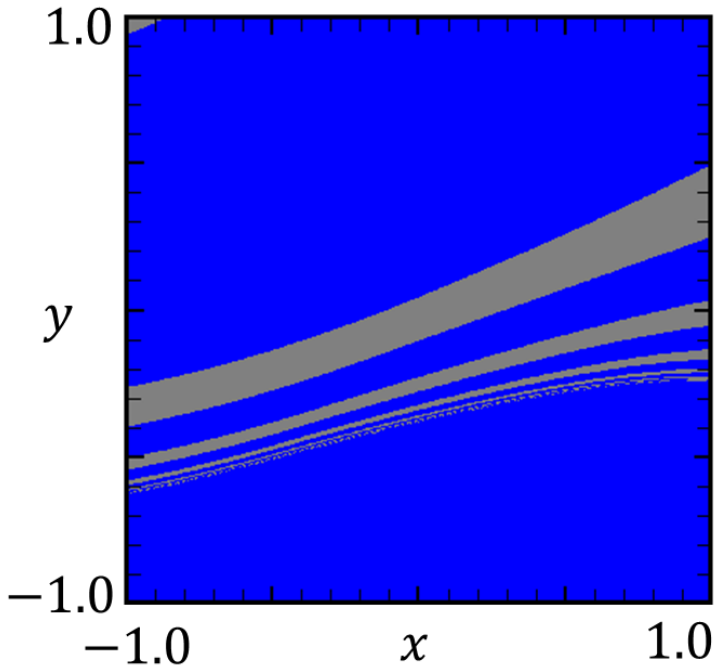

Figure 5.5.4 Basins of the periodic solution and the two-dimensional tori at point Q $(D_2 = 0.83, D_4 = 0.657)$.

5.6 Farey sequences

The Farey sequence is found to be related to the generation patterns of the two-dimensional tori. Numerical observation of this series have been proposed in a non-autonomous electric circuit of two-coupled PWCOs driven by a rectangular wave forcing [53]. In this section, we confirm the generation of this series in three-coupled PWCOs.

At first, Farey sequence is briefly explained. The Farey sequence is a ascending sequence of irreducible fractions between 0 and 1. For example, we give the following Farey sequence:

$$F = \left\{ \frac{0}{1}, \frac{1}{4}, \frac{1}{3}, \frac{2}{5}, \frac{1}{2} \right\}. \tag{5.21}$$

If $\frac{a}{b}, \frac{c}{d}$, and $\frac{e}{f}$ are consecutive fractions in a Farey sequence then

$$\frac{c}{d} = \frac{a+e}{b+f}. \tag{5.22}$$

To facilitate the observation of the two-dimensional tori, we magnified a view of Fig. 5.5.1 as shown in Fig. 5.6.1. Figure 5.6.2 shows various types of two-dimensional tori on the section $\pi_{x1} = \{\boldsymbol{x} | x = 1\}$ projected on the $y - z$ plane. Figures (a)–(d) correspond to points marked by $Q_1 - Q_4$ in Fig. 5.6.1. The number of times the two-dimensional tori reaches the boundary $z = -1$ is denoted by H. And the number of times the two-dimensional tori reaches the boundary $y = -1$ is denoted by K. In Fig 5.6.2(a), since $H = 0$ and $K = 1$, we can obtain the fraction $\frac{H}{K} = \frac{0}{1}$. In the same way, we can obtain the series

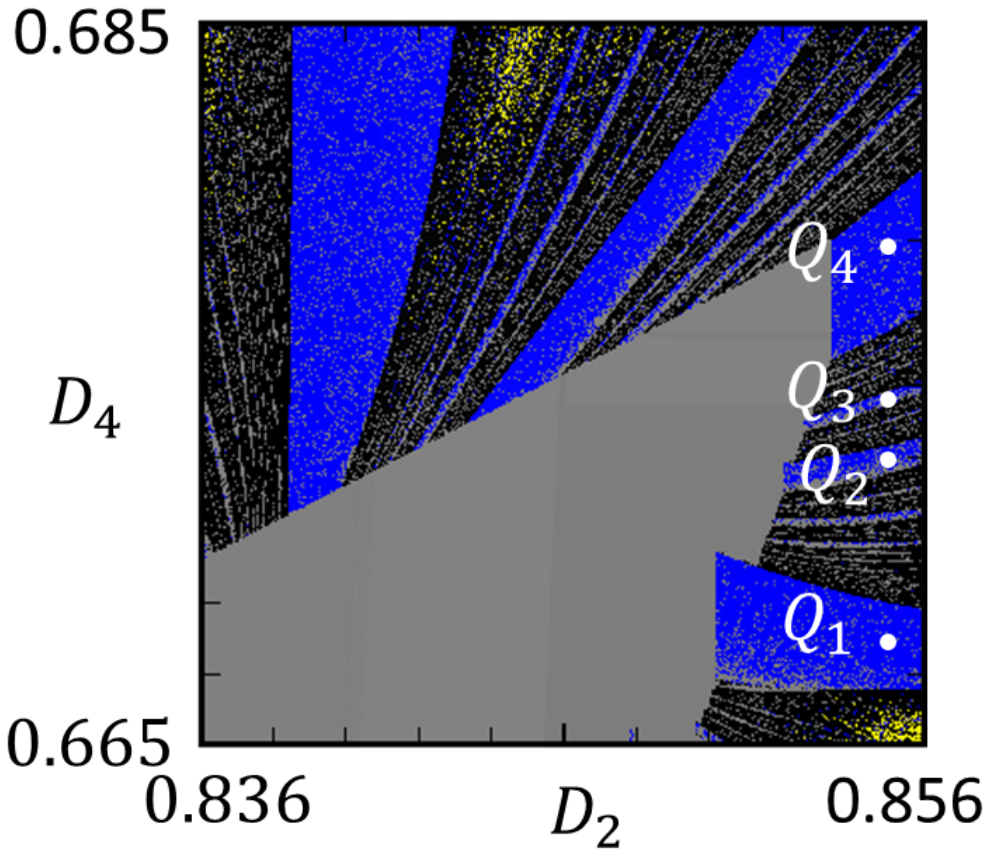

Figure 5.6.1 Magnified view of Fig. 5.5.1(b) ($D_1 = 1.2, D_3 = 1.5$, and $D_5 = D_6 = 101$).

$\left\{\frac{0}{1}, \frac{1}{2}, \frac{2}{3}, \frac{1}{1}\right\}$. Between Q_1 and Q_4, there exists Q_2, i.e., $\frac{1}{2} = \frac{0+1}{1+1}$. Similarly, between Q_2 and Q_4, there exists Q_3, i.e., $\frac{2}{3} = \frac{1+1}{2+1}$. In the same vein, Q_2 exists between Q_1 and Q_3.

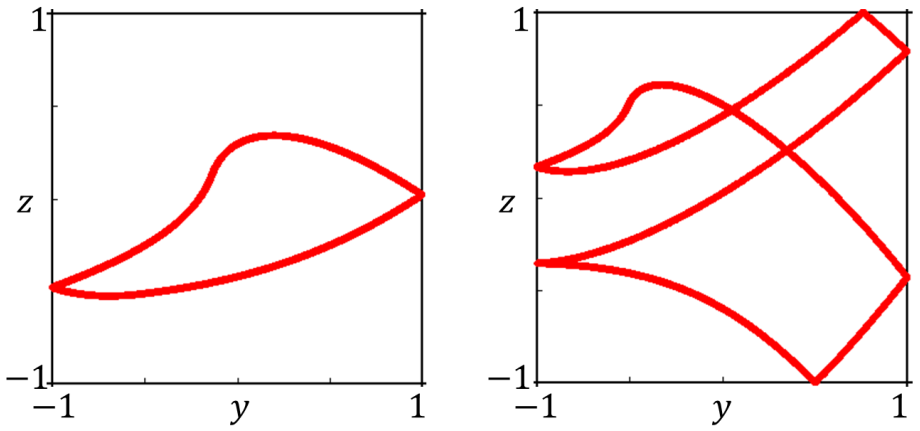

(a) $Q_1(0:1)$.

(b) $Q_2(1:2)$.

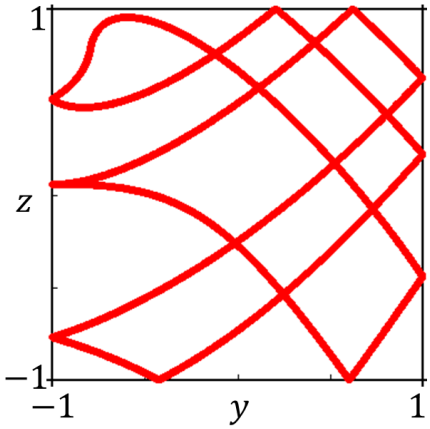

(c) $Q_3(2:3)$.

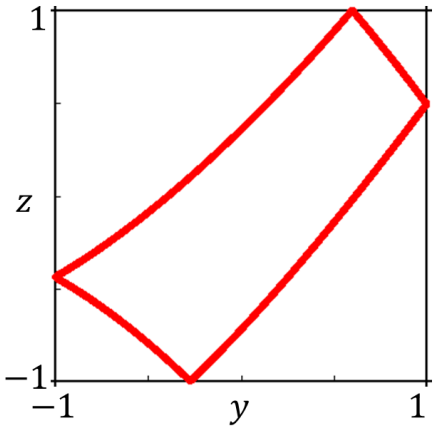

(d) $Q_4(1:1)$.

Figure 5.6.2 Farey sequences ($D_1 = 1.2, D_3 = 1.5$, and $D_5 = D_6 = 101$: (a) $D_2 = 0.855, D_4 = 0.6675$; (b) $D_2 = 0.855, D_4 = 0.6729$; (c) $D_2 = 0.855, D_4 = 0.6746$ and (d) $D_2 = 0.855, D_4 = 0.679$.

5.7 Hysteresis phenomenon of a two-coupled delayed logistic map

In section 4.5 and section 5.5, we observed the hysteresis phenomenon occurring in the three-dimensional system of PWCOs. However, the mechanism responsible for this phenomenon cannot be clarified. In this section, we focus on a two-coupled delayed logistic map to explain the mechanism causing this phenomenon.

It is known that a delayed logistic map is a typical example of discrete-time dynamics that generate an invariant closed curve (ab. ICC) corresponding to a two-dimensional tori in continuous-time dynamics. A delayed logistic map is expressed as the following equation:

$$\begin{aligned} x_{n+1} &= y_n, \\ y_{n+1} &= B y_n (1 - x_n), \end{aligned} \tag{5.23}$$

where B is a parameter.

Figures 5.7.1(a) and (b) show a one-parameter bifurcation diagram and the corresponding graph of the two Lyapunov exponent of a delayed logistic map, respectively. As seen in these figures, when $B < 2$ there exists a periodic solution with respect to the negative Lyapunov exponents. When $B = 2$, the first Lyapunov exponent becomes zero leading a generation of an ICC. It can be easily checked that the ICC is generated owing to a Neimark–Sacker (ab. N-S) bifurcation [37].

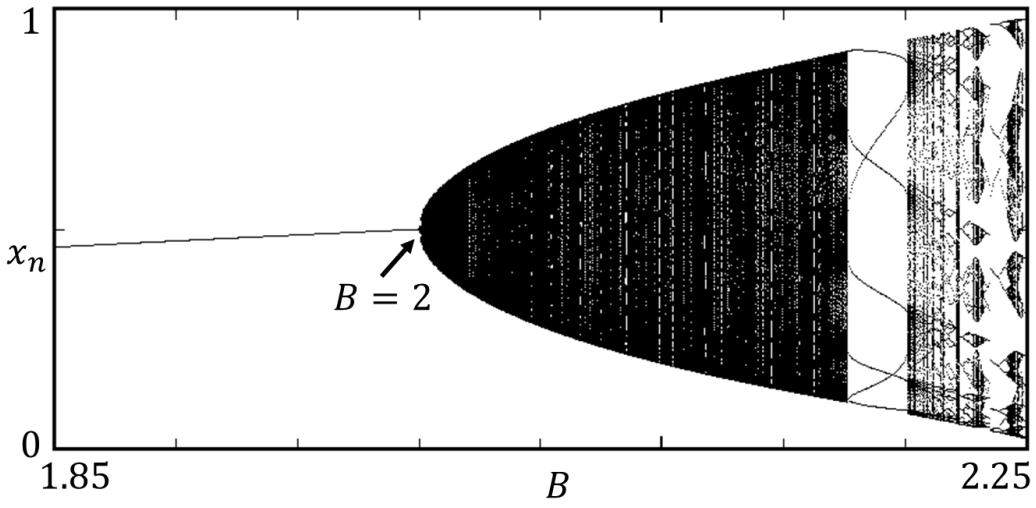

(a) One-parameter bifurcation diagram.

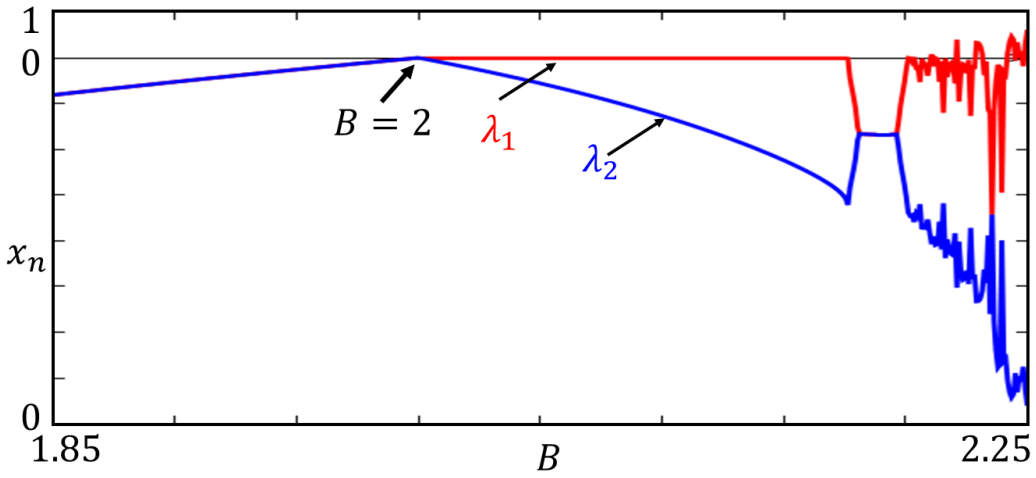

(b) Corresponding graph of the Lyapunov exponents.

Figure 5.7.1 A delayed logistic map.

Since a single delayed logistic map generates an ICC, a two-coupled one can generate an two-dimensional invariant tori (ab. IT) corresponding to a three-dimensional tori in continuous-time dynamics. The two-coupled delayed logistic map is expressed as the following equation:

$$\begin{aligned} x_{n+1} &= y_n, \\ y_{n+1} &= B_1 y_n(1 - x_n) + \varepsilon_1 w_n, \\ z_{n+1} &= w_n, \\ w_{n+1} &= B_2 w_n(1 - z_n) + \varepsilon_2 y_n, \end{aligned} \tag{5.24}$$

where ε_1 and ε_2 are coupling parameters.

We create some two-parameter Lyapunov diagrams to investigate the bifurcation structures as shown in Fig. 5.7.2(a)–(c). A continuous deformation method, which is mentioned in the previous Section, is used when the bifurcation parameters vary. The first and the second Lyapunov exponents are calculated using Eq. 5.18. Let B_1 and B_2 be bifurcation parameters, which lie on the horizontal and vertical axis, respectively. The regions-generating the periodic solution are marked by gray. The regions generating ICC and IT are marked by blue, and yellow, respectively. Arnol'd resonance web is clearly observed as shown in Fig 5.7.2(a). Figures 5.7.2(b) and (c) are magnified views of Fig. 5.7.2(a). We can observe that the hysteresis phenomenon is clearly occurred.

To analyze the hysteresis phenomenon in detail, we conduct one-parameter bifurcation diagram with ($\varepsilon_1 = 0.01$, $\varepsilon_2 = 0.02$, and $B_1 = 2.1575$) as shown in Figures 5.7.3. This diagram is obtained when the bifurcation parameter varies

B_2 along the horizontal axis. A continuous deformation method is also used to trace B_2 from left to right and vice versa as shown in Fig. 5.7.3(a) and (b), respectively. For each value of B_2, after removing the transient time, a set of state variables x_n are plotted for 10^3 iterations on the vertical axis. When B_2 increases, the periodic solutions starts at $B_2 \cong 2.02185$. However, when B_2 decreases, this solution only vanishes at $B_2 \cong 2.02177$. This result suggests that the hysteresis phenomenon occurs when it undergoes the subcritical N–S bifurcation.

The schematic diagram of the subcritical N–S bifurcation is shown in Fig. 5.7.4. The horizontal and vertical axis correspond to the bifurcation parameter B_2 and the state variable x_n, respectively. The periodic solution and ICC are denoted by red and green, respectively. In the figure, the solid line illustrates a stable solution, the dashed line illustrates an unstable one. The parameter is traced from the lower to the upper value and vice versa. We observe that in the case of increasing the parameter, the value of the parameter for which the N–S bifurcation occurs ($P_{\max}$) is higher in the case of decreasing the parameter ($P_{\min}$). In addition, there exists the coexistence of the periodic solution and ICC in the range ($P_{\min}, P_{\max}$). N–S and saddle-node bifurcation curves calculated by the algorithm proposed by Kawakami [16] are drawn in green and red, respectively, as shown in Fig. 5.7.2(b)–(c). The boundaries between the regions generating the periodic solution and ICC obtained by using Lyapunov analysis do

not coincide with the saddle-node bifurcation curves using Kawakami's shooting algorithm in Fig. 5.7.2(b) and (c). This result suggests that complicated quasi-periodic bifurcations could occur near these boundaries.

If we fix all the parmeter values: $\varepsilon_1 = 0.01, \varepsilon_2 = 0.02, B_1 = 2.1575, B_2 = 2.02165$, and vary the initial values, we can observe both the periodic solution and ICC. When we use the initial values $(x_0, y_0, z_0, w_0) = (0.475, 0.9, 0.8, 0.8)$, the solution represents a periodic attractor with period 122, which are projected onto the $x_n - y_n$ and $z_n - w_n$ plane as shown in Fig. 5.7.5(a) and (b), respectively. By contrast, when we use the initial values $(x_0, y_0, z_0, w_0) = (0.475, 0.9, 0.1, 0.1)$, the solution shows a ICC as shown in Fig. 5.7.6(a) and (b), respectively.

Next, we clarify the basin boundary the periodic solution and ICC. For simplicity, we fix $z_0 = w_0 = 0.8$. If the solution converges to the periodic solution or two-dimensional tori, we plot the gray or blue point, respectively. Moreover, diverging solutions are marked by green. The basins of these solutions obtained at the point R $(\varepsilon_1 = 0.01, \varepsilon_1 = 0.02, B_1 = 2.1575, B_2 = 2.02165)$ that is projected onto the $x - y$ plane are shown in Fig. 5.7.7. It shows a complicated basin boundary, which is similar to Fig. 5.5.4.

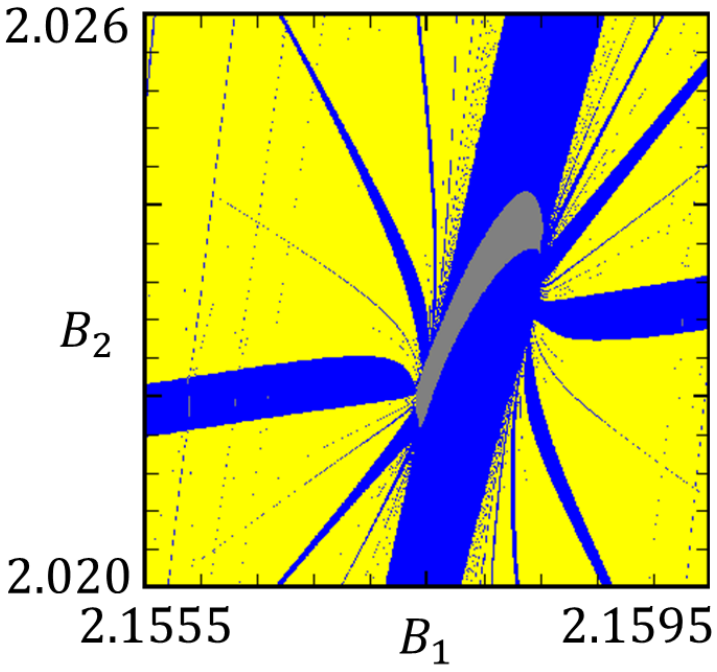

(a) Lyapunov diagram.

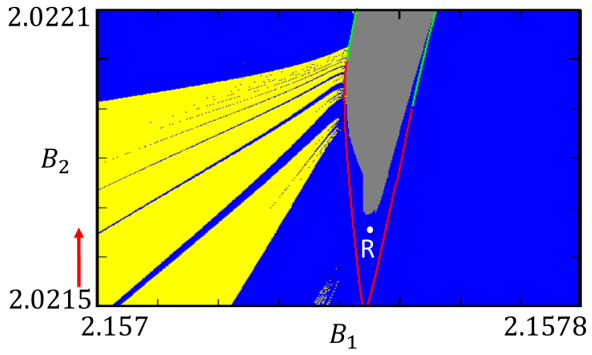

(b) Bottom left.

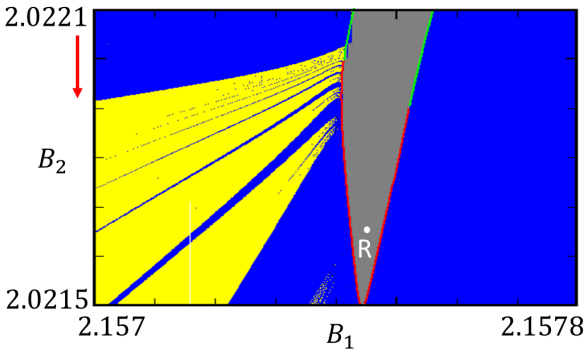

(c) Top left.

Figure 5.7.2 Lyapunov diagrams obtained from different initial parameter values ($\varepsilon_1 = 0.01$ and $\varepsilon_2 = 0.02$).

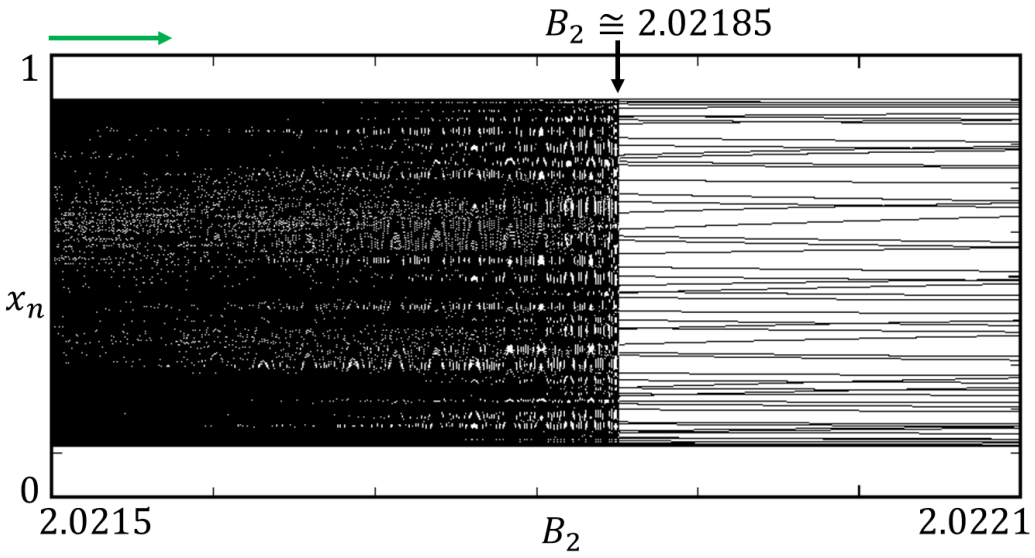

(a) Increasing B_2.

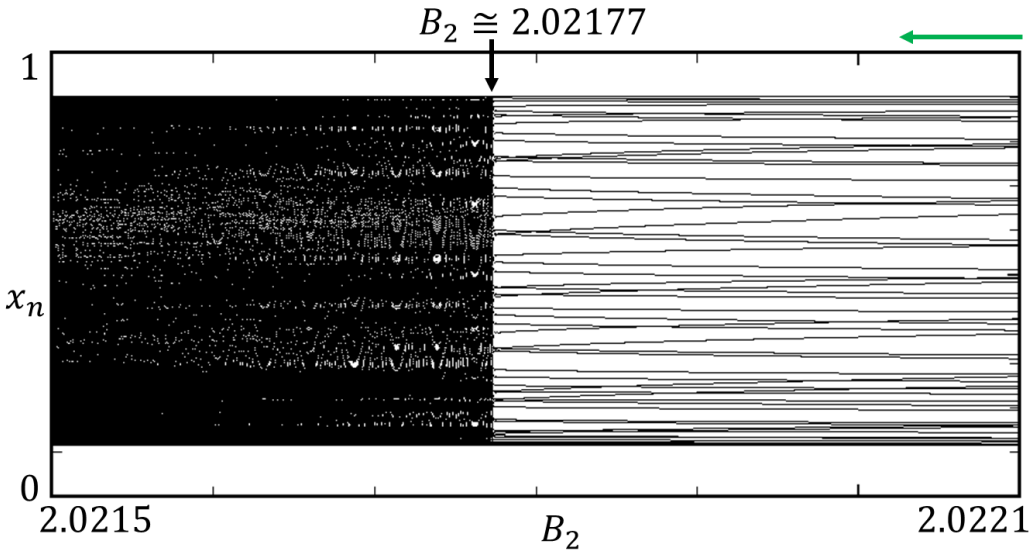

(b) Decreasing B_2.

Figure 5.7.3 One-parameter bifurcation of the two-coupled delayed logistic map ($\varepsilon_1 = 0.01$, $\varepsilon_2 = 0.02$, and $B_1 = 2.1575$).

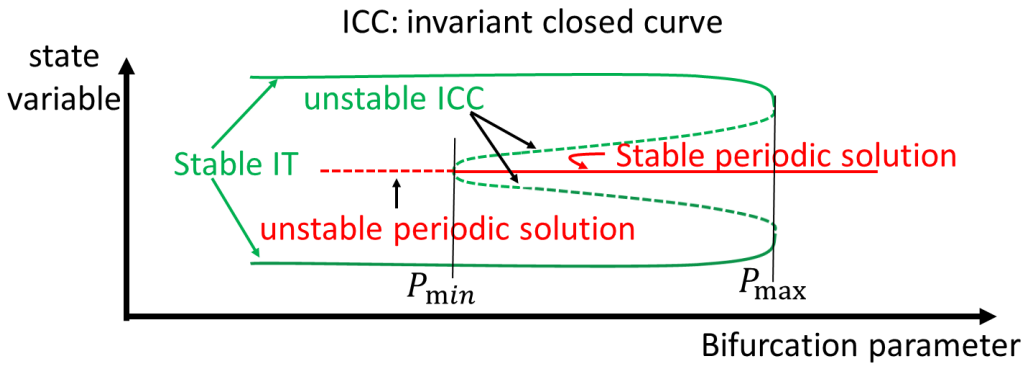

Figure 5.7.4 Schematic diagram of subcritical Neimark–Sacker bifurcation.

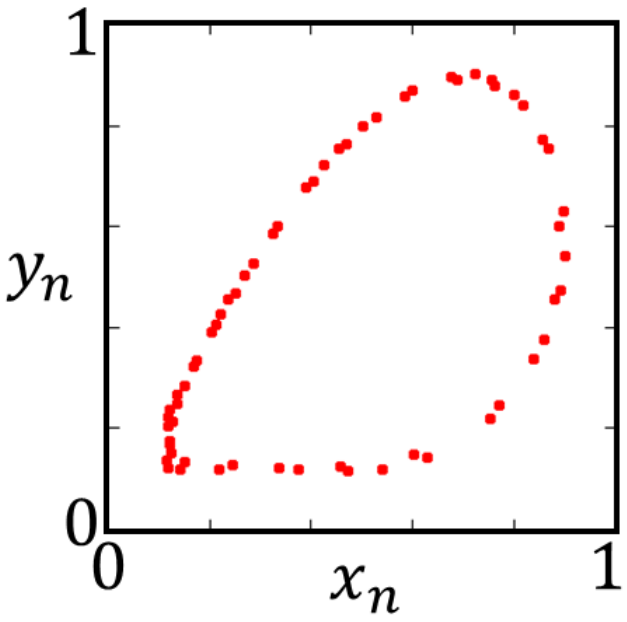

(a) $x_n - y_n$.

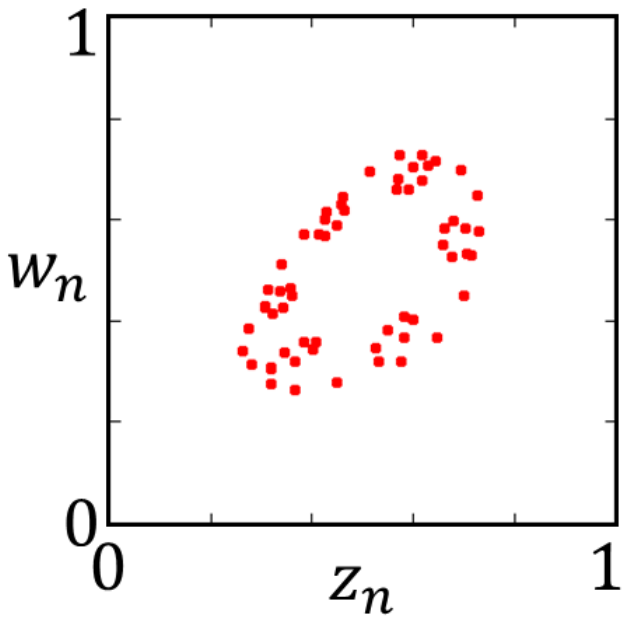

(b) $z_n - w_n$.

Figure 5.7.5 Periodic attractor with period 122.

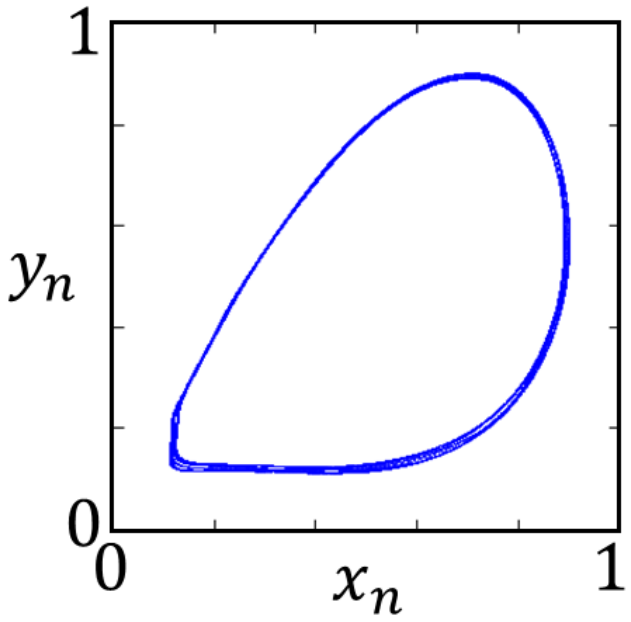

(a) $x_n - y_n$.

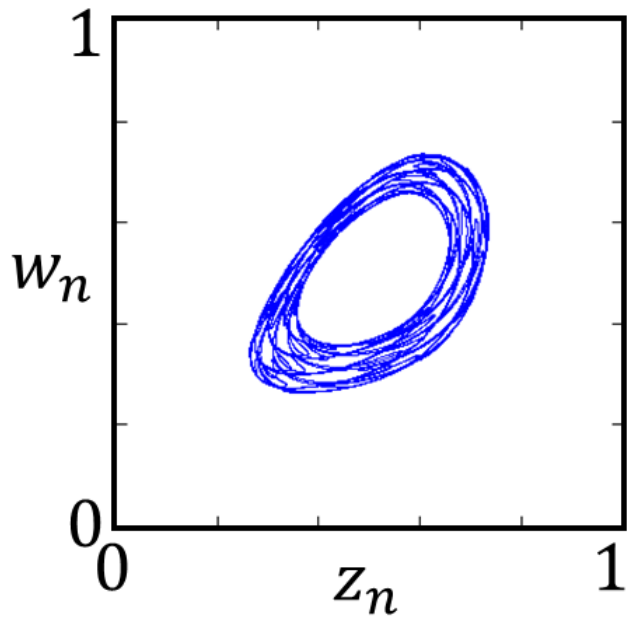

(b) $z_n - w_n$.

Figure 5.7.6 Invariant closed curve.

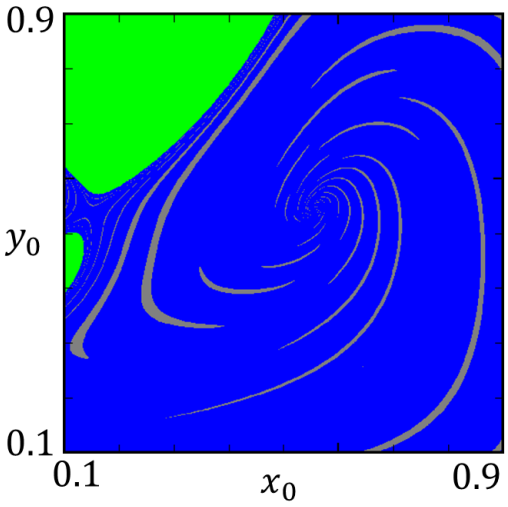

(a)

Figure 5.7.7 Basins of the periodic attractor and the invariant tori at point R ($\varepsilon_1 = 0.01, \varepsilon_2 = 0.02, B_1 = 2.15745$, and $B_2 = 2.02165$) in Fig. 5.7.2 on the (x_0, y_0) plane with $z_0 = 0.8$ and $w_0 = 0.8$.

5.8 Conclusions

We analyzed ARW and Chenciner bubbles generated in a three-coupled PWCOs. Two-parameter Lyapunov diagrams were derived to discuss the bifurcation structures. According to the numerics, the hysteresis phenomenon was observed. It did not distort the Chenciner bubbles as observed in two-coupled PWCOs driven by a rectangular forcing. To clarify this phenomenon, a two-coupled delayed logistic map was investigated. Based on Lyapunov analysis using this dynamics, it was suggested that the hysteresis might occur owing to a subcritical Neimark-Sacker bifurcation. However, the saddle-node bifurcation curves between ICC and periodic solution obtained by using Lyapunov analysis did not coincide with the boundaries using the shooting algorithm proposed in Ref [16]. In future work, we plan to clarify the bifurcation mechanism that cause the hysteresis phenomenon. Moreover, we are interest in how hysteresis strongly influence on Arnol'd resonance webs in higher-dimensional dynamics.

Chapter 6

Overall Conclusions

In this thesis, we have investigated the quasi-periodic bifurcation phenomena generated in coupled oscillators. Specifically, we concentrated on the following two topics:

(A) Arnol'd tongues generated in two-coupled oscillators.

(B) Arnol'd resonance webs generated in two-coupled oscillators including a periodic forcing and three-coupled oscillators.

In Chapter 2, we introduced a preliminary study on piecewise-constant oscillators (ab. PWCOs). We focus on the simplest type of PWCOs, which consist of one capacitor and one voltage controlled current sources (ab. VCCSs) with a hysteresis characteristic. The oscillation generates a triangular wave, and it is confirmed numerically and experimentally. We also investigate two-coupled PWCOs, we point out that each PWCO must be connected by capacitors in order for the circuit to become piecewise-constant.

In Chapter 3, we considered quasi-periodic phenomena generated in an autonomous two-coupled PWCOs. We created some rigorous two-parameter Lya-

punov diagrams. Our numerical results showed that Arnol'd tongues are generated in a wide range of parameter range. Moreover, the analysis of the system arrives at that of a 1-D return map. By using the 1-D return map, we clarified that Arnol'd tongues are surrounded by a non-smooth tangent bifurcation. Several bifurcation boundaries were explicitly derived.

In Chapter 4, we investigated chaos and quasi-periodic oscillations generated in a non-autonomous two-coupled PWCOs. We formulated the numerical procedure for conducting the Lyapunov analysis in PWCOs. Two-parameter Lyapunov diagrams were obtained, which show the complex bifurcation structures. According to the numerical results, chaos and Arnol'd resonance webs are clearly observed. Inevitably, we observed hysteresis phenomenon, which distorts the Chenciner bubbles in the cases of weak coupling. Furthermore, the generation pattern of two-dimensional tori was demonstrated numerically and experimentally.

In Chapter 5, we proposed an autonomous three-coupled PWCOs that generates three-dimensional tori. Two-parameter Lyapunov diagrams were derived to discuss the bifurcation structures. Arnol'd resonance webs, chaos and the hysteresis phenomenon was also observed. However, the hysteresis did not distort the Chenciner bubbles as observed in two-coupled PWCOs driven by a rectangular wave forcing. To clarify this phenomenon, a two-coupled delayed logistic map was investigated. Based on Lyapunov analysis using this dynam-

ics, it was suggested that the hysteresis might occur owing to a subcritical Neimark-Sacker bifurcation.

We analyzed complex quasi-periodic phenomena generated in some coupled PWCOs with a significantly high resolution similar to that of discrete-time dynamical systems. We formulated a systematic procedure for conducting Lyapunov analysis in PWCOs. This procedure is applicable in both autonomous and non-autonomous PWCOs driven by a rectangular wave forcing. The extremely simple procedure will contribute to the study on bifurcation analysis of the family of PWCOs. Although, the hysteresis phenomenon is evident in both autonomous and non-autonomous PWCOs that generates three-dimensional tori, we could not fully clarify the bifurcation mechanism causing it at present.

In future, we consider the following works:

(i) To analyze the entire bifurcation structures of quasi-periodic phenomena generated in two-coupled PWCOs.

(ii) To clarify the generation mechanism of hysteresis phenomenon.

(iii) To investigate how hysteresis strongly influences on Arnol'd resonance webs in higher-dimensional dynamics.

References

[1] F.C. Hoppensteadt and J.P. Keener, "Phase Locking of Biological Clocks," J. Math. Biol., vol. 15, pp. 339-349, 1982.

[2] L. Glass, "Cardiac Arrhythmias and Circle Maps–A Classical Problem," Chaos, vol. 1, pp. 13-19, 1991.

[3] T. Nagai and S. Doi, "Oscillations, Bistabilities and Bifurcations in a Cardiac Pacemaker Cell Model," Proc. of NOLTA2016, pp. 318-321, 2016.

[4] C. Huygens, The Pendulum Clock, Iowa State University Press, 1986 (translated from French).

[5] Y. Kuramoto, Chemical Oscillations, Waves and Turbulence, Spinger, 1984.

[6] A. Pikovsky, M. Rosenblum, and J. Kurths, A Universal Concept in Nonlinear Sciences, Cambridge University Press, 2001.

[7] B. Romeira, J.M.L. Figueiredo, C.N. Ironside, and T. Slight, "Chaotic Dynamics in Resonant Tunneling Optoelectronic Voltage Controlled Oscillators," IEEE Photonics Technology Letters, vol. 21, no. 24, pp. 1819-1821, 2009.

[8] D.P. Rosin, D. Rontani, and D.J. Gauthier, "Synchronization of Coupled Boolean Phase Oscillators," Phys. Rev. E, vol. 89, 042907, pp. 1-7, 2014.

[9] K. Umeno, "Spread Spectrum Communications Based On Almost Periodic Functions–Almost Periodic Code Approach Versus Chaotic Code Approach for Communications–," IEICE Technical Report, vol. 114, no. 250, NLP2014-62, pp. 87-90, 2014 (in Japanese).

[10] A. Suárez and R. Quéré, Stability Analysis of Nonlinear Microwave Circuits, Artech House, 2003.

[11] H. Bai-lin, Elementary Symbolic Dynamics and Chaos in Dissipative Systems, World Scientific, 1989.

[12] M.H. Jensen, P. Bak, and T. Bohr, "Complete Devil's Staircase, Fractal Dimension, and Universality of Mode-Locking Structure in the Circle Map," Phys. Rev. Lett, vol. 50, no. 21, pp. 1637-1639, 1983.

[13] R.E. Best, Phase-Locked Loops, McGraw-Hill, 2003.

[14] A.E. Aroudi, L. Benadero, E. Toribio, and S. Machiche, "Quasiperiodicity and Chaos in the DC-DC Buck-Boost Converter," Internat. J. Bifur. Chaos, vol. 10, pp. 359-371, 2000.

[15] A. Pikovsky and M. Rosenblum, "Synchronization: a General Phenomenon in an Oscillatory World," Nova Acta Leopoldina, vol. NF 88, pp. 255-268, 2003.

[16] H. Kawakami, "Bifurcation of Periodic Responses in Forced Dynamic Nonlinear Circuits: Computation of Bifurcation Value of the System Parameters," IEEE Trans. Circuits Syst., vol. CAS-31, no. 3, pp. 248-260, 1984.

[17] L.O. Chua, M. Komuro, and T. Matsumoto, "The Double Scroll Family," IEEE Trans. Circuits Syst., vol. CAS-33, no. 11, pp. 1073-1118, 1986.

[18] T. Matsumoto, L.O. Chua, and R. Tokunaga, "Chaos Via Torus Breakdown," IEEE Trans. Circuits Syst., vol. CAS-34, no. 3, pp. 240-253, 1987.

[19] T. Saito, "On Chaos Generating Circuits Described by a Piecewise-Linear Constrained Equation," IEICE Trans. Fundamentals, vol. J71-A, no. 4, pp. 965-972, 1988 (in Japanese).

[20] T. Saito, "Reality of Chaos in Four-Dimensional Hysteretic Circuits," IEEE Trans. Circuits Syst., vol. 38, no. 12, pp. 1517-1524, 1991.

[21] N. Inaba and S. Kokura, "Bifurcation and Chaos in the Forced Rayleigh Oscillator with a Diode," IEICE Trans. Fundamentals, vol. J76-A, no. 7, pp. 942-950, 1993 (in Japanese).

[22] N. Inaba and N. Baba, "Bifurcation Sets in the Forced Rayleigh Oscillator with a Diode," IEICE Trans. Fundamentals, vol. J78-A, no. 4, pp. 485-492, 1995 (in Japanese).

[23] T. Tsubone and T. Saito, "Manifold Piecewise Constant Systems and Chaos," IEICE Trans. Fundamentals, vol. E82-A, pp. 1619-1626, 1999.

[24] T. Tsubone, N. Inaba, T. Tsubouchi, and T. Yoshinaga, "Synchronization Phenomena from an Extremely Simplified Piecewise-Constant Driven Oscillator," IEICE Trans. Fundamentals, vol. J93-A, pp. 375-383, 2010 (in Japanese).

[25] K. Suzuki and T. Tsubone, "In-Phase and Anti-Phase Synchronization Phenomena in Coupled Systems of Piecewise Constant Oscillators," IEICE Trans. Fundamentals, vol. E98-A, pp. 340-353, 2015.

[26] H. Kuriyama and T. Tsubone, "Arnold Tongues of 2-D Piecewise Constant Driven Oscillator," Proc. of NOLTA 2015, vol. E98-A, pp. 479-482, 2015.

[27] T. Tsubone, T. Saito, and N. Inaba, "Design of an Analog Chaos-Generating Circuit Using Piecewise-Constant Dynamics," Prog. Theor. Exp. Phys., vol. 2016, 053A01, 2016.

[28] P.S. Linsay and A.W. Cumming, "Three-Frequency Quasiperiodicity, Phase Locking, and The Onset of Chaos," Physica D, vol. 40, pp. 196-217, 1989.

[29] C. Baesens, J. Guckenheimer, S. Kim, and R.S. Mackay, "Three Coupled Oscillators: Mode-Locking, Global Bifurcations and Toroidal Chaos," Physica D, vol. 49, pp. 387-475, 1991.

[30] H. Broer, C. Simó, and R. Vitolo, "The Hopf-saddle-node Bifurcation for Fixed Points of 3D-diffeomorphisms: the Arnol'd Resonance Web," Bull. Belg. Math. Soc. Simon Stevin, vol. 15, pp. 769-787, 2008.

[31] H. Broer, C. Simó, and R. Vitolo, "The Hopf-saddle-node Bifurcation for Fixed Points of 3D-diffeomorphisms: Analysis of a Resonance 'bubble'," Physica D, vol. 237, pp. 1773-1799, 2008.

[32] R. Vitolo, H. Broer, and C. Simó, "Quasi-periodic Bifurcations of Invariant Circles in Low-dimensional Dissipative Dynamical Systems," Regul. Chaotic Dyn., vol. 16, pp. 154-184, 2011.

[33] A.P. Kuznetsov, S.P. Kuznetsov, I.R. Sataev, and L.V. Turukina, "About Landau-Hopf Scenario in a System of Coupled Self-Oscillators," Phys. Lett. A, vol. 377, pp. 3291-3295, 2013.

[34] A.P. Kuznetsov and Y.V. Sedova, "Low-Dimensional Discrete Kuramoto Model: Hierarchy of Multifrequency Quasiperiodicity Regimes," Internat. J. Bifur. Chaos, vol. 24, 1430022, 2014.

[35] M. Sekikawa, N. Inaba, T. Tsubouchi, and K. Aihara, "Novel Bifurcation Structure Generated in Piecewise-Linear Three LC Resonant Circuit and Its Lyapunov Analysis," Physica D, vol. 241, pp. 1169-1178, 2012.

[36] K. Kamiyama, N. Inaba, M. Sekikawa, and T. Endo, "Bifurcation Boundaries of Three-Frequency Quasi-periodic Oscillations in Discrete-Time Dynamical System," Physica D, vol. 289, pp. 12-17, 2014.

[37] M. Sekikawa, N. Inaba, K. Kamiyama, and K. Aihara, "Three-dimensional Tori and Arnold Tongues," Chaos, vol. 24, 013137, 2014.

[38] Y.P. Emelianova, A.P. Kuznetsov, I.R. Sataev, and L.V. Turukina, "Synchronization and Multi-frequency Oscillations in the Low-dimensional Chain of the Self-oscillators," Physica D, vol. 244, pp. 36-49, 2013.

[39] Y.P. Emelianova, A.P. Kuznetsov, L.V. Turukina, I.R. Sataev, and N.Y. Chernyshov, "A Structure of the Oscillation Frequencies Parameter Space for the System of Dissipatively Coupled Oscillators," Commun. Nonlinear Sci. Numer. Simul., vol. 19, pp. 1203-1212, 2014.

[40] V.S. Anishchenko, M.A. Safonova, U. Feudel, and J. Kurths, "Bifurcation and Transition to Chaos Through Three-Dimensional Tori," Int. J. Bifurc. Chaos, vol. 4, pp. 595-607, 1994.

[41] V.S. Anishchenko, S.M. Nikolaev, and J. Kurths, "Synchronization Mechanisms of Resonant Limit Cycle on Two-Dimensional Torus," Russ. J. Nonlinear Dyn., vol. 4, pp. 39-56, 2008 (in Russian).

[42] V. Anishchenko, S. Nikolaev, and J. Kurths, "Bifurcational Mechanisms of Synchronization of a Resonant Limit Cycle on a Two-Dimensional Torus," Chaos, vol. 18, 037123, 2008.

[43] V.Anishchenko, S. Astakhov, and T. Vadivasova, "Phase Dynamics of Two Coupled Oscillators under External Periodic Force," Europhys. Lett., vol. 86, 30003, 2009.

[44] V.S. Anishchenko, S.V. Astakhov, T.E. Vadivasova, and A.V. Feoktistov, "Numerical and Experimental Study of External Synchronization of Two-Frequency Oscillations," Nelin. Dinam., vol. 5, pp. 237-252, 2009.

[45] A.P. Kuznetsov and J.P. Roman, "Properties of Synchronization in the Systems of Non-Identical Coupled Van Der Pol and Van Der Pol–Duffing Oscillators. Broadband Synchronization," Physica D, vol. 238, pp. 1499-1506, 2009.

[46] A.P. Kuznetsov, I.R. Sataev, and L.V. Tyuryukina, "Synchronization of Quasi-periodic Oscillations in Coupled Phase Oscillators," Tech. Phys. Lett., vol. 36, pp. 478-481, 2010.

[47] A.P. Kuznetsov, I.R. Sataev, and L.V. Tyuryukina, "On the Road Towards Multidimensional Tori," Commun. Nonlinear Sci. Numer. Simul., vol. 16, pp. 2371-2376, 2011.

[48] Y.P. Emelianova, A.P. Kuznetsov, and L.V. Turukina, "Quasi-periodic Bifurcations and "Amplitude Death" in Low-dimensional Ensemble of Van der Pol Oscillators," Phys. Lett. A, vol. 378, pp. 153-157, 2014.

[49] M. Sekikawa and N. Inaba, "Doubly Twisted Neimark–Sacker Bifurcation and Two Coexisting Two-Dimensional Tori," Phys. Lett. A, vol. 380, pp. 171-176, 2016.

[50] P. Ashwin, "Boundary of Two Frequency Behaviour in a System of Three Weakly Coupled Electronic Oscillators," Chaos Solitons Fractals, vol. 9, pp. 1279-1287, 1998.

[51] K. Itoh, N. Inaba, M. Sekikawa, and T. Endo, "Three-Torus-Causing Mechanism in a Third-Order Forced Oscillator," Prog. Theor. Exp. Phys., vol. 2013, 0903A02, 2013.

[52] N. Inaba, M. Sekikawa, Y. Shinotsuka, K. Kamiyama, K. Fujimoto, T. Yoshinaga, and T. Endo, "Bifurcation Scenarios for a 3D Torus and Torus-Doubling," Prog. Theor. Exp. Phys., vol. 2014, 023A01, 2014.

[53] N. Inaba, K. Kamiyama, T. Kousaka, and T. Endo, "Numerical and Experimental Observation of Arnold Resonance Webs in an Electrical Circuit," Physica D, 311-312, pp. 17-24, 2015.

[54] F. Takens and F.O.O. Wagener, "Resonances in Skew and Reducible Quasi-Periodic Hopf Bifurcations," Nonlinearity, vol. 13, pp. 377-396, 2000.

[55] Y.A. Kuznetsov and H.G.E. Meijer, "Remarks on Interacting Neimark–Sacker Bifurcations," J. Difference Equ. Appl., vol. 12, pp. 1009-1035, 2006.

[56] K. Kamiyama, M. Komuro, and T. Endo, "Bifurcation of Quasi-Periodic Oscillation in Mutually Coupled Hard-Type Oscillators: Demonstration of Unstable Quasi-Periodic Orbits," Internat. J. Bifur. Chaos, vol. 22, 1230022, 2012.

[57] K. Kamiyama, M. Komuro, and T. Endo, "Algorithms for Obtaining a Saddle Torus Between Two Attractors," Internat. J. Bifur. Chaos, vol. 23, 1330032, 2013.

[58] K. Kamiyama, M. Komuro, T. Endo, and K. Aihara, "Classification of Bifurcations of Quasi-Periodic Solutions Using Lyapunov Bundles," Internat. J. Bifur. Chaos, vol. 24, 1430034, 2014.

[59] S. Hidaka, N. Inaba, K. Kamiyama, M. Sekikawa, and T. Endo, "Bifurcation Structure of an Invariant Three-Torus and Its Computational Sensitivity Generated in a Three-Coupled Delayed Logistic Map," NOLTA IEICE, vol. 6, pp. 433-442, 2015.

[60] N.V. Stankevich, J. Kurths, and A.P. Kuznetsov, "Forced Synchronization of Quasiperiodic Oscillations," Commun. Nonlinear Sci. Numer. Simul., vol. 20, pp. 316-323, 2015.

[61] S. Hidaka, N. Inaba, M. Sekikawa, and T. Endo, "Bifurcation Analysis of Four-Frequency Quasi-Periodic Oscillations in a Three-Coupled Delayed Logistic Map," Phys. Lett. A, vol. 379, pp. 664-668, 2015.

[62] G. Benettin, L. Galgani, A. Giorgilli, J.-M. Streichyn, "Lyapunov Characteristic Exponents for Smooth Dynamical Systems and for Hamiltonian Systems; a Method for Computing All of them. Part 1: Theory," Meccanica, vol. 15, pp. 9-20, 1980.

[63] I. Shimada and T. Nagashima, "A Numerical Approach to Ergodic Problem of Dissipative Dynamical Systems," Prog. Theor. Phys., vol. 61, pp. 1605-1616, 1979.

[64] D. Ruelle and F. Takens, "On the Nature of Turbulence," Comm. Math. Phys, vol. 20, pp. 167-192, 1971.

A list of the related papers by the author

(Original papers)

1. Tri Quoc Truong, Tadashi Tsubone, Munehisa Sekikawa, and Naohiko Inaba, "Complicated quasiperiodic oscillation and chaos from driven piecewise-constant circuit: Chenciner bubbles do not necessarily occur via simple phase-locking," Physica D: Nonlinear Phenomena, vol. 341, pp. 1-9, 2017.

2. Tri Quoc Truong, Tadashi Tsubone, Kuniyasu Shimizu, and Naohiko Inaba, "Experimental study of mixed-mode oscillations in a four-segment piecewise linear Bonhoeffer-van der Pol oscillator under weak periodic perturbation–Successive and nonsuccessive MMO-incrementing bifurcations–," IEICE Transactions on Fundamentals of Electronics, Communications and Computer Sciences, vol. E100-A, no. 7, pp. 1522-1531, 2017.

3. Tri Quoc Truong, Tadashi Tsubone, Munehisa Sekikawa, Naohiko Inaba, and Tetsuro Endo, "Arnol'd resonance web and Chenciner bubbles from a threedimensional piecewise-constant hysteresis oscillator," Progress of The-

oretical and Experimental Physics, vol. 2017, no. 5, 053A04, 2017.

(International symposia)

1. Tri Quoc Truong, Tadashi Tsubone, Naohiko Inaba, and Tetsuro Endo, "Chaos near the Chenciner bubbles from a piecewise-constant system," Proceedings of the 2016 International Symposium on Nonlinear Theory and Its Applications, 2016.

2. Tri Quoc Truong, Tadashi Tsubone, and Naohiko Inaba, "Analysis of bifurcation phenomena of coupled piecewise-constant hysteresis oscillators," Proceedings of the 2017 International Symposium on Nonlinear Theory and Its Applications, 2017.

(Technical reports and other presentations)

1. Tri Quoc Truong, Tadashi Tsubone, Munehisa Sekikawa, Naohiko Inaba, and Tetsuro Endo, "Arnol'd resonance web and Chenciner bubbles in 3-dimensional piecewise-constant oscillator," IEICE Technical Report, vol. 116, no. 353, NLP2016-93, pp. 49-54, December 2016.

2. Tri Quoc Truong, Tadashi Tsubone, and Naohiko Inaba, "Chaos and Chenciner bubbles of a piecewise-constant system," IEICE Technical Report, vol. 116, no. 86, NLP2016-31, pp. 61-64, June 2016.

3. Naohiko Inaba, Kuniyasu Shimizu, Tri Quoc Truong, Tadashi Tsubone, Hiroyuki Asahara, Takuji Kousaka, and Tetsuro Endo, "Mixed-mode os-

cillationincrementing bifurcations and universal constant from BVP oscillators Part2," IEICE Technical Report, vol. 116, no. 86, NLP2016-32, pp. 65-70, June 2016.

4. Tri Quoc Truong and Tadashi Tsubone, "Study on a derivation method of Arnold Resonance Web in piecewise-constant systems," The 2015 IEICE Shinetsu Section Conference, 2B-3, p.22, October 2015 (Japanese).

5. Tri Quoc Truong and Tadashi Tsubone, "Study on synchronization phenomena of a driven piecewise-constant oscillator," IEICE Technical report, vol. 114, no. 288, NLP2014-97, pp. 91-94, November 2014 (Japanese).

6. Tri Quoc Truong and Tadashi Tsubone, "Synchronization phenomena of hysteresis piecewise constant oscillators by using common external force," The 2014 IEICE Shinetsu Section Conference, P-1, p. 167, October 2014 (Japanese).